공 학 박 사 학 위 논 문

Synthesis and Characterization of Dynamic Covalent Polymer Networks for Soft Robotics and IR Optical Applications

동적 공유결합 고분자 네트워크 합성과 분석

그리고 소프트 로봇 및 적외선 광학소재로의 응용

2 0 2 3 년 8 월

서울대학교 대학원

화학생물공학부

황 재 혁

Synthesis and Characterization of Dynamic Covalent Polymer

Networks for Soft Robotics and IR Optical Applications

by

Jae Hyuk Hwang

Adviser: Professor Jong-Chan Lee, Ph. D.

Submitted in Partial Fulfillment
of the Requirements for the Degree of
DOCTOR OF PHILOSOPHY

August, 2023

School of Chemical and Biological Engineering
College of Engineering
Graduate School
Seoul National University

동적 공유결합 고분자 네트워크 합성과 분석

그리고 소프트 로봇 및 적외선 광학소재로의 응용

Synthesis and Characterization of Dynamic Covalent Polymer Networks for Soft Robotics and IR Optical Applications

지도교수 이 종 찬 박사

이 논문을 공학박사학위 논문으로 제출함.

2023년 8월

서울대학교 대학원

화학생물공학부

황 재 혁

황재혁의 박사학위논문을 인준함.

2023년 8월

위원장   (인)

부위원장   (인)

위   원   (인)

위   원   (인)

위   원   (인)

Abstract

This study presents the synthesis and characterization of dynamic covalent polymer networks (DCPN) for soft robotics and infrared (IR) applications. Firstly, dynamic photo-controllable liquid crystalline network (pc-LCN) containing 2-methylene-propane-1,3-bis(thioethyl acrylate) (MBTA) crosslinker capable of dynamic allyl sulfide bond exchange and static 4-bis-[4-(3-acryloyloxypropyloxy)benzoyloxy]-2-methylbenzene (RM257) crosslinker capable of static crosslinking were synthesized. Static and dynamic covalent dual-crosslinked pc-LCN enabled Lego-like reversible assembly between the interfaces of films due to MBTA, and the crosslinked structure was maintained due to the static RM257 crosslinker. By tailoring the static and dynamic covalent linkages in the networks, pc-LCN films could be readily reconfigured and assembled into complex 3D structures under ultraviolet (UV) irradiation. Such monoliths could also be disassembled into their constituent building block films and reassembled into different architectures under the same UV irradiation. Moreover, for various adaptive actuation control of soft robots, selective visible-light-responsive dopant dyes were adopted to actuate pc-LCN building blocks. The pc-LCNs containing dyes that absorb different wavelengths within visible light were selectively actuated. The pc-LCN film building blocks with each dye were monolithically assembled

into Lego-like 3D soft transformable robots. 3D soft transformable robots with versatile locomotion capabilities, including rolling, gripping, and cargo transport in multiple directions, were demonstrated.

Secondly, a new class of poly(thiourethane) (MFTU) vitrimer with an excess thiol ratio of 10 mol % was synthesized. MFTU containing excess thiol enabled fast dynamic thiourethane bond exchange based on zinc diethyldithiocarbamate $(Zn(DTC)_2)$ catalyst compared to conventional dibutyltin dilaurate (DBTDL) catalyst. Stiffness modulation of MFTU was enabled by the melting transition of semi-crystalline structure within the network. Young's modulus of MFTU increased 70.5 times in the rigid state compared to the pliable state. Furthermore, the formation of hydrogen bonds and Zn coordination bonds realized reversible assembly/disassembly between MFTU films. In the MFTU network, thiol ligand exchange occurred over 60 $^{\circ}$C, and hydrogen bonds were separated. At this time, new hydrogen bonds and Zn coordination bonds are formed between the interfaces of the MFTU films, resulting in an assembly. When heat treatment was applied to the assembled MFTU film again with gentle stress, the hydrogen bond was separated while thiol ligand exchange occurred, causing the MFTU films to disassemble each other. Through these multifunctional properties, the MFTU building blocks were manufactured as soft hand robots and performed magnetic actuation according to rigid or pliable states. The soft hand robot was transformed

into a soft receiver again, safely receiving the object in a pliable state. By rigid programming, the soft receiver performed cargo gripping and delivery.

Finally, *in-situ* microphase-separated sulfur-rich copolymers were synthesized via inverse vulcanization of elemental sulfur utilizing 1,3,5-trivinylbenzene (TVB). Since self-crosslinking is possible because the TVB crosslinker has a very high ceiling temperature of 400 °C, a self-crosslinked TVB-rich domain was formed during inverse vulcanization. Since elemental sulfur reacted with TVB to form a polysulfide-rich domain, poly(sulfur-*random*-TVB) (poly(S-*r*-TVB)) showed a microphase-separated structure. Even with 80 wt % sulfur content, the microphase-separated TVB-rich domain self-reinforces the copolymer with a noteworthy modulus of $\approx$2.0 GPa and a high glass transition temperature (T_g) of 92.6 °C, while still exhibiting outstanding IR optical properties. Through IR imaging, poly(S-*r*-TVB) showed a high-resolution image compared to opaque reference samples. Therefore, the trade-off relationship between the IR transmittance (sulfur content) and thermal properties of sulfur copolymers was resolved through the self-crosslinkable TVB crosslinker.

TABLE OF CONTENTS

Chapter 1

Introduction

Chapter 2

Dynamic Photo-Controllable Liquid Crystalline Networks for Monolithically Assembled 3D Soft Transformable Robot

Chapter 3

Multifunctional Poly(thiourethane) Vitrimer with Variable Stiffness and Lego-like Assembly/Disassembly Properties for 3D Transformable Soft Robot

Chapter 4

A Microphase Separation Strategy for the Infrared Transparency–Thermomechanical Property Conundrum in Sulfur-Rich Copolymers

List of Tables

List of Figures

MWIR camera. (f) Comparison of the MWIR thermal images of poly(S_{80}-r-TVB$_{20}$) and PMMA windows. The thickness of all films is 1.1 mm.

Chapter 1

Introduction

1.1. Dynamic Covalent Polymer Networks

Polymers are broadly divided into thermoplastics and thermosets. Primarily linear polymers, thermoplastics, exhibit reprocessability and recyclability but show poor thermomechanical properties at high temperatures. In contrast, thermosets with crosslinked structures present excellent thermomechanical properties and dimensional stability, but reprocessing and recycling are challenging. To overcome these challenges, dynamic covalent bond exchanges can be incorporated into a crosslinked thermoset polymer to develop dynamic covalent polymer networks (DCPN), which show reprocessability, recyclability, enhanced dimensional stability, and excellent thermomechanical properties. Synergistically combined with thermoplastic and thermoset polymers, DCPNs exhibit great potential in polymer chemistry to substitute traditional thermoplastic or thermosets (Figure 1.1). Based on dynamic covalent bond exchanges, the topology of the DCNP can be switched via exchange reactions at the crosslinking points (Figure 1.2) [1]. Such a fascinating mechanism facilitates the reprocessing and recycling of the crosslinked polymer, which was previously challenging to achieve.

Since Leibler *et al.* introduced the associative dynamic transesterification reaction into epoxy-based crosslinked polymers in 2011 [2], DCPNs based on dynamic covalent bond exchanges have received significant attention. DCPNs are

divided into vitrimer and vitrimer-like materials according to the types of dynamic covalent bond exchanges. Vitrimers are based on S_N2-type associative dynamic covalent bond exchange reactions under catalysis and can maintain crosslinking density due to the simultaneous occurrence of covalent bond separation and formation [3]. Due to the crosslinking density maintained during the dynamic covalent bond exchange, insoluble vitrimers show stress relaxation behavior at high temperatures, and welding between films, reprocessing, injection molding, and reshaping is possible. On the contrary, vitrimer-like materials are composed of dissociative dynamic covalent bonds and cannot maintain network integrity during the covalent bond exchange and have flowability. Vitrimer-like materials cannot show stress relaxation behavior at high temperatures due to the dissociation of crosslinked structure but can be reprocessed, recycled, or welded at high temperatures. Once polymerized, DCPNs with vitrimers and vitrimer-like materials can undergo covalent bond exchanges such as transesterification [2,4,5], transamination [6,7], dioxaborolane metathesis [8], silyl ether [9], urethane [10-12], urea [13,14], thiourea [15], thiourethane [16-18], polysulfide [19] and boronic ester bond exchange reactions [20].

Recently, many researches have been broadly conducted on the effective decomposition and recycling of various DCPNs [17,21]. In addition to the self-healing and recyclability with excellent mechanical, rheological, and thermal

properties, the demand for DCPNs with various functionalities is growing. Reprocessable DCPNs have shown malleability and rheological behavior in the solid state, making it possible to use as various stimuli-responsive materials with the incorporation of functional fillers. Therefore, DCPNs can be used as multi-stimuli responsive shape memory polymers [22], reprogrammable liquid crystalline elastomers [23], and 3D/4D printing materials [5,24,25]. In addition, DCPN composite 2D films can be fabricated into 3D architectures through welding and reprocessing using dynamic covalent bond exchangeable properties of DCPNs. Strategies for 3D structure fabrications can be applied to various fields, such as shape morphing devices [26], soft robotics [27], carbon fiber reinforced plastic (CFRP) [28].

1.2. Polymeric Materials for Soft Robotics Applications

Conventional rigid robots are widely used in manufacturing but have limited adaptability. While rigid robots use pin joints to connect the links of each part, soft robots use polymeric materials to form joints, enabling act similarly to the movements of living things. Therefore, soft robots can safely interact with surrounding objects in complex and diverse environments and have recently attracted significant attention [29]. The driving methods of soft robots include pneumatic, motor-wire (tendon), and driving using smart materials. Among the driving methods, polymers can be applied to soft robots as smart materials with lightweight and subminiature structures based on various forms of deformation. Based on the storage and elastic modulus, soft robots are made of soft polymeric materials like biological muscles and can realize complex motions with facile deformations of bending and twisting with high curvature.

Stimuli-responsive materials such as liquid crystalline networks (LCN) and shape-memory polymers are required to give these soft robots for controlled shape-transformation functions (Figure 1.3) [30-34]. In response to stimuli, soft robots can implement various movements such as rolling, crawling, walking, gripping, and jumping [35-39]. LCNs are composed of rigid mesogens, and the alignment of mesogens in LCNs changes from a nematic state to an isotropic state based on

isotropic transition temperature (T_i) under external stimuli (heat or light) [40]. As the alignment of mesogens in LCN changes to an isotropic state, the bending actuation of the LCN film occurs, and reversible shape deformation using this can be applied macroscopically. Shape memory polymer is a polymer that memories the initial shape of the polymer and returns to its original shape (permanent shape) from the deformed shape (temporarily fixed shape) by appropriate external stimuli [41]. Generally, shape memory properties can be implemented when the chain is temporarily fixed by lowering the polymer below the transition temperature, which is strained above the transition temperature, such as the glass transition temperature (T_g) or crystallization temperature (T_c). At this time, the shape memory polymer must have a chemically crosslinked network structure because it should recover to a permanent shape according to its elasticity.

Conventional LCNs and thermoset shape memory polymers are challenging to transform further via reprocessing or recycling once the initial shape is fixed after manufacturing. When dynamic covalent bonds are introduced into existing LCNs or thermosetting shape memory polymers, they can overcome the aforementioned disadvantages by additional deformation, reprocessing, welding, and recycling [3] (Figure 1.4). In addition, dynamic covalent polymer network (DCPN)-based LCNs or thermally adaptive shape memory polymers can additionally control shape morphing via temperature changes. However, since the heat application is

6

challenging to induce selective dynamic covalent bond exchange and shape morphing locally, manufacturing and precise motion control of complex 3D structures capable of selectively remote control in response to various external stimuli are required. Recently, polymeric materials containing fillers or dyes that induce a photothermal effect in response to light have been reported among external stimuli [42]. In addition, polymers that can induce shape morphing in response to moisture and pH have been reported [43,44]. However, DCPN-based 3D soft robots are manufactured by welding or adding adhesive, and research on the facile transformation of permanent 3D structures should be conducted.

1.3. Sulfur-Rich Copolymers for Infrared Imaging

The infrared (IR) region is primarily divided into three categories: near wave infrared (NIR), mid wave infrared (MWIR), and long wave infrared (LWIR). IR optical materials transmit the light of MWIR and LWIR that are difficult to see with the human eye and are used to identify objects in dark situations. Especially, IR lenses are used as an indispensable material for medical (e.g., thermal imaging for COVID-19 screening), transportation (e.g., night vision for autonomous driving), and military (e.g., thermal sensing for missile detection) applications [40]. Chalcogenide is a material that contains one or more elements, such as sulfur (S), selenium (Se), and tellurium (Te), among group 16 elements, excepting oxygen (O). Because the chalcogenide has high infrared transmittance and refractive index (n) according to Lorentz-Lorenz's formula, optical materials for night vision or thermal cameras with high transmittance in the MWIR and LWIR region include crystalline or non-oxide chalcogenide glasses such as ZnS, ZnSe, and Ge [45]. However, such chalcogenide glasses are difficult to process and expensive to reprocess once broken; applying it as a low-cost human body sensor for smart home appliances and building lighting used in real life is challenging. Therefore, developing low-cost IR optical materials with facile processing is required.

Low-cost elemental sulfur is produced on a large scale as a petroleum waste

byproduct in the hydrodesulfurization process of crude oil, with 80 million tons annually. In 2013, Pyun *et al.* reported poly(S-*r*-DIB) by inverse vulcanization of elemental sulfur using 1,3-diisopropenylbenzene (DIB) [46]. Sulfur is the lightest chalcogen element with high polarity and molar refractive index [47]. Besides, transmittances of sulfur-rich copolymers are very high in the IR region due to the low phonon energy between polysulfide bonds [48]. Based on the dynamic polysulfide bond exchange, sulfur-rich copolymers are even facile to reprocess and self-healable. With these intrinsic characteristics, low-cost sulfur-rich copolymers with excellent IR optical properties showed great potential for high-value applications in IR optical materials (Figure 1.5). However, as the sulfur content increases, the IR optical properties improve, but there is a trade-off relationship in which the thermomechanical properties decrease. Therefore, research on sulfur copolymers with enhanced thermomechanical properties with increasing sulfur content is required.

1.4. Motivation

Dynamic covalent polymer networks (DCPN) based on dynamic covalent bonds showed great promise for practical soft robotics applications. For soft robotics to be further developed, it must be implemented as a 3D structure rather than a simple 2D film shape. On the one hand, a method of fabricating a 3D structure from 2D films via adhesive, welding, and post-polymerization processes have been reported in existing soft robotics applications (Figure 1.6) [49-51]. However, by using adhesive materials, it is difficult to fabricate complex 3D structures. Transforming 3D structures into another structure should accompany the complicated process of removing the adhesive after the fabrication. On the other hand, it is a method of realizing a 3D structure by chemical welding through dynamic covalent bonding between DCPNs. However, once welded polymers have limitations in being difficult to separate again, and it is difficult to remanufacture them into other structures [50]. Although DCPNs can be newly manufactured after reprocessing using the dynamic covalent bond exchange, there still have a challenge that requires a very complicated process. We studied a dual crosslinking system to enable reversible assembly between liquid crystal polymers. RM257, a reactive mesogen, was used to maintain the permanent crosslinked structure of liquid crystal vitrimer. In addition, we confirmed that reversible assembly and disassembly

between interfaces of liquid crystal vitrimer films is enabled by MBTA crosslinker, which is capable of dynamic allyl sulfide bond exchange.

The polymeric materials that consist of the soft robot should easily be assembled into a 3D structure without welding or adding adhesive. Meanwhile, the assembled 3D robots should have the rigid stiffness of a rigid robot while having a pliable stiffness enough to grip a deformable object so that it can be driven adaptively in a confined environment [29,52,53]. Polymeric materials composing general soft robots have only one stiffness mode, rigid or pliable. However, developing highly adaptable polymeric materials capable of stiffness modulation for a rigid or pliable state is very challenging. In this regard, smart polymeric materials showing various stiffness using hydrogen bonding or ionic crosslinking of linear polymers have been reported [54,55]. However, these materials have problems with inferior physical properties at low stiffness and are difficult to utilize for soft robotics applications composed of 3D structures. Therefore, we synthesized an excess poly(thiourethane) vitrimer composed of dynamic thiourethane bonds and studied vitrimer properties, variable stiffness, and reversible assembly properties.

The DCPNs can also be applied to IR optics. Inverse vulcanized sulfur-rich copolymers, which can polysulfide bond exchange, have a trade-off relationship between IR optical and thermomechanical properties. Increasing the sulfur content increases the IR transmittance and refractive index, enhancing IR optical properties.

1 1

On the contrary, the thermomechanical properties are reduced since the crosslinker content is lowered. Hence, a crosslinker with more functional groups than a conventional crosslinker was used to increase the degree of crosslinking [56]. In addition, a crosslinker capable of self-crosslinking was introduced to improve thermomechanical properties [57]. However, these sulfur-rich copolymers are also challenging because their thermomechanical properties still need to be high when a large amount of sulfur is contained. Therefore, we introduced a self-crosslinkable crosslinker with three functional groups and studied a phase-separated sulfur-rich copolymer structure. We resolved the trade-off conundrum between IR optical properties dependent on sulfur content and thermomechanical properties dependent on crosslinker content.

1.5. References

[1] G. M. Scheutz, J. J. Lessard, M. B. Sims, B. S. Sumerlin, *J. Am. Chem. Soc.* **2019**, *141*, 16181.

[2] D. Montarnal, M. Capelot, F. Tournilhac, L. Leibler, *Science* **2011**, *334*, 965–968.

[3] N. Zheng, Y. Xu, Q. Zhao, T. Xie, *Chem. Rev.* **2021**, *121*, 1716–1745.

[4] M. Capelot, M. M. Unterlass, F. Tournilhac, L. Leibler, *ACS Macro Lett.* **2012**, *1*, 789.

[5] J. Joe, J. Shin, Y. S. Choi, J. H. Hwang, S. H. Kim, J. Han, B. Park, W. Lee, S. Park, Y. S. Kim, *Adv. Sci.* **2021**, *8*, 2103682.

[6] C. Taplan, M. Guerre, C. N. Bowman, F. E. Du Prez, *Macromol. Rapid Commun.* **2021**, *42*, 2000644.

[7] W. Denissen, G. Rivero, R. Nicolay, L. Leibler, J. M. Winne, F. E. Du Prez, *Adv. Funct. Mater.* **2015**, *25*, 2451–2457.

[8] M. Röttger, T. Domenech, R. van der Weegen, A. Breuillac, R. Nicolaÿ, L. Leibler, *Science* **2017**, *356*, 62–65.

[9] C. A. Tretbar, J. A. Neal, Z. Guan, *J. Am. Chem. Soc.* **2019**, *141*, 16595–16599.

[10] N. Zheng, Z. Fang, W. Zou, Q. Zhao, T. Xie, *Angew. Chem. Int. Ed.* **2016**, *55*, 11421–11425

[11] D. J. Fortman, J. P. Brutman, C. J. Cramer, M. A. Hillmyer, W. R. Dichtel, *J. Am. Chem. Soc.* **2015**, *137*, 14019.

[12] S. Ji, X. Wu, Y. Jiang, T. Wang, Z. Liu, C. Cao, B. Ji, L. Chi, D. Li, X. Chen, *ACS Nano* **2022**, *16*, 16833–16842

[13] H. Ying, Y. Zhang, J. Cheng, *Nat. Commun.* **2014**, *5*, 3218.

[14] A. Erice, A. Ruiz de Luzuriaga, J. M. Matxain, F. Ruipérez, J. M. Asua, H.-J. Grande, A. Rekondo, *Polymer* **2018**, *145*, 127.

[15] H. Feng, N. Zheng, W. Peng, C. Ni, H. Song, Q. Zhao, T. Xie, *Nat. Commun.* **2022**, *13*, 397.

[16] L. Li, X. Chen, J. M. Torkelson, *Macromolecules* **2019**, *52*, 8207– 8216.

[17] C. H. Cui, X. X. Chen, L. Ma, Q. Y. Zhong, Z. Li, A. Mariappan, Q. Zhang, Y. L. Cheng, G. He, X. M. Chen, Z. Dong, L. An, Y. F. Zhang, *ACS Appl. Mater. Interfaces* **2020**, *12*, 47975.

[18] Y. Xue, C. Li, W. Wang, Z. Liu, Z. Guo, J. Tan, Q. Zhang, *Macromol. Rapid Commun.* **2022**, *43*, 2100510.

[19] J. J. Griebel, N. A. Nguyen, A. V. Astashkin, R. S. Glass, M. E. Mackay, K. Char, J. Pyun, *ACS Macro Lett.* **2014**, *3*, 1258–1261.

[20] O. R. Cromwell, J. Chung, Z. Guan, *J. Am. Chem. Soc.* **2015**, *137*, 6492–6495.

[21] Q. Shi, K. Yu, X. Kuang, X. Mu, C. K. Dunn, M. L. Dunn, T. Wang, H. Jerry Qi, *Mater. Horiz.* **2017**, *4*, 598

[22] Q. Chen, X. Yu, Z. Pei, Y. Yang, Y. Wei, Y. Ji, *Chem. Sci.* **2017**, *8*, 724.

[23] Y. Yang, Z. Q. Pei, Z. Li, Y. Wei, Y. Ji, *J. Am. Chem. Soc.* **2016**, *138*, 2118.

[24] E. C. Davidson, A. Kotikian, S. Li, J. Aizenberg, J. A. Lewis, *Adv. Mater.* **2020**, *32*, 1905682.

[25] S. Choi, B. Park, S. Jo, J. H. Seo, W. Lee, D.-G. Kim, K. B. Lee, Y. S. Kim, S. Park, *Adv. Eng. Mater.* **2022**, *24*, 2101497

[26] X. Kuang, S. Wu, Q. Ze, L. Yue, Y. Jin, S. M. Montgomery, F. Yang, H. J. Qi, R. Zhao, *Adv. Mater.* 2021, 2102113

[27] Y. Yang, H. Wang, S. Zhang, Y. Wei, X. He, J. Wang, Y. Zhang, Y. Ji, *Matter.* **2021**, *4*, 3354–3365

[28] K. Yu, Q. Shi, M. L. Dunn, T. Wang, H. J. Qi, *Adv. Funct. Mater.* **2016**, *26*, 6098–6106

[29] D. Rus, M. T. Tolley, *Nature* **2015**, *521*, 467.

[30] Q. He, Z. Wang, Y. Wang, Z. Song, S. Cai, *ACS Appl. Mater. Interfaces* **2020**, *12*, 35464–35474.

[31] H. Zeng, P. Wasylczyk, D. S. Wiersma, A. Priimagi, *Adv.Mater.* **2018**, *30*, 170355.

[32] Q. He, Z. Wang, Y. Wang, A. Minori, M. Tolley, S. Cai, *Sci. Adv.* **2019**, *5*, eaax5746.

[33] B. Shin, J. Ha, M. Lee, K. Park, G. H. Park, T. Choi, K.-J. Cho, H.-Y. Kim, *Sci. Robot.* **2018**, *3*, eaar2629.

[34] J. Zhang, Y. Guo, W. Hu, R. H. Soon, Z. S. Davidson, M. Sitti, *Adv. Mater.* **2021**, *33*, 2006191.

[35] A. Kotikian, C. McMahan, B. C. Davidson, J. M. Muhammad, R. D. Weeks, C. Daraio, J. A. Lewis, *Sci. Robot.* **2019**, *4*, eaax7044.

[36] C. Wang. K. Sim, J. Chen, H. Kim, Z. Rao, Y. Li, W. Chen, J. Song, R. Verduzco, C. Yu, *Adv. Mater.* **2018**, *30*, 1706695.

[37] T. J. White, D. J. Broer, *Nat. Mater.* **2015**, *14*, 1087–1098.

[38] R. Coulson, C. J. Stabile, K. T. Turner, C. Majidi, *Soft Robot.* **2022**, 9, 189–200.

[39] C. Ah, X. Liang, S. Cai. *Adv Mater. Technol.* **2019**, *4*, 1900185.

[40] T. J. White, D. J. Broer, *Nat. Mater.* **2015**, *14*, 1087–1098.

[41] Q. Zhao, H. J. Qi, T. Xie, *Prog. Polym. Sci.* **2015**, *79*, 49–50.

[42] B. Zuo, M. Wang, B.-P. Lin, H. Yang, *Nat. Commun.* **2019**, *10*, 4539.

[43] X. Zheng, S. Guan, C. Zhang, T. Qu, W. Wen, Y. Zhao, A. Chen, *Small* **2019**, 1900110.

[44] A. H. Gelebart, D. J. Mulder, G. Vantomme, A. Schenning, D. J. Broer, *Angew. Chem., Int. Ed.* **2017**, *56*, 13436.

[45] M. Vollmer, K. -P. Möllmann, *Infrared Thermal Imaging,* Wiley-VCH Verlag

GmbH, **2017**.

[46] W. J. Chung, J. J. Griebel, E. T. Kim, H. Yoon, A. G. Simmonds, H. J. Ji, P. T. Dirlam, R. S. Glass, J. J. Wie, N. A. Nguyen, B. W. Guralnick, J. Park, Á. Somogyi, P. Theato, M. E. Mackay, Y.-E. Sung, K. Char, J. Pyun, *Nat. Chem.* **2013**, *5*, 518–524.

[47] K. Choi, W. Jang, W. Lee, J. S. Choi, M. Kang, J. Kim, K. Char, J. Lim, S. G. Im, *Macromolecules* **2022**, 55, 7222–7231

[48] T. S. Kleine, T. Lee, K. J. Carothers, M. O. Hamilton, L. E. Anderson, L. Ruiz Diaz, N. P. Lyons, K. R. Coasey, W. O. Parker Jr, L. Borghi, M. E. Mackay, K. Char, R. S. Glass, D. L. Lichtenberger, R. A. Norwood, J. Pyun, *Angew. Chem. Int. Ed.* **2019**, *58*, 17656–17660

[49] M. P. da Cunha, S. Ambergen, M. G. Debije, E. F. G. A. Homburg, J. M. J. den Toonder, A. P. H. J. Schenning, *Adv. Sci.* **2020**, *7*, 1902842.

[50] Y. Zhang, Z. Wang, Y. Yang, Q. Chen, X. Qian, Y. Wu, H. Liang, Y. Xu, Y. Wei, Y. Ji, *Sci. Adv.* **2020**, *6*, eaay8606.

[51] L. Chen, M. Wang, L. X. Guo, B. P. Lin, H. Yang, *J. Mater. Chem. C* **2018**, *6*, 8251.

[52] C. Laschi, B. Mazzolai, M. Cianchetti, *Sci. Rob.* **2016**, *1*, eaah3690.

[53] Y. Wei, Y. Chen, T. Ren, Q. Chen, C. Yan, Y. Yang, Y. Li, *Soft Rob.* **2016**, *3*, 134–143.

[54] M.-H. Zhang, C.-H. Li, J.-L. Zuo, *Chem. Eng. J.* **2021**, *433*, 133840.

[55] D. Cao, J. G. Martinez, E. S. Hara, E. W. H. Jager, *Adv. Mater.* **2022**, *34*, 2107345.

[56] T. S. Kleine, N. A. Nguyen, L. E. Anderson, S. Namnabat, E. A. LaVilla, S. A. Showghi, P. T. Dirlam, C. B. Arrington, M. S. Manchester, J. Schwiegerling, R. S. Glass, K. Char, R. A. Norwood, M. E. Mackay, J. Pyun, *ACS Macro Lett.* **2016**, *5*, 1152–1156.

[57] S. Park, D. Lee, H. Cho, J. Lim, K. Char, *ACS Macro Lett.* **2019**, *8*, 1670–1675.
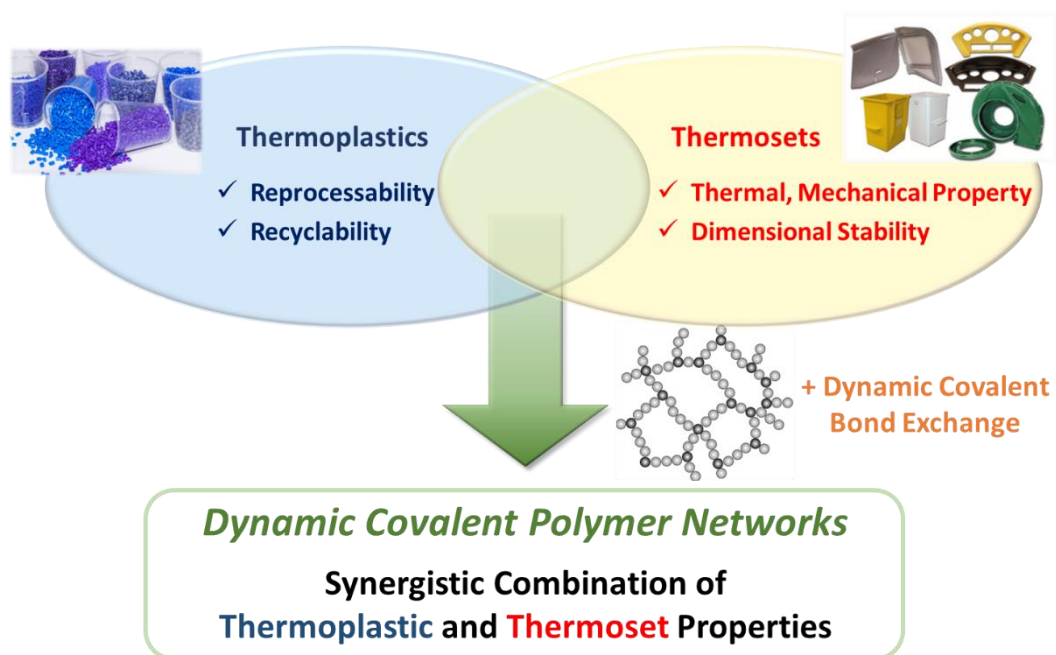
Figure 1.1. Schematic illustration of dynamic covalent polymer networks (DCPN) with synergistic combination of thermoplastic and thermoset properties via dynamic covalent bond exchange.
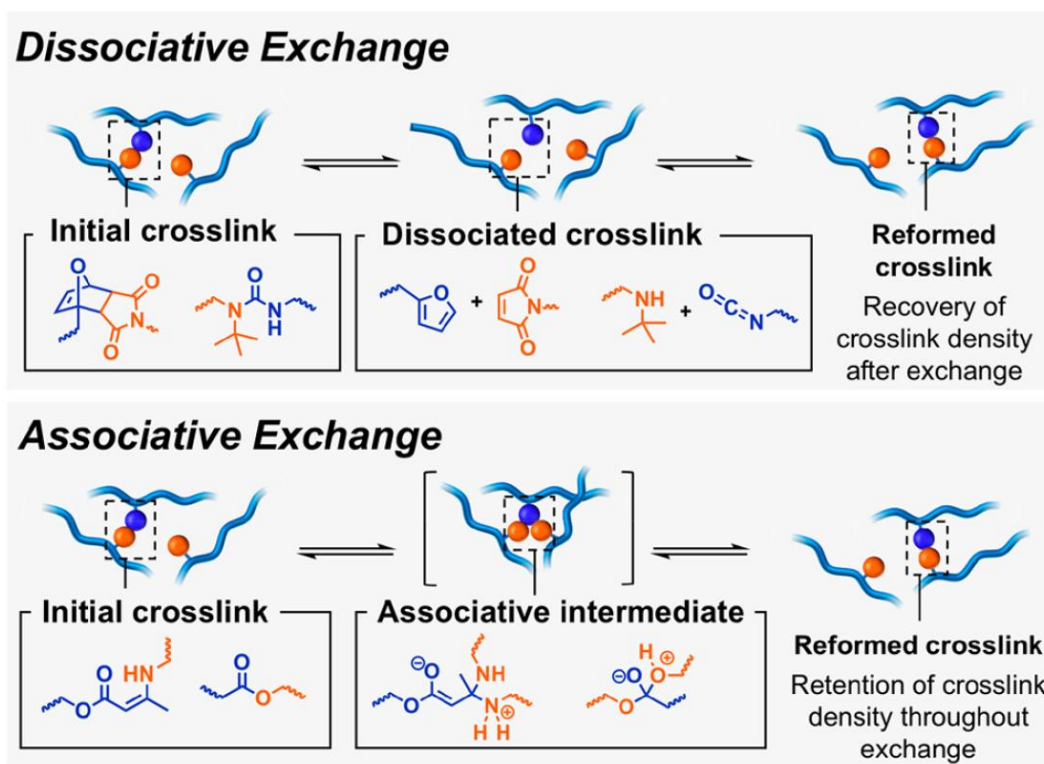
Figure 1.2. Schematic illustration of dissociative and associative bond exchange pathways for DCPNs [1].
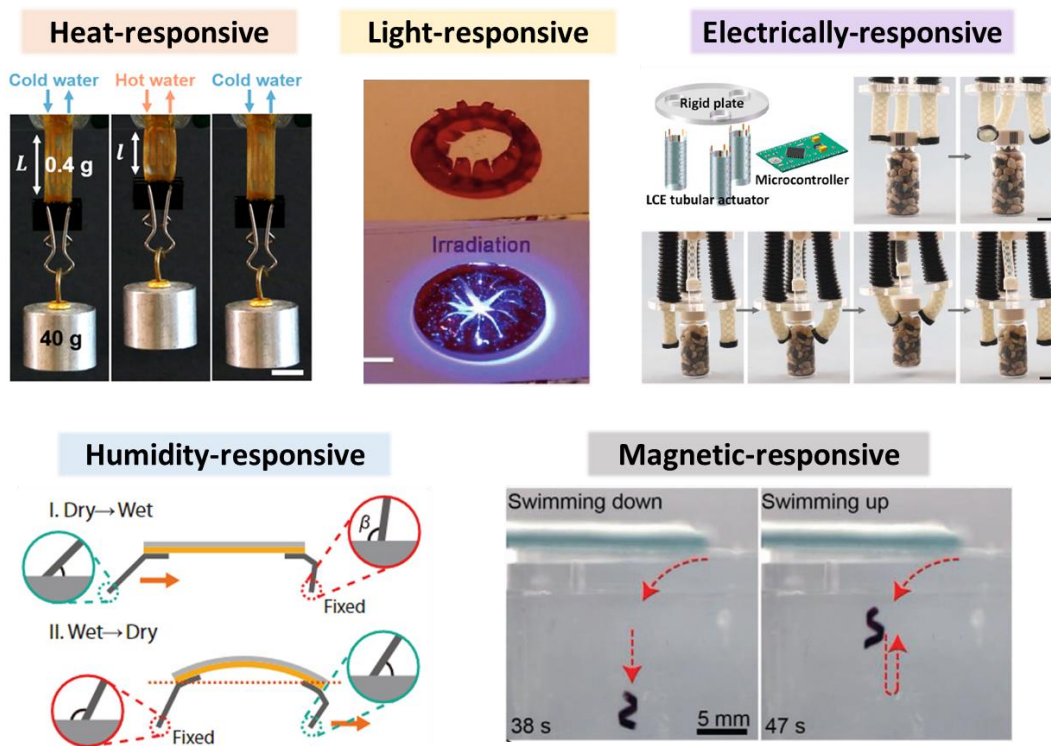
Figure 1.3. Various stimulus-responsive soft robots [30-34].
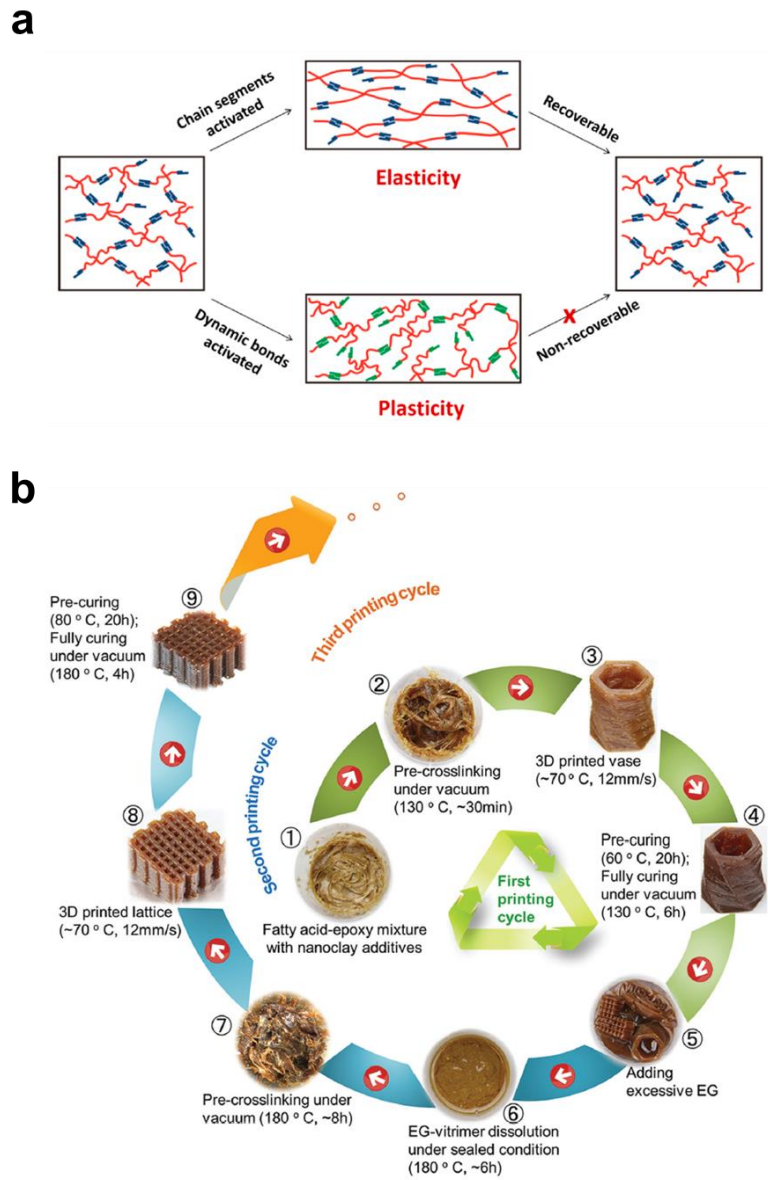
Figure 1.4. Schematic illustration of (a) elasticity and plasticity of DCPN with shape memory properties and (b) crosslinking / dissolution / recrosslinking cycle of recyclable 3D printing of nanoclay-reinforced vitrimer epoxy [3,21].
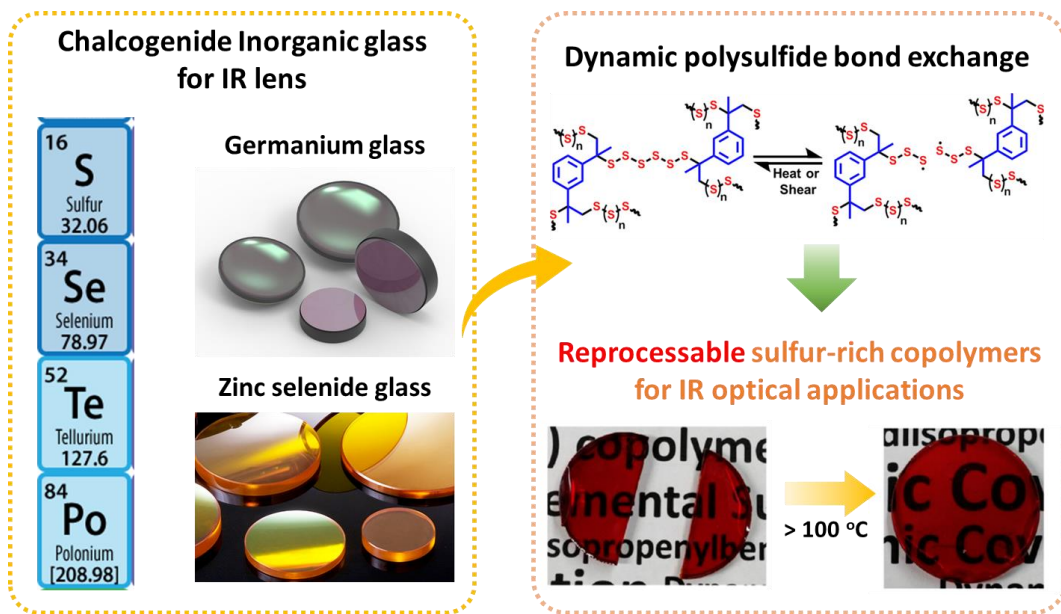
Figure 1.5. Schematic illustration of chalcogenide inorganic glass and reprocessable sulfur-rich copolymers for IR lens [19,45,46].
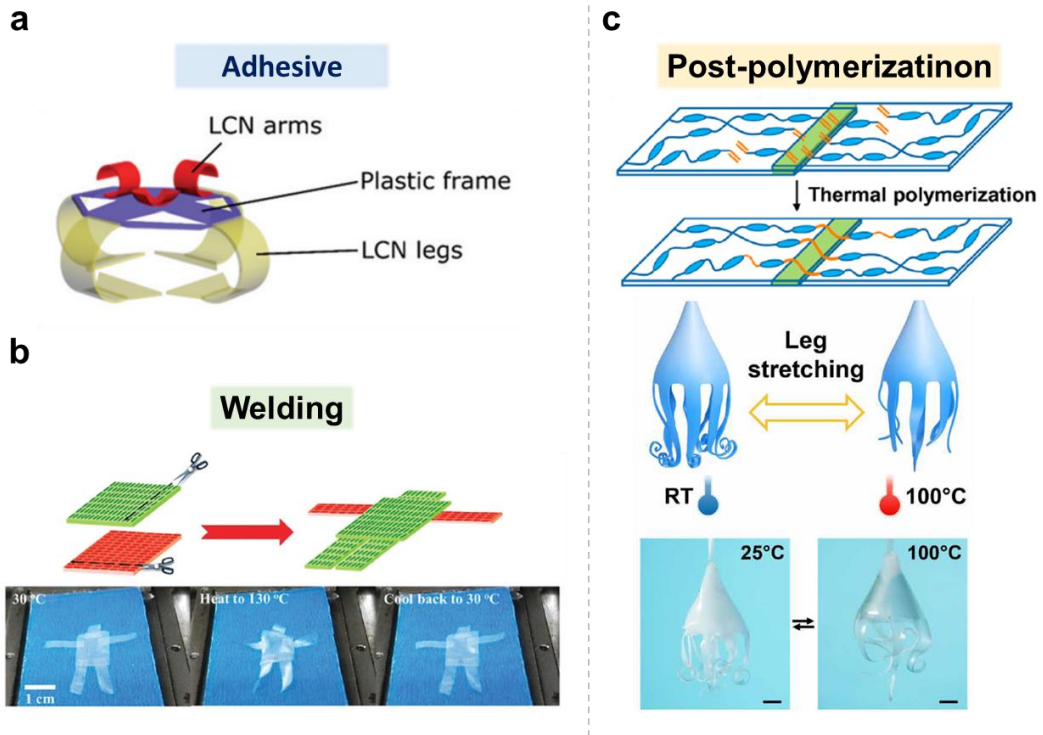
Figure 1.6. Fabricating 3D structures from 2D films via (a) adhesive, (b) welding, and (c) post-polymerization processes [49-51].

Chapter 2

Dynamic Photo-Controllable Liquid Crystalline Networks for Monolithically Assembled 3D Soft Transformable Robot

2.1. Introduction

There have been extensive studies on soft robots made of various soft polymeric materials to complement conventional rigid robots [1-7]. Among polymeric materials, liquid crystalline networks (LCNs) have mainly been investigated for soft robotic applications [8-13]. Such materials have the advantage of mimicking biological systems on a small scale, being stimuli-responsive, and can be operated according to the orientation state of the liquid crystalline moieties inside [14-20]. When the ordered orientation of the liquid crystalline moieties in the LCNs is distorted to an isotropic state by an external stimulus, actuation occurs because the prevailing form is deformed [21-23]. Upon removing the external stimulus, the LCNs fully recover their original orientation state inside and thus the external forms owing to the stably crosslinked network structure [3,9,10,22]. These systems can be actuated using various external stimuli such as light [14,24-26], heat [27], electricity [28,29], and magnetism [30,31].

Among the various actuation methods, light-driven actuation has the advantage of enabling the selective and independent movement of LCNs by an appropriate wavelength of irradiating light and precise remote control over their movement according to the light intensity [12,21,32]. There are two ways to achieve

2 6

reversible actuation of LCNs by temporarily distorting the orientation state inside under a specific wavelength of light irradiation: (i) the photomechanical method using an azobenzene-containing dopant or crosslinker, relying on the trans–cis isomerization process of the azobenzene moiety [33], and (ii) the photothermal method using an additive capable of photothermal conversion to generate heat [34]. The light-driven LCNs were first applied in soft robotic systems based on two-dimensional (2D) film operation [8,9,15,26]. For instance, Priimagi et al. showed that an LCN containing an azobenzene-based dopant dye could actuate upon visible light irradiation, and demonstrated its possible applications for artificial flytraps [16] and self-regulating irises [35]. More Recently, Yang et al. reported a multi-directional walking soft robot utilizing visible/near-infrared tri-wavelength-modulated 2D LCNs [24].

Although these examples are successful demonstrations of light-driven LCNs for soft robotic applications, more complex three-dimensional (3D) structures of LCN-based soft robots are required to achieve movement with multiple degrees of freedom in various environments. Schenning et al. reported a 3D soft-transport robot composed of multiple LCN actuators with two different azobenzene derivatives [25]. However, the actuating LCN arms and legs of the soft transporting robot were non-monolithic and simply attached to a non-actuated polymeric hub using double-sided tape, which may lead to a decrease in its long-term structural

stability. Recently, chemical welding processes, which form covalent bonds at the interfaces between LCN films without additional adhesives, have been applied to construct monolithic, complex 3D soft robot structures from 2D building blocks [13,36,37]. Moreover, dynamic covalent bond exchanges in LCNs can also be used to fabricate LCN-based soft robots exhibiting reconfigurable shapes and reprogrammable actuation [33,38]. Ji et al. demonstrated the expansion of the limited movement of LCN-based soft robots by the construction and reconfiguration of monolithic 3D structures utilizing various dynamic covalent bond exchanges, such as transesterification [39], dynamic siloxane [40], and allyl sulfide bond exchanges [38]. However, certain challenges remain in the development of advanced soft robots. For example, once a 3D monolithic structure capable of a specific movement is fabricated via chemical welding-based assembly of the LCNs, it is impossible to transform it into a new 3D structure capable of another movement through the disassembly-reassembly process [13,36]. Furthermore, systems that can be shape-reconfigured require additional processes, such as thermal treatment, and the selective reconfiguration of detailed parts is challenging [41]. Thus, there remain opportunities to develop lego-like reversible interfacial assembly systems based on LCNs with a controlled dynamic covalent polymer network architecture.

2 8

Herein, we demonstrate a monolithically assembled 3D soft transformable robot based on dual-crosslinked photo-controllable LCNs (pc-LCNs) with reversible assembly/disassembly and shape reconfiguration capabilities. The dual-crosslinked pc-LCN consists of an optimized ratio of static mesogenic and dynamic allyl sulfide crosslinks. Dynamic covalent bond exchange reactions at the interface of two pc-LCN films held in contact can be controlled through ultraviolet (UV) irradiation while maintaining the overall network stability and molecular alignment by static mesogenic crosslinks, thereby leading to controllable reversible assembly/disassembly of the LCN films. Remarkably, because the reversible assembly/disassembly process does not require an additional adhesive component, monolithic 3D architectures composed of only pc-LCNs were fabricated. Dynamic covalent bond exchanges also enable the cumulative shape reconfiguration of pc-LCN films for structural versatility. Meanwhile, visible-light-responsive dopant dyes are introduced into the pc-LCNs to induce their actuation behaviors under visible-light irradiation so that the UV-controlled 3D shape formation and visible-light-controlled actuation processes do not affect each other. Based on these characteristics, pc-LCN building blocks can be assembled and consecutively transformed into various 3D soft robots with versatile motion capabilities, including rolling, gripping, and cargo transport in multiple directions.

2.2. Results and Discussion

2.2.1. Preparation of a photo-controllable LCN with static and dynamic dual-crosslinks

This study presents a novel concept of lego-like reversible assembly/disassembly and consecutive shape reconfiguration of 2D LCN films through controlled dynamic covalent bond exchanges. A key approach to achieving this is to construct a precisely tailored dual-crosslinked network structure comprising both static mesogenic and dynamic allyl sulfide crosslinks. A dual-crosslinked pc-LCN film with blue dopant dye (pc-LCN-B) was prepared from mesogenic monomer (RM105; 63 mol%), static mesogenic crosslinker (RM257; 23.8 mol%), dynamic allyl sulfide crosslinker (MBTA; 10.2 mol%), photoinitiator (Irgacure 651; 2 mol%), and Disperse Blue 14 dye (DB14; 1 mol%) (Figure 2.1). First, RM105, RM257, MBTA, Irgacure 651, and DB14 were stirred in a vial at 80 °C to form a homogeneous mixture. A liquid crystal (LC) cell comprising two glass slides with bottom planar and top homeotropic alignment layer coatings was placed on a hot plate at 80 °C, infiltrated with the prepared mixture, and then cooled naturally to 25 °C at a rate slower than 5 °C min^{-1}. Photopolymerization was performed for 15 min at 25 °C under 20 mW cm^{-2} UV (λ = 365 nm) irradiation.

Finally, the LC cell was carefully opened to obtain a pc-LCN-B film with splay molecular alignment (Figure 2.2 and 2.3) [17,42].

As the maximum absorption wavelength (λ_{max}) of the DB14 dye is 644 nm [43], the splay alignment in pc-LCN-B can be distorted to an isotropic state by increasing the temperature to approximately 70 °C owing to the photothermal effect of DB14 under 660 nm light irradiation (50 mW cm^{-2}) [32]. Thus, the flat pc-LCN-B film exhibits bending actuation upon isotropic transition because the planarily aligned LCN part contracts, whereas the homeotropically aligned LCN part stretches (Figure 2.4). The actuation behavior of the film was found to be maintained when it contained up to 30% of the dynamic allyl sulfide crosslinker (MBTA) with respect to the total content of the crosslinkers (Table 2.1). At an MBTA ratio higher than 30%, actuation is either significantly slower or does not occur at all. This is because the contents of the alignable mesogenic monomer (RM105) and crosslinker (RM257) decreased as the unalignable MBTA content increased. Therefore, to maximize the dynamic bond exchange capability of pc-LCN-B while maintaining the splay molecular alignment for bending actuation, the MBTA content was set to 10.2 mol% with respect to the total LC mixture.

2.2.2. Reversible assembly/disassembly and shape reconfiguration of pc-LCN films

Bowman's group previously demonstrated reversible addition-fragmentation chain transfer (RAFT)-based bond exchange in polymer networks under photoactivated conditions using MBTA as a RAFT-based dynamic covalent crosslinker [44,45]. Once derived from the photoinitiator under light exposure, the radical species reacts with the allyl sulfide moieties of MBTA to generate thiyl radicals, which can subsequently undergo dynamic bond exchange reactions with other allyl sulfide units (Figure 2.5). Although previous studies have proposed the possible utilization of dynamic allyl sulfide crosslinkers for the photoinduced plasticity of polymer networks [38,44-46], the photocontrolled reversible assembly and disassembly of LCNs, as performed in this study, have not yet been reported.

The dual-crosslinked structure, which utilizes a static RM257 crosslinker in addition to a dynamic MBTA crosslinker, is crucial for the realization of reversible assembly/disassembly. As shown in Figure 2.6 and 2.7, dynamic allyl sulfide bond exchanges occur at the interface between two pc-LCN-B films during gentle pressing under UV irradiation (λ = 365 nm, 0.2 W cm^{-2} for 30 s), resulting in a monolithically assembled pc-LCN-B film. In contrast, the RM257-based crosslinked network of pc-LCN-B is chemically stable, even under UV irradiation,

enabling the bulk internal network to withstand tensile stress without breaking. Thus, the assembled pc-LCN-B film can be disassembled into two original pc-LCN-B films by again applying a small tensile stress under UV irradiation ($\lambda = 365$ nm, 0.2 W cm^{-2} for 30 s). Scanning electron microscopy (SEM) analysis revealed that the UV-assembled pc-LCN-B film showed cross-sections that were closely attached and connected to each other at the interface. Nevertheless, the interfacial assembly was neatly separated under UV irradiation and tensile stress (Figure 2.8). In addition, since MBTA contained relatively less than RM257, the self-healing property of pc-LCN by MBTA was not well shown (Figure 2.9).

Lap-shear tests were performed using a dynamic mechanical analyzer (DMA) to confirm the stability of the system formed by the interfacial assembly. Figure 2.10 shows the representative stress-strain curves of a pristine pc-LCN-B film and an assembled film obtained from two partially overlapped pc-LCN-B films, which clearly confirms the stability of the interfacial assembly through dynamic allyl sulfide bond exchanges. The elastic modulus (E) and strain at break (ε_b) values of the assembled sample were relatively larger and smaller than those of the pristine film, respectively, owing to the presence of a partially overlapped area (Figure 2.11 and Table 2.2). Moreover, when the monolithically assembled pc-LCN-B film was stretched by tensile stress in the absence of UV irradiation, the original film part fractured, while the assembled section remained intact (Figure 2.12). When

3 3

physically attached without UV irradiation, the two pc-LCN-B films were readily detached under applied stress because covalent bonds were not formed at the interface (Figure 2.13). Similarly, physically attached LCN-B films without any MBTA crosslinker (i.e., 100% RM257 crosslinker with respect to the total crosslinker content) were found to be detached readily under stress (Figure 2.14). Meanwhile, when the ratio of MBTA with respect to the total content of crosslinkers increased to 100% in the pc-LCNs, the two films were chemically welded by forming strong covalent bonds at the interface under UV treatment, so the fully welded film was fractured instead of delaminating even under careful tensile stress and UV irradiation (Figure 2.15). Therefore, both dynamic allyl sulfide crosslinking and static mesogenic crosslinking should be utilized in the construction of pc-LCNs to achieve photocontrolled reversible assembly and disassembly.

In addition to the reversible assembly/disassembly capability, the shape reconfiguration of pc-LCNs was also found to be possible. This is because network rearrangement and fixation by dynamic covalent bond exchange are more dominant than network stabilization by static covalent crosslinks. The shape reconfiguration mechanism via the photoinduced plasticity of pc-LCNs is shown in Figure 2.16. Upon appropriate reshaping and UV irradiation (0.2 W cm^{-2}, 40 s), the pc-LCN-B film can be consecutively reconfigured to different shapes by relaxing the

mechanically induced stress via dynamic allyl sulfide bond exchanges. For example, as shown in Figure 2.17, the pristine pc-LCN-B film was first deformed using a tweezer and UV-irradiated to reconfigure it into a curved shape. The curved film was rolled around a glass pipette and irradiated with UV light to transform it into a spiral shape. Subsequently, the spiral-shaped pc-LCN-B was placed into a heart-shaped Teflon template to create a heart shape, followed by UV irradiation to fix the heart shape. Finally, the original 2D flat film was regenerated using the same reshaping and UV irradiation processes. We also confirmed that shape reconfiguration of pc-LCNs is possible regardless of the presence or type of dopant dye. Details of the photocontrolled shape reconfiguration of the dye-free pc-LCN are presented in Figure 2.18.

It should be noted that the actuation characteristics of pc-LCNs are preserved even while exhibiting reversible assembly/disassembly and shape reconfiguration capabilities. As shown in Figure 2.19, the bending angle for the actuation of the pc-LCN-B film, according to the UV irradiation time, did not change significantly. However, when irradiated continuously for more than 120 s, the bending angle gradually decreased, and this may be because of disruption of the liquid crystalline alignment owing to excess dynamic bond exchanges. Multiple UV irradiations with an interval of 120 s did not appear to affect the liquid crystal alignment, and the decrease in the bending angle was maintained within 5°.

2.2.3. Monolithically assembled, transformable 3D architectures based on pc-LCN-B films

By utilizing both of the above reversible assembly/disassembly and shape reconfiguration capabilities, monolithically assemblable and transformable 3D architectures can be fabricated from 2D pc-LCN-B films. Successive assembly, reconfiguration, actuation, and disassembly of pc-LCN-based monolithic 3D structures were performed to mimic the metamorphosis from a caterpillar to a butterfly (Figure 2.20). The structural complexity increases as the system transforms from the 2D structure of a caterpillar to a chrysalis and then to a butterfly. In addition, when irradiated with 660 nm light, each structure exhibited specific actuation behaviors owing to the disruption of the splay molecular alignment in pc-LCN-B. The photographs in Figure 2.21 show the entire process. The caterpillar-mimic structure was fabricated by alternately assembling four pc-LCN-B building blocks with opposite molecular orientations. Thus, the caterpillar-mimic structure could be actuated by irradiating with 660 nm light (50 mW cm^{-2}) to realize movement similar to crawling. After disassembling the structures under UV irradiation, they were transformed into a more complex 3D chrysalis-mimic structure through additional assembly and shape reconfiguration processes. A Y-shaped flat structure was prepared by assembling eight building blocks of the same

3 6

molecular orientation, which was followed by shape reconfiguration to form the closed chrysalis-like structure. The actuation resembled the opening of chrysalis was then performed by 660 nm light irradiation. Similar to the Y-shaped structure of the chrysalis-mimicking fabrication, a flat butterfly structure was prepared by assembling the eight building blocks of the same molecular orientation. The waist of the butterfly was then reconfigured to form the initial bent structure, opposite to the flapping and bending direction of the wings and antennae, respectively. The butterfly-mimic structure was actuated by 660 nm light irradiation to exhibit the flapping motion. Thus, the same pc-LCN-B films can be utilized as basic building blocks to enable the continuous implementation of various complex 3D architectures that exhibit different actuation behaviors. Such a lego-like, reversible assembly/disassembly process is the main advantage of dual-crosslinked pc-LCNs compared to the irreversible chemical welding-based fabrication methods of LCNs with dynamic covalent bonds [36,37].

2.2.4. Selective visible light responsiveness of pc-LCNs with different dopant dyes

Although a pc-LCN-B film capable of actuation under 660 nm light irradiation was presented in the previous section, the photo-stimuli for actuation do not need

to be limited to specific wavelengths. Rather, the building blocks should be actuated individually and regionally in response to various wavelengths to realize the complex movements of the assembled 3D architectures. We applied three different dopant dyes (including DB14 used for pc-LCN-B) to develop three different pc-LCN building blocks, denoted as pc-LCN-X (where X represents the first letter of the dye color; for example, a sample with a red dye is denoted as pc-LCN-R). DB14 (λ_{max} = 644 nm) in pc-LCN-B acts as a photothermal conversion agent to generate heat for actuation [32], whereas Disperse Red 1 (DR1, λ_{max} = 502 nm) and Disperse Orange 13 (DO13, λ_{max} = 427 nm) induce photomechanical actuations of pc-LCNs through the trans–cis isomerization of the azobenzene moiety (Figure 2.22 and Figure 2.23) [32]. The UV-visible absorption spectra of the dopant dyes and pc-LCN-Xs are displayed in Figure 2.24 [43]. The dye-doped pc-LCN-Xs had similar maximum absorption wavelengths as the dye, except for a slight band shift and broadening [24]. The increasing absorption peak of pc-LCN-Xs below 400 nm was attributed to the remaining Irgacure 651 photoinitiator with an absorption peak at ~350 nm in the samples [47].

The selective actuation behavior of pc-LCNs doped with different dopant dyes under visible light irradiation is presented in Figure 2.25. When irradiated with 532 nm light, only the pc-LCN-R was actuated, while pc-LCN-B and pc-LCN-O remained intact and were actuated only when irradiated with 660 and 405 nm light,

respectively [43]. To determine the degree of actuation over time, the bending angle profiles of pc-LCN-Xs can be obtained by measuring the angle α between l_A and l_H under visible light irradiation, where l_A is the tangent from the middle to the right endpoint of the arc, and l_H is the horizontal baseline (Figure 2.26) [24]. After a certain duration of approximately 35−40 s, each film converged to its maximum bending angle (~40°) regardless of the doped dye type. To further confirm the degree of actuation of pc-LCNs depending on the film thickness, 30, 50, and 80 µm-thick pc-LCN films were prepared. When irradiated by light intensity of 50 mW cm^{-2}, the 30 and 50 µm-thick pc-LCN films exhibited bending actuation, but the 80 µm-thick pc-LCN-B film did not show any actuation behavior, possibly due to the light attenuation (Figure 2.27). It was found that much higher light intensity of 100 mW cm^{-2} should be applied to actuate the 80 µm-thick pc-LCN films. The selective responsiveness of pc-LCN-Xs to light of various wavelengths, along with their reversible assembly/disassembly and shape reconfiguration characteristics, could also play an important role in realizing more advanced 3D soft robots.

2.2.5. Fabrication and movements of 3D soft transformable robot

We demonstrated the exemplary fabrication process and movements of monolithically assembled 3D soft robots, transforming from soft rolling robots to

soft tripod robots and soft grippers, based on dual-crosslinked 2D pc-LCN building blocks. The entire process is presented on a track and consists of four positions: (I) start/finish, (II) transformation, (III) storage, and (IV) obstacle (Figure 2.28). Various movements of pc-LCN-based 3D soft robots, including rolling [48-50], gripping [19,31], loading, unloading [25], and walking [15,51] with switching direction, are achieved on the track through the appropriate transformation process. First, the soft rolling robot moves by rolling from position (I) to position (II). After being transformed into a soft tripod robot and soft gripper at position (II), the gripper grips a black cargo and loads it on the tripod robot. Then, the tripod loaded with the black cargo walks to position (III), unloads it, and walks again in the horizontal direction. While walking, it faces an obstacle at position (IV), switches direction to its lower left, and again walks to the right to arrive at the finish line.

The detailed processes of assembling the robots and their operation on the track are explained by illustrations and photographs (Figure 2.29). The trace coordinates of the movements on the track are plotted in Figure 2.30. Three soft robots with rolling (soft rolling robot), multi-directional walking (soft tripod robot), and loading (soft gripper) capabilities can be transformed into one another. To fabricate 3D soft transformable robots with these characteristics, building blocks were first prepared by appropriately cutting the dye-free pc-LCN film and pc-LCNs with three different dopant dyes. A soft rolling robot can be fabricated using two

rectangular-shaped pc-LCN-B and two T-shaped dye-free pc-LCN building blocks by a photo-controlled assembly process (Figure 2.29a), where the two pc-LCN-B building blocks are assembled to actuate in an S shape by bending in opposite directions. The dye-free pc-LCN building block functions only as a structural part and not for actuation. For example, the frictional force for the effective rolling locomotion of a soft rolling robot can be increased by attaching dye-free pc-LCNs at both ends of the assembled pc-LCN-B [52-54]. Accordingly, when irradiated by 660 nm light, the soft rolling robot moves by continuously rolling from position (I) to position (II). The trace positions generated during the movement of the soft rolling robot are shown in Figure 2.30a. Once it arrives at position (II), the soft rolling robot is disassembled into its building blocks for transformation into a soft tripod robot and a soft gripper.

One of the recovered T-shaped dye-free pc-LCN blocks could be reconfigured into a 3D cube shape with two vacant sides by deformation under UV irradiation. The rectangular pc-LCN-B, pc-LCN-R, pc-LCN-O, and triangular dye-free pc-LCN building blocks, along with the open cube-shaped blocks, were assembled together into the soft tripod robot via appropriate masking and UV irradiation (Figure 2.29b and 2.31a). The three legs made of dye-doped pc-LCNs exhibited bending actuation downwards for walking locomotion. The vacant side of the open cube for unloading the cargo was located opposite to the pc-LCN-B block of the

4 1

soft tripod robot. The soft gripper could also be monolithically assembled from four dye-doped pc-LCN building blocks using a similar fabrication procedure (Figure 2.31b). One pc-LCN-R block was installed as the handle to enable the forward bending movement, one pc-LCN-B unit was used as the main backbone so that the entire soft gripper could be closed, and two pc-LCN-O units were applied as the two arms for the grip motion. Upon irradiating 660, 532, and 405 nm wavelengths simultaneously, the soft gripper can pick up black cargo. After its movement to the soft tripod robot, the grip was released by stopping the light irradiation, and the black cargo was loaded on the open cube-shaped basket of the soft tripod robot. Subsequently, the black cargo-loaded soft tripod robot walked from position (II) to position (III) in the left diagonal direction under 532 nm light irradiation (Figure 2.29c). The trace position of the soft tripod robot upon 532 nm light irradiation is plotted in Figure 2.30b. At position (III), one leg made of pc-LCN-B block in the soft tripod robot can be bent by irradiating with 660 nm light. As the soft tripod robot inclines, the black cargo falls into the storage area through the open side of the dye-free pc-LCN basket. After completing the unloading task, the soft tripod robot walked to the right to return to the starting point by irradiation with 660 nm light. Given that there is an obstacle at position (IV) on the return path, the soft tripod robot can switch the walking direction by 405 nm light irradiation to move diagonally to the left, after which it then walks again to the right by 660 nm light

irradiation to reach the finish position (I). The trace position for reaching the finish

line by switching direction from position (III) is plotted in Figure 2.30c.

2.3. Conclusion

In summary, we demonstrated the preparation of photo-controllable LCNs (pc-LCNs) comprising static and dynamic covalent dual-crosslinks for transformable soft robotics. UV-controlled reversible assembly/disassembly and shape reconfiguration of pc-LCNs are achieved by precisely tailoring their network structures. As the static mesogenic crosslinks in the networks are strongly fixed, only the dynamic bond exchanges of allyl sulfide crosslinks occur to reversibly assemble or reconfigure pc-LCN films under UV irradiation. In addition, pc-LCNs contain various visible-light-responsive dopant dyes, and their bending actuation behaviors are selectively controlled by irradiation with visible light having different wavelengths without affecting the UV-responsive dynamic crosslinks. Accordingly, such orthogonally controllable reversible assembly and actuation processes enable the utilization of pc-LCNs as building blocks for monolithically assembled 3D soft transformable robots with versatile motion capabilities. For example, a soft rolling robot that can roll, a soft gripper that can pick up cargo, and a soft tripod robot that can transport cargo in multiple directions can be consecutively constructed from the same pc-LCN building blocks. The developed system is not limited to photo-responsive actuation in this study; thus, we are currently preparing multi-stimuli-responsive LCN building blocks with magnetic and electrical responsiveness for

more advanced 3D soft transformable robots. We also expect that the present work will provide insight into the design and preparation of LCN-based materials for various emerging applications, including four-dimensional (4D) printing and shape-morphing electronics.

2.4. Experimental

Materials: 4-Methoxybenzoic acid 4-(6-acryloyloxyhexyloxy)phenyl ester (RM105, 97%, Synthon Chemicals), 4-bis-[4-(3-acryloyloxypropyloxy)benzoyloxy]-2-methylbenzene (RM257, 97%, Synthon Chemicals), Disperse Red 1 (DR1, dye content:95%, Sigma-Aldrich), Disperse Blue 14 (DB14, dye content:97%, Sigma-Aldrich), Disperse Orange 13 (DO13, dye content:90%, Sigma-Aldrich), 2,2-dimethoxy-2-phenylacetophenone (Irgacure 651, DMPA, 99%, Sigma-Aldrich), planar alignment layer-coated glass ($40 \times 30 \times 0.7$ mm, IDP System), homeotropic alignment layer-coated glass ($30 \times 30 \times 0.7$ mm, IDP System), NOA63 UV-curing epoxy material (Norland Products), and 50 μm spacers (50 μm polymer microspheres, Suzhou Nanomicro Technology Co. Ltd.) were used as received. 2-methylene-propane-1,3-bis(thioethyl acrylate) (MBTA) was synthesized as previously described [55]. All other reagents and solvents were used as received from standard vendors.

Preparation of pc-LCN film: For the LC cell fabrication, a planar alignment layer on a glass substrate (4×3 cm) was used as the lower surface, while a homeotropic alignment layer on a glass substrate (3×3 cm) was used as the upper surface. The homeotropic alignment layer-coated glass was placed above the planar layer-coated

4 6

glass with polymer bead spacers, NOA63 was added at the four corners, and then cured using a 20 mW cm^{-2} UV LED (λ = 365 nm) to prepare a 50-µm-thick liquid crystal cell. To prepare pc-LCN-B, RM105 (0.4 g, 63 mol%), RM257 (0.22 g, 23.8 mol%), MBTA (0.05 g, 10.2 mol%), DB14 (0.004 g, 1 mol%), and Irgacure 651 (0.01 g, 2 mol%) were placed in a vial equipped with a magnetic stirring bar, followed by stirring at 80 ℃ for 30 min to obtain a homogeneous reactive LC

mixture [16,38]. The prepared LC cell was placed on a hot plate at 80 °C, and the LC mixture was infiltrated into the cell through capillary force. After infiltration, the LC cell was naturally cooled to 25 °C at a rate lower than 5 °C min^{-1}. UV-induced photopolymerization was then performed at 25 °C (365 nm, 20 mW cm^{-2}) for 15 min. The crosslinked pc-LCN film inside the LC cell was carefully separated using a blade. pc-LCN-R and pc-LCN-O were prepared using the same procedure but with different dyes, DR1 (1 mol%) and DO13 (1 mol%), respectively.

Reversible assembly-disassembly and shape reconfiguration of pc-LCN films: The pc-LCN films were partially overlapped (ca. 1.0–2.5 mm) and gently pressed, followed by UV irradiation (0.2 W cm^{-2}, 30 s) with masking films installed in areas that did not overlap (Figure 2.7). The pc-LCN assembled via dynamic allyl sulfide bond exchange reactions at the interface was obtained after UV exposure. In order to disassemble the pc-LCN film, the overlapped area was again irradiated by UV

light (0.2 W cm^{-2}, 30 s) while simultaneously pulling apart both ends of the assembled pc-LCN film gently. For shape reconfiguration, the pristine pc-LCN film was first deformed using appropriate support, then UV light (0.2 W cm^{-2}, 30 s) was irradiated on the physically deformed pc-LCN to induce dynamic allyl sulfide bond exchange reactions to relax the stress (Figure 2.17).

Fabrication of soft rolling robot, soft tripod robot, and soft gripper: To fabricate a soft rolling robot, building blocks were first prepared by cutting pc-LCN films into appropriate shapes. The pc-LCN-B main blocks were assembled to actuate in an S manner by bending them in opposite directions. T-shaped dye-free pc-LCN blocks were attached at both ends of the pc-LCN-B assembly to generate frictional force upon rolling actuation (Figure 2.28a). Before assembling the soft tripod robot, the building blocks were recovered by disassembling the soft rolling robot. One of the T-shaped blocks was reconfigured into a 3D cube with two vacant sides by deformation under UV irradiation. Then, the rectangular pc-LCN-B, pc-LCN-R, pc-LCN-O blocks, and triangular dye-free pc-LCN blocks were assembled together into the soft tripod robot via appropriate masking and UV irradiation (Figure 2.30a). The vacant sides of the open cube were located opposite the pc-LCN-B block of the soft tripod robot. To assemble the soft gripper, pc-LCN-B, pc-LCN-R, and pc-LCN-O building blocks were cut into different sizes of 10 mm × 1 mm, 5 mm × 2 mm,

and 4 mm $\times$ 1 mm, respectively, and assembled using a similar fabrication procedure (Figure 2.30b).

Instrumentation and characterization techniques: UV-visible-near-infrared spectra were recorded on a Hitachi U-4100 spectrometer. The temperature changes of the pc-LCNs during visible-light irradiation were monitored using an infrared camera (T300, FLIR). The following single-wavelength laser sources (CNI Optoelectronics Technology Co., Ltd.) were applied for visible-light actuation: an MDL-III-660 laser (660 nm, maximum intensity = 0.5 W cm^{-2}), MGL-FN-532 laser (532 nm, maximum intensity = 0.5 W cm^{-2}), and MDL-III-405 laser (660 nm, maximum intensity = 0.5 W cm^{-2}). A UV LED (365 nm, maximum intensity = 8 W cm^{-2}, FE400, Phoseon Technology) was used for the photopolymerization, reconfiguration, and reversible assembly disassembly. Tensile testing of pc-LCN films was performed by dynamic mechanical analysis (DMA, TA Instruments, Q800) at 25 °C and a strain rate of 0.04 min^{-1}. Scanning electron microscopy (SEM) was conducted using Tescan VEGA-II/LSV equipment. Polarized optical microscopy (POM) was performed using a Nikon 50iPol microscope.

2.5. References

[1] R. F. Shepherd, F. Ilievski, W. Choi, S. A. Morin, A. A. Stokes, A. D. Mazzeo, X. Chen, M. Wang, G. M. Whitesides, *Proc. Natl. Acad. Sci.* **2011**, *108*, 20400-20403.

[2] Y. Yu, M. Nakano, T. Ikeda, *Nature* **2003**, *425*, 145.

[3] M. del Pozo, J. A. H. P. Sol, A. P. H. J. Schenning, M. G. Debije, *Adv. Mater.* **2021**, 2104390.

[4] D. Rus, M. T. Tolley, *Nature* **2015**, *521*, 467-475.

[5] S. Kim, C. Laschi, B. Trimmer, *Trends Biotechnol.* **2013**, *31*, 287-294.

[6] C. Majidi, *Soft Robotics* **2014**, *1*, 5-11.

[7] J. Liu, Y. Gao, Y.-J. Lee, S. Yang, *Trends in Chem.* **2020**, *2*, 107-122.

[8] R. R. Kohlmeyer, J. Chen, *Angew. Chem. Int. Ed.* **2013**, *52*, 9234-9237; *Angew. Chem.* **2013**, *125*, 9404-9407.

[9] S. Iamsaard, S. J. Aβhoff, B. Matt, T. Kudernac, J. J. L. M. Cornelissen, S. P. Fletcher, N. Katsonis, *Nat. Chem.* **2014**, *6*, 229-235.

[10] T. J. White, D. J. Broer, *Nat. Mater.* **2015**, *14*, 1087-1098.

[11] T. Ube, T. Ikeda, *Adv. Optical Mater.* **2019**, *7*, 1900380.

[12] H. Zeng, M. Lahikainen, L. Liu, Z. Ahmed, O. M. Wani, M. Wang, H. Yang, A. Priimagi, *Nat. Commun.* **2019**, *10*, 5057.

[13] Y. Zhang, Z. Wang, Y. Yang, Q. Chen, X. Qian, Y. Wu, H. Liang, Y. Xu, Y. Wei, Y. Ji, *Sci. Adv.* **2020**, *6*, eaay8606.

[14] H. Zeng, O. M. Wani, P. Wasylczyk, R. Kaczmarek, A. Priimagi, *Adv. Mater.* **2017**, *29*, 1701814.

[15] H. Zeng, O. M. Wani, P. Wasylczyk, A. Priimagi, *Macromol. Rapid Commun.* **2018**, *39*, 1700224.

[16] O. M. Wani, H. Zeng, A. Priimagi, *Nat. Commun.* **2017**, *8*, 15546.

[17] J. A. H. P. Sol, A. R. Peeketi, N. Vyas, A. P. H. J. Schenning, R. K. Annabattula, M. G. Debije, *Chem. Commun.* **2019**, *55*, 1726-1729.

[18] S.-U. Kim, Y.-J. Lee, J. Liu, D. S. Kim, H. Wang, S. Yang, *Nat. Mater.* **2022**, *21*, 41-46.

[19] H. Tian, H. Liu, J. Shao, S. Li, X. Li, X. Chen, *Soft Matter* **2020**, *16*, 5599-5608.

[20] O. M. Wani, R. Verpaalen, H. Zeng, A. Priimagi, A. P. H. J. Schenning, *Adv. Mater.* **2019**, *31*, 1805985.

[21] H. Finkelmann, E. Nishikawa, G. G. Pereira, M. Warner, *Phys. Rev. Lett.* **2001**, *87*, 015501.

[22] T. Kato, Y. Hirai, S. Nakaso, M. Moriyama, *Chem. Soc. Rev.* **2007**, *36*, 1857-1867.

[23] L. T. de Haan, C. Sánchez-Somolinos, C. M. W. Bastiaansen, A. P. H. J.

Schenning, D. J. Broer, *Angew. Chem. Int. Ed.* **2012**, *51*, 12469–12472; *Angew. Chem.* **2012**, *124*, 12637–12640.

[24] B. Zuo, M. Wang, B.-P. Lin, H. Yang, *Nat. Commun.* **2019**, *10*, 4539.

[25] M. P. da Cunha, S. Ambergen, M. G. Debije, E. F. G. A. Homburg, J. M. J. den Toonder, A. P. H. J. Schenning, *Adv. Sci.* **2020**, *7*, 1902842.

[26] Z. Li, X. Zhang, S. Wang, Y. Yang, B. Qin, K. Wang, T. Xie, Y. Wei, Y. Ji, *Chem. Sci.* **2016**, *7*, 4741-4747.

[27] Y. Yang, F. Ma, Z. Li, J. Qiao, Y. Wei, Y. Ji, *J. Mater. Chem. A* **2017**, *5*, 7285-7290.

[28] H. Kim, J. Gibson, J. Maeng, M. O. Saed, K. Pimentel, R. T. Rihani, J. J. Pancrazio, S. V. Georgakopoulos, T. H. Ware, *ACS Appl. Mater. Interfaces* **2019**, *11*, 19506-19513.

[29] Q. He, Z. Wang, Y. Wang, A. Minori, M. T. Tolley, S. Cai, *Sci. Adv.* **2019**, *5*, eaax5746.

[30] M. P. da Cunha, Y. Foelen, T. A. P. Engels, K. Papamichou, M. Hagenbeek, M. G. Debije, A. P. H. J. Schenning, *Adv. Optical Mater.* **2019**, *7*, 1801604.

[31] M. P. da Cunha, Y. Foelen, R. J. H. van Raak, J. N. Murphy, T. A. P. Engels, M. G. Debije, A. P. H. J. Schenning, *Adv. Optical Mater.* **2019**, *7*, 1801643.

[32] H. Zeng, H. Zhang, O. Ikkala, A. Priimagi, *Matter* **2020**, *2*, 194-206.

[33] Z.-C. Jiang, Y.-Y. Xiao, L. Yin, L. Han, Y. Zhao, *Angew. Chem. Int. Ed.* **2020**,

59, 4925-4931; *Angew. Chem.* **2020**, *132*, 4955-4961.

[34] M. Wang, X.-B. Hu, B. Zuo, S. Huang, X.-M. Chen, H. Yang, *Chem. Commun.* **2020**, *56*, 7597-7600.

[35] H. Zeng, O. M. Wani, P. Wasylczyk, R. Kaczmarek, A. Priimagi, *Adv. Mater.* **2017**, *29*, 1701814.

[36] L. Chen, M. Wang, L.-X. Guo, B.-P. Lin, H. Yang, *J. Mater. Chem. C* **2018**, *6*, 8251-8257.

[37] X. Zheng, S. Guan, C. Zhang, T. Qu, W. Wen, Y. Zhao, A. Chen, *Small* **2019**, 1900110.

[38] X. Qian, Q. Chen, Y. Yang, Y. Xu, Z. Li, Z. Wang, Y. Wu, Y. Wei, Y. Ji, *Adv. Mater.* **2018**, *30*, 1801103.

[39] Y. Yang, E. M. Terentjev, Y. Zhang, Q. Chen, Y. Zhao, Y. Wei, Y. Ji, *Angew. Chem. Int. Ed.* **2019**, *58*, 17474-17479; *Angew. Chem.* **2019**, *131*, 17635-17640.

[40] Y. Wu, Y. Yang, X. Qian, Q. Chen, Y. Wei, Y. Ji, *Angew. Chem. Int. Ed.* **2020**, *59*, 4778-4784; *Angew. Chem.* **2020**, *132*, 4808-4814.

[41] R. C. P. Verpaalen, M. P. da Cunha, T. A. P. Engels, M. G. Debije, A. P. H. J. Schenning, *Angew. Chem. Int. Ed.* **2020**, *59*, 4532-4536; *Angew. Chem.* **2020**, *132*, 4562-4566.

[42] C. L. van Oosten, C. W. M. Bastiaansen, D. J. Broer, *Nat. Mater* **2009**, *8*, 677-682.

[43] M. Lahikainen, H. Zeng, A. Priimagi, *Nat. Commun.* **2018**, *9*, 4148.

[44] T. F. Scott, A. D. Schneider, W. D. Cook, C. N. Bowman, *Science* **2005**, *308*, 1615-1617.

[45] M. K. McBride, M. Hendrikx, D. Liu, B. T. Worrell, D. J. Broer, C. N. Bowman, *Adv. Mater.* **2017**, *29*, 1606509.

[46] E. C. Davidson, A. Kotikian, S. Li, J. Aizenberg, J. A. Lewis, *Adv. Mater.* **2020**, *32*, 1905682.

[47] H. Kaczmarek, P. Galka, *Open Process Chem. J.* **2008**, *1*, 8-11.

[48] X. Lu, S. Guo, X. Tong, H. Xia, Y. Zhao, *Adv. Mater.* **2017**, *29*, 1606467.

[49] M. P. da Cunha, A. R. Peeketi, K. Mehta, D. J. Broer, R. K. Annabattula, A. P. H. J. Schenning, M. G. Debije, *Chem. Commun.* **2019**, *55*, 11029-11032.

[50] M. Wang, Z.-W. Cheng, B. Zuo, X.-M. Chen, S. Huang, H. Yang, *ACS Macro Lett.* **2020**, *9*, 860-865.

[51] X. Lu, H. Zhang, G. Fei, B. Yu, X. Tong, H. Xia, Y. Zhao, *Adv. Mater.* **2018**, *30*, 1706597.

[52] L. Zhu, Y. Cao, Y. Liu, Z. Yang, X. Chen, *Soft Matter* **2017**, *13*, 4441-4456.

[53] Y. Cao, Y. Liu, Y. Chen, L. Zhu, Y. Yan, X. Chen, *J. Mech. Phys. Solids* **2017**, *99*, 304-320.

[54] Z. Yang, L. Zhu, B. Li, S. Sun, Y. Chen, Y. Yan, Y. Liu, X. Chen, *Extreme Mech. Lett.* **2016**, *8*, 88-95.

[55] C. J. Kloxin, T. F. Scott, H. Y. Park, C. N. Bowman, *Adv. Mater.* **2011**, *23*, 1977-1981.

Table 2.1. Effect of RM257 and MBTA contents on bending actuation of the pc-LCN film.

Sample[a]	RM257 (mol%)[b]	MBTA (mol%)[c]	Actuation[d]
MBTA-0%	34.0	0	O
MBTA-10%	30.6	3.4	O
MBTA-20%	27.2	6.8	O
MBTA-30%	23.8	10.2	O
MBTA-40%	20.4	13.6	X
MBTA-50%	17.0	17.0	X
MBTA-60%	13.6	20.4	X
MBTA-70%	10.2	23.8	X
MBTA-80%	6.8	27.2	X
MBTA-90%	3.4	30.6	X
MBTA-100%	0	34.0	X

[a] Designated as MBTA-#, where # indicates the molar percentage (mol%) of MBTA with respect to the total crosslinker content in pc-LCN. [b] Molar percentage (mol%) of RM257 in pc-LCN. [c] Molar percentage (mol%) of MBTA in pc-LCN. [d] O: bending actuation observed; X: not observed.

Table 2.2. Summary of mechanical properties of pristine and assembled pc-LCN films with different dyes (DB14, DR1, DO13).

Sample	$E^{a)}$ (MPa)	$\sigma_u{}^{a)}$ (MPa)	$\varepsilon_b{}^{a)}$ (%)
pc-LCN-B[b]	2.41 ± 0.8	10.8 ± 2.5	34.0 ± 15
Assembled pc-LCN-B[c]	3.46 ± 1.5	8.36 ± 2.8	7.39 ± 3.1
pc-LCN-R[b]	0.50 ± 0.15	3.46 ± 0.7	55.8 ± 20
Assembled pc-LCN-R[c]	0.46 ± 0.2	3.81 ± 0.9	42.8 ± 20
pc-LCN-O[b]	2.70 ± 0.7	6.65 ± 0.8	24.7 ± 9.8
Assembled pc-LCN-O[c]	1.97 ± 0.2	6.66 ± 0.4	21.6 ± 2.6

[a] Determined from tensile testing at 25 °C and strain rate of 0.04 min^{-1}, where E, σ_u, and ε_b are the elastic modulus, ultimate tensile stress, and strain at break, respectively. [b] Pristine pc-LCN films with different dyes. [c] Films assembled under 365 nm UV irradiation (0.2 W cm^{-2}) for 30 s.
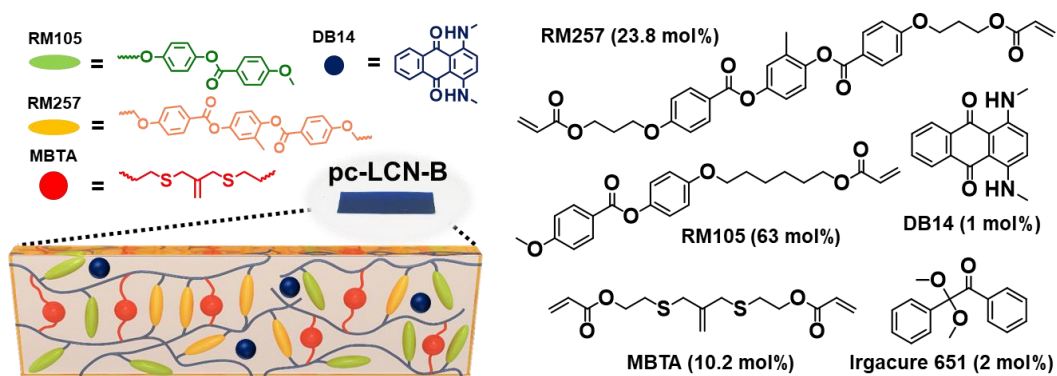
Figure 2.1. Schematic illustration of the dual-crosslinked pc-LCN and chemical structures of the components used in the pc-LCN-B.
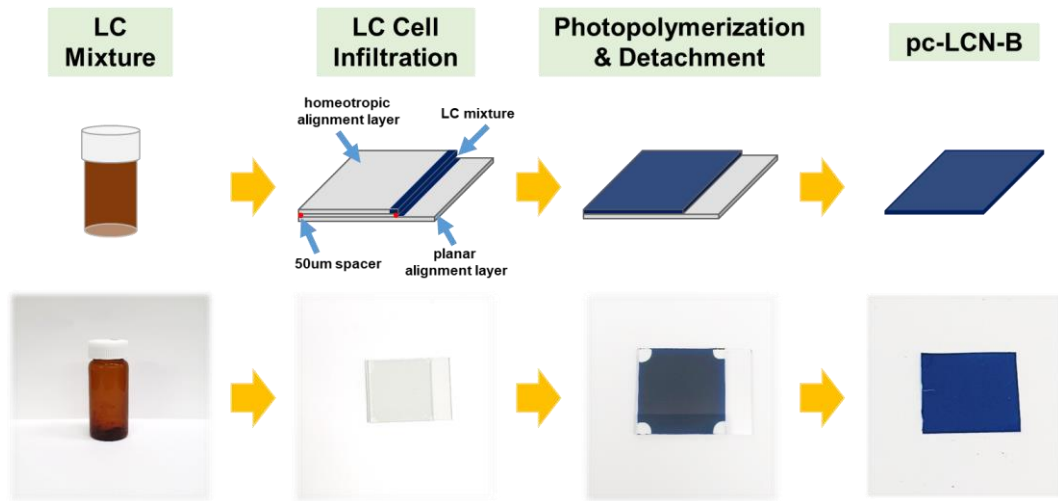
Figure 2.2. Schematic illustration and photographs showing fabrication process of pc-LCN-B.
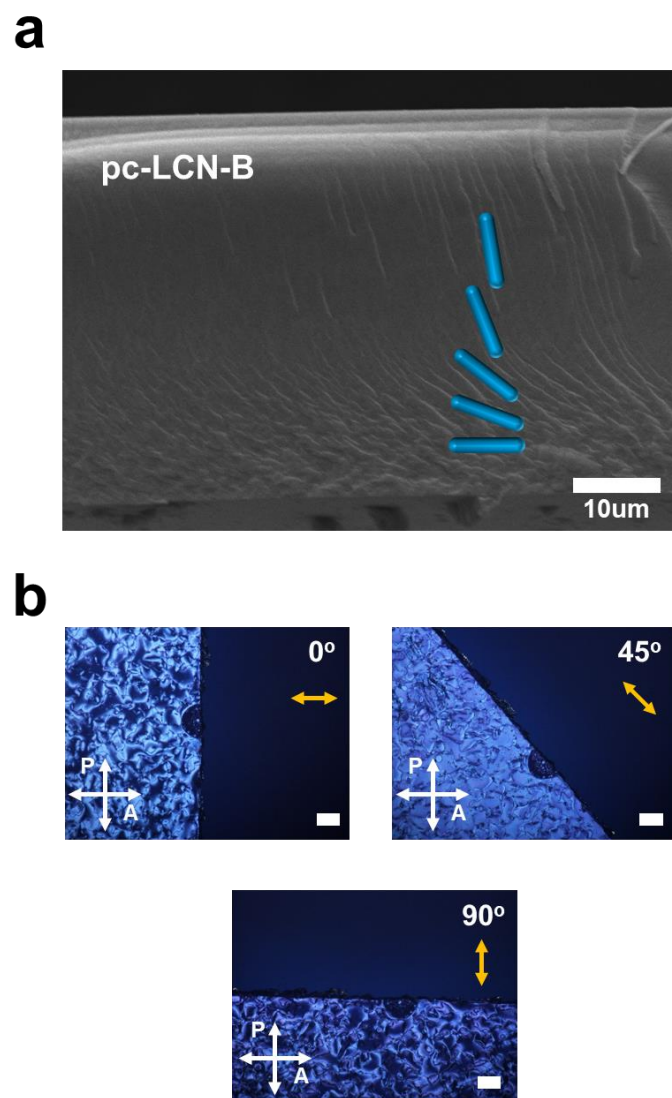
Figure 2.3. a) Cross-sectional SEM image and b) POM images of the splay-aligned pc-LCN-B film (scale bars: 10 μm).
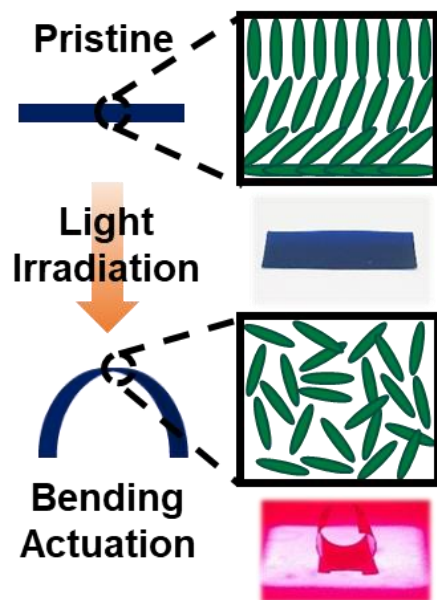
Figure 2.4. Visible light-driven actuation of the splay-aligned pc-LCN-B film doped with disperse blue 14 (DB14, 1 mol%).
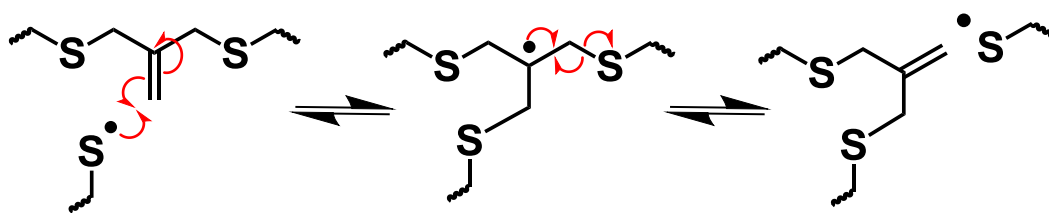
Figure 2.5. Mechanism of dynamic allyl sulfide bond exchange.
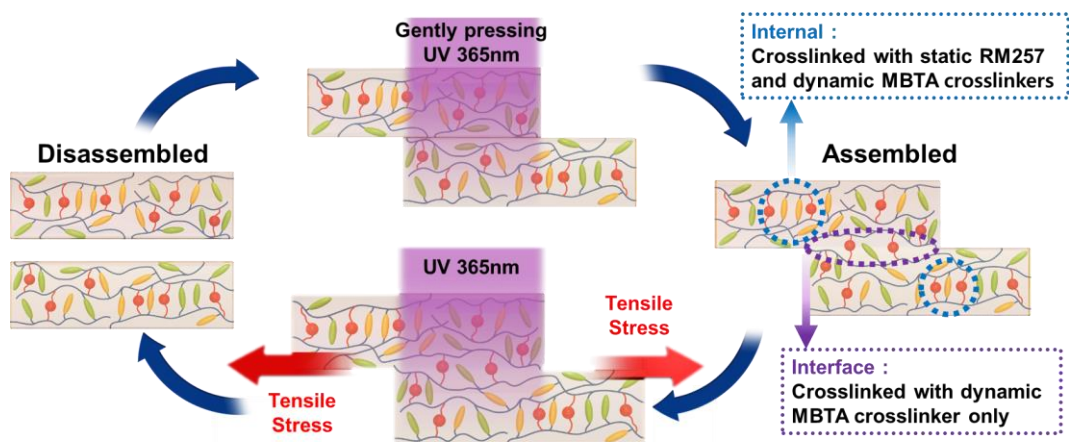
Figure 2.6. Mechanism for photo-controlled reversible assembly and disassembly of the pc-LCN film.
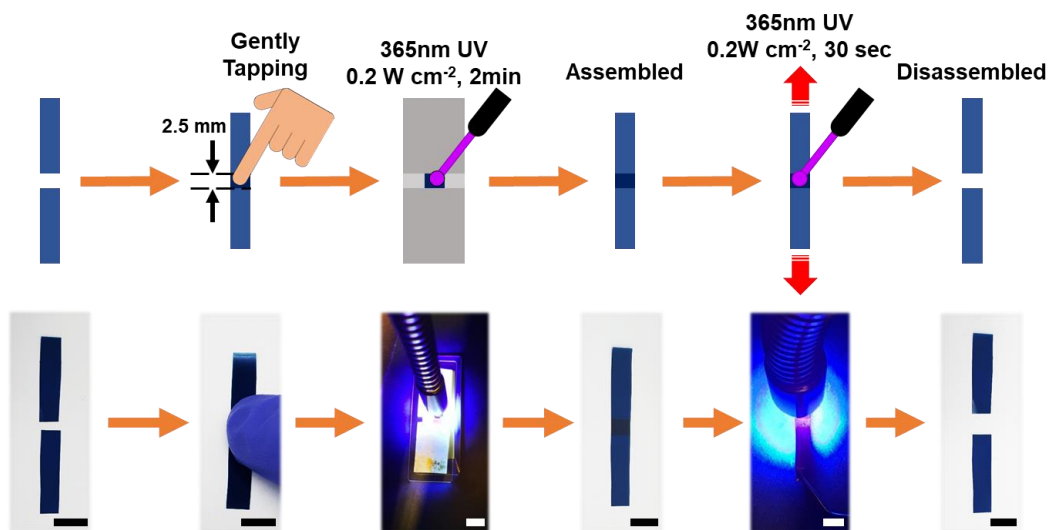
Figure 2.7. Schematic illustration and photographs of UV-controlled assembly-disassembly procedure for pc-LCN-B films (scale bars: 5 mm).
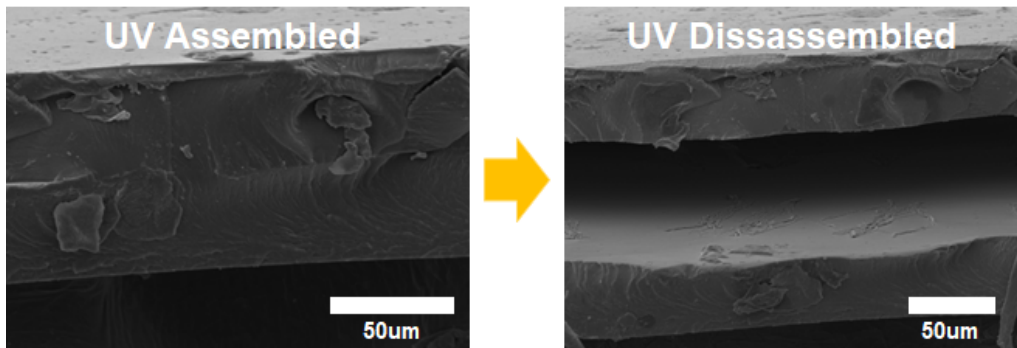
Figure 2.8. Cross-sectional SEM images of the assembled and disassembled pc-LCN-B film.
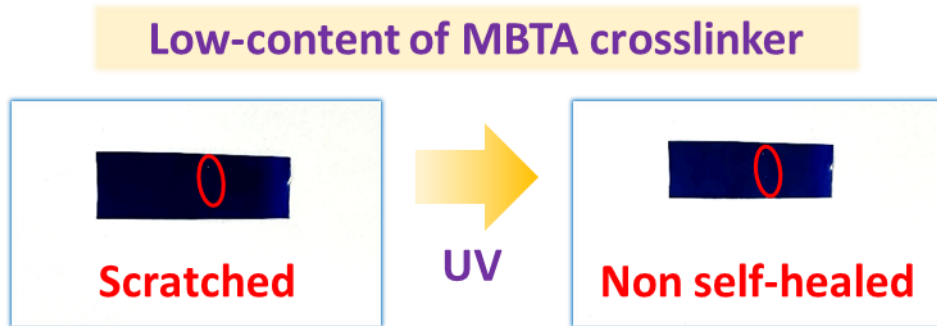
Figure 2.9. Self-healing properties of pc-LCN-B under UV irradiation.
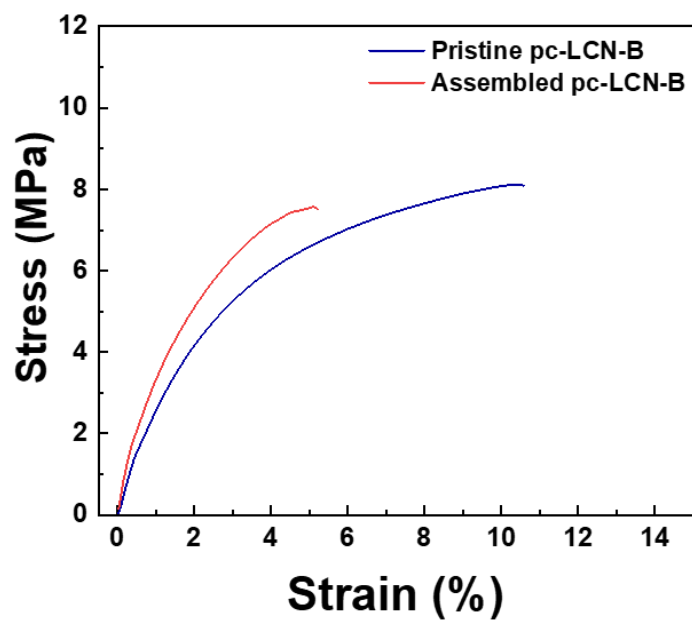
Figure 2.10. Representative stress-strain curves of pristine and assembled pc-LCN-B films.
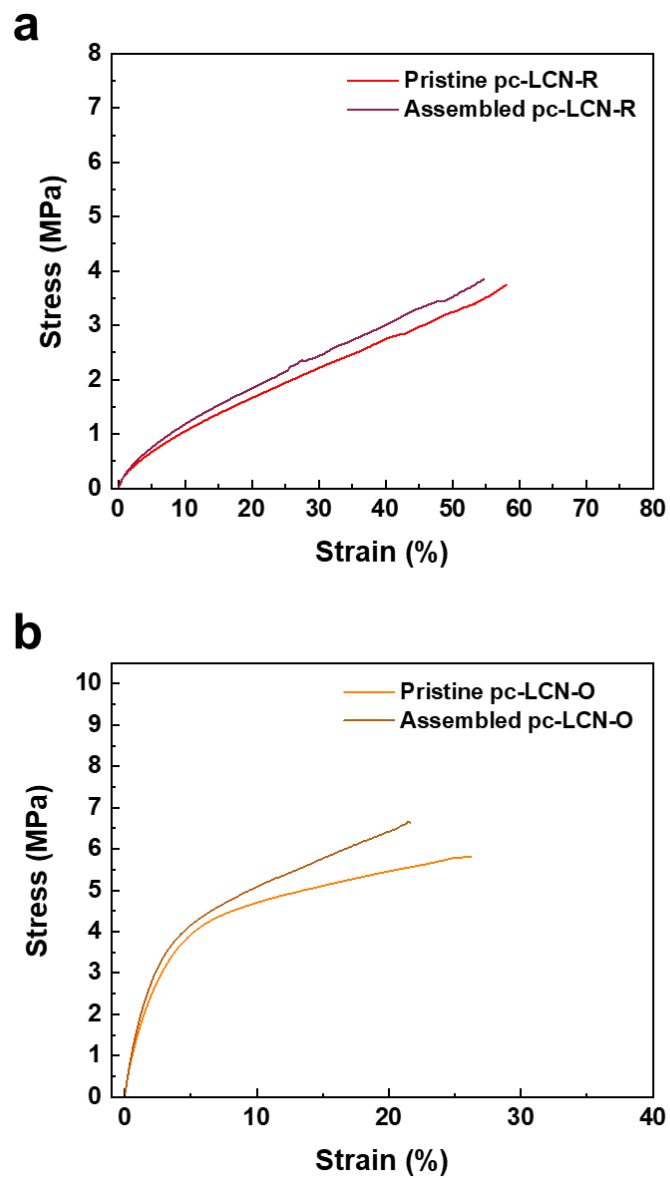
Figure 2.11. Representative stress-strain curves of pristine and assembled pc-LCN films with a) DR1 and b) DO13 dyes.
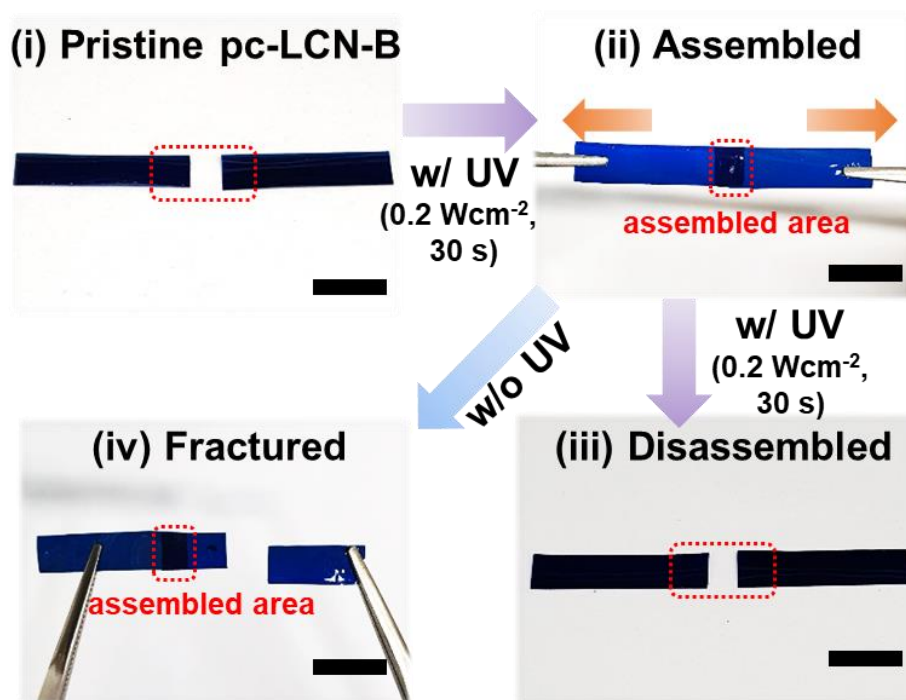
Figure 2.12. Photographs of (i) pristine, (ii) assembled, and (iii) disassembled films during the photo-controlled reversible assembly-disassembly process, and (iv) fractured film under a tensile load (scale bars: 5 mm).
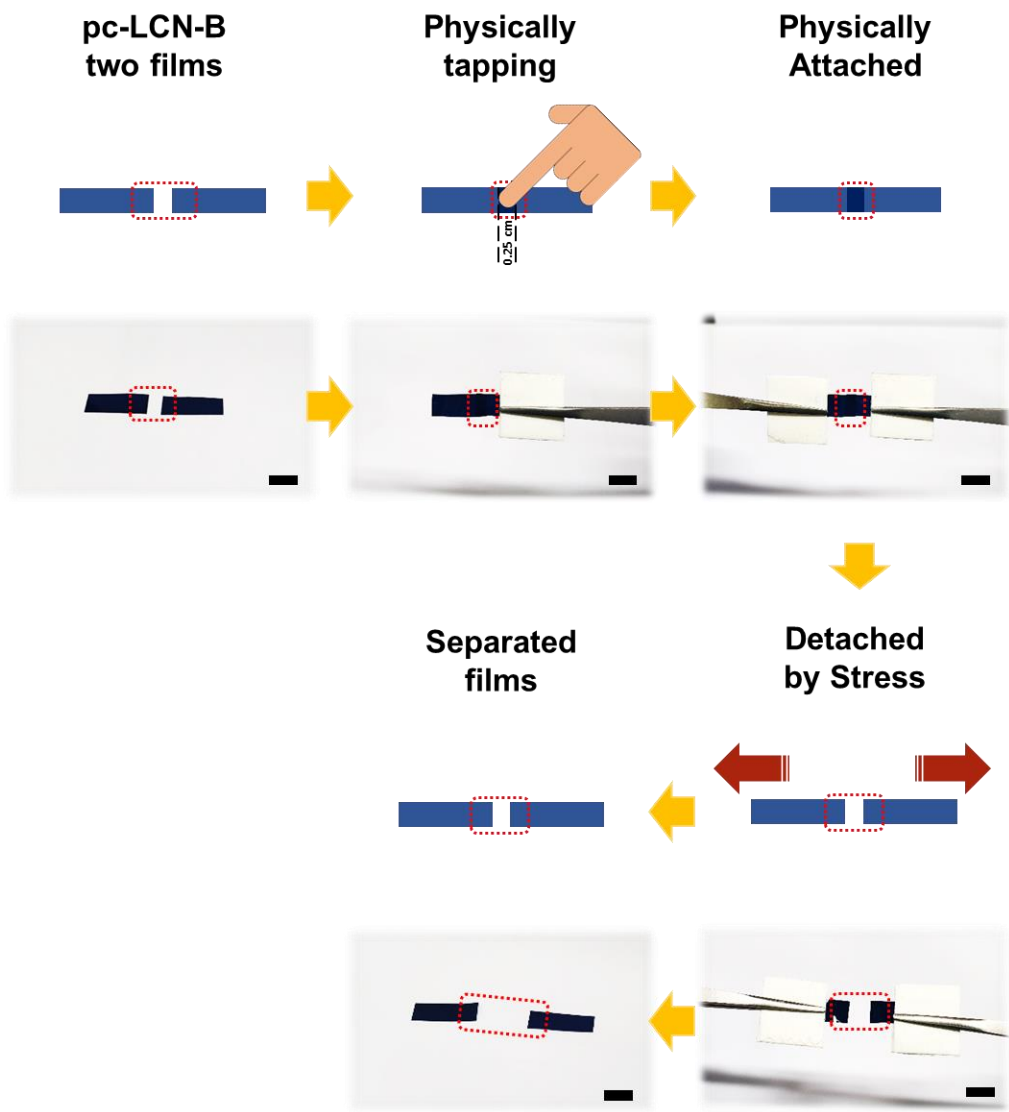
Figure 2.13. Schematic illustration and photographs of physically attached pc-LCN-B films without UV irradiation, showing detachment under tensile stress (scale bars: 5 mm).
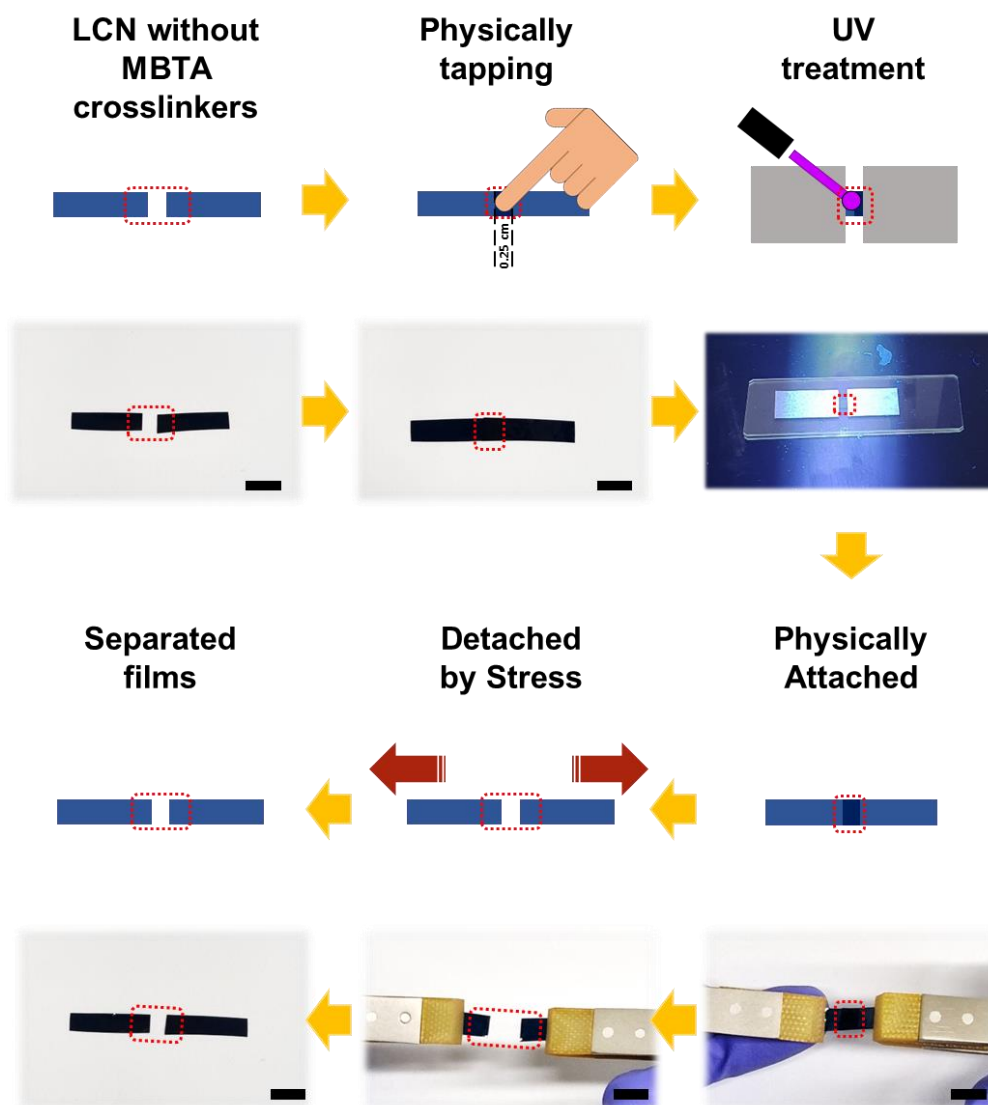
Figure 2.14. Schematic illustration and photographs of physically attached LCN-B films without any MBTA crosslinkers (i.e., with 100% RM257 crosslinkers) under UV irradiation (0.2 W cm^{-2}, 30 s), showing detachment under tensile stress (scale bars 5 mm).
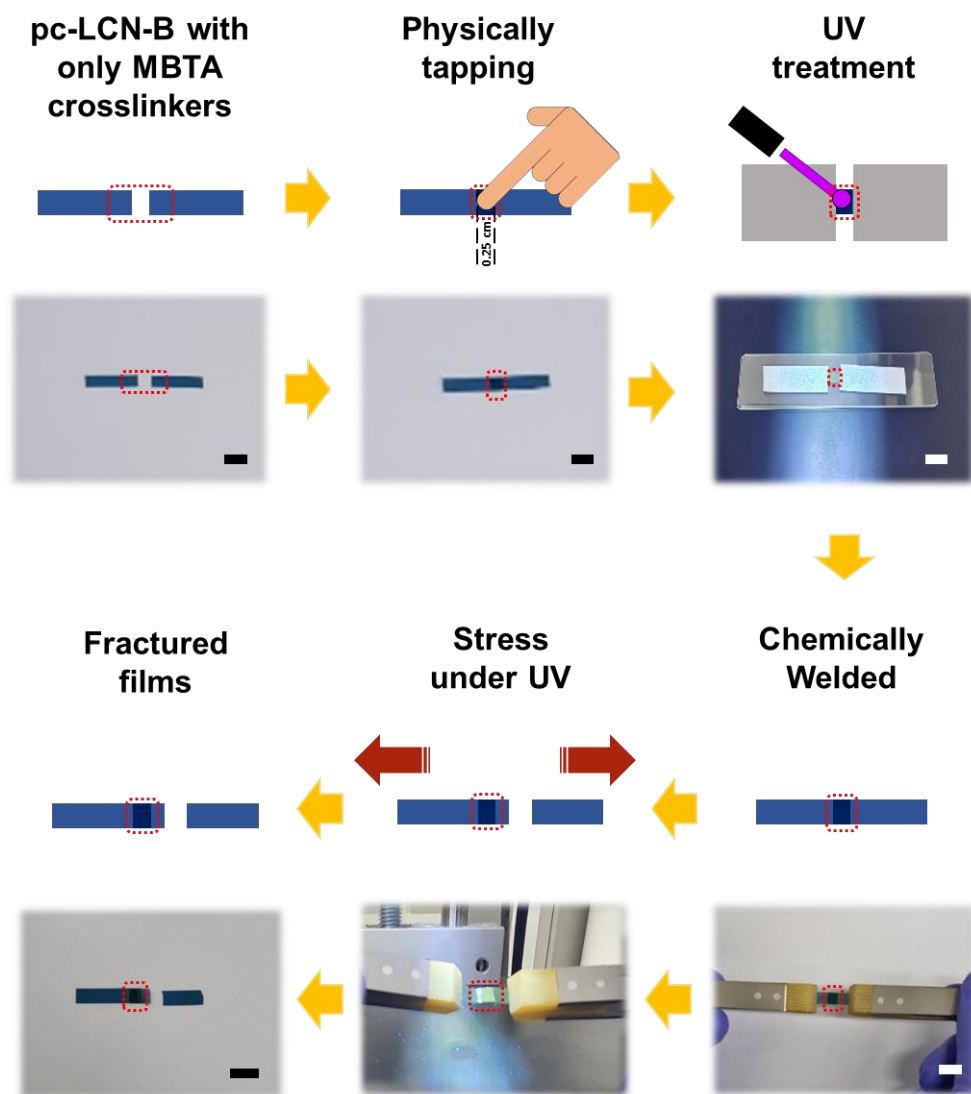
Figure 2.15. Schematic illustration and photographs of chemically welded pc-LCN-B films with only MBTA crosslinkers (i.e., with 0% RM257 crosslinkers) under UV irradiation. After the UV irradiation (0.2 W cm^{-2}, 30 s), the films were completely welded and could not be disassembled again (scale bars: 5 mm).
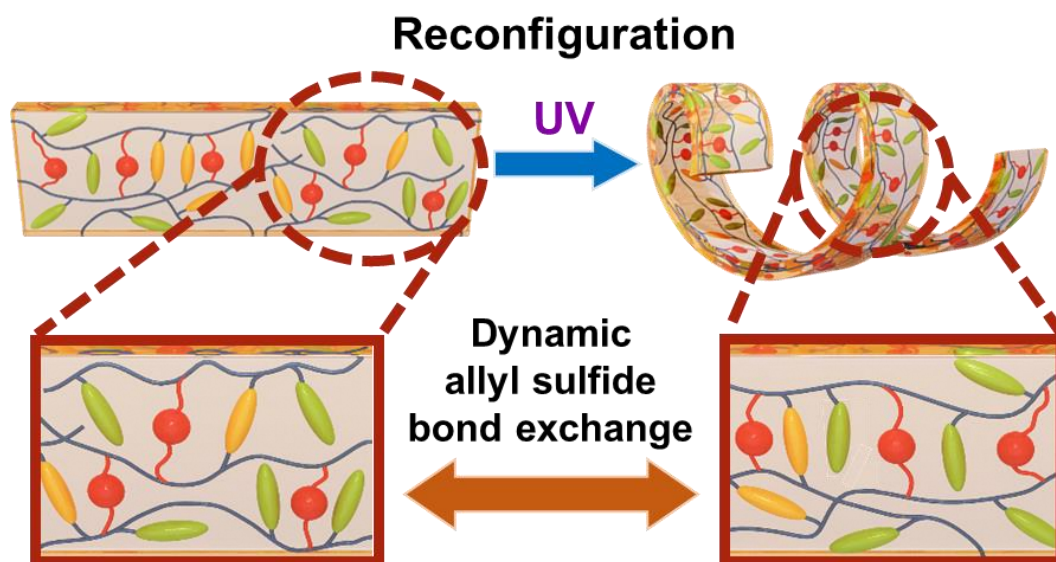
Figure 2.16. Mechanism for the plasticity-based shape reconfiguration of pc-LCN via dynamic allyl sulfide bond exchange under UV irradiation (0.2 W cm^{-2}, 40 s).
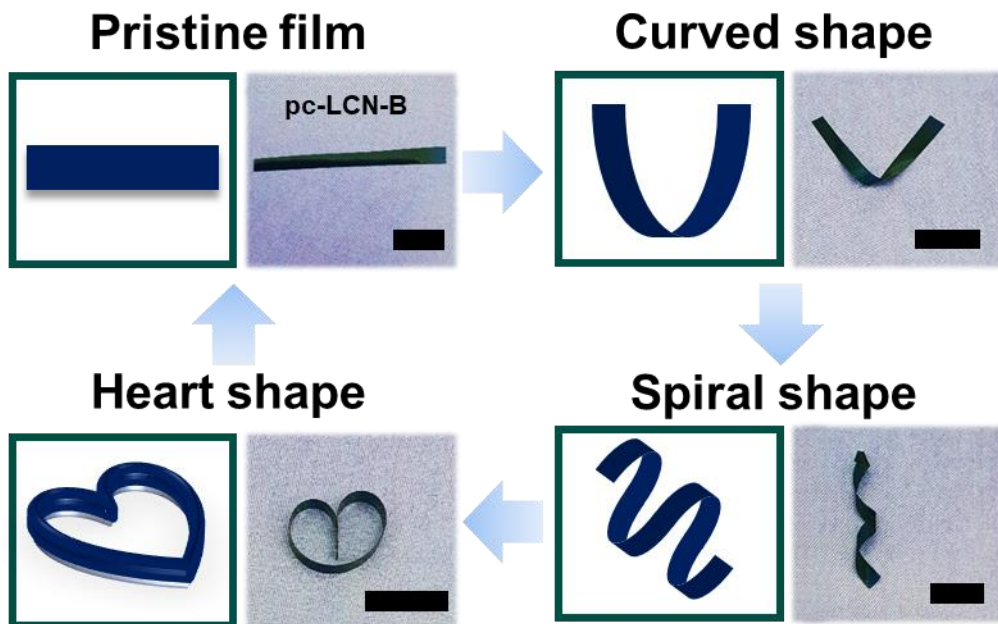
Figure 2.17. Consecutive shape reconfiguration of the pc-LCN-B film via cumulative photo-induced plasticity (scale bars: 5 mm).
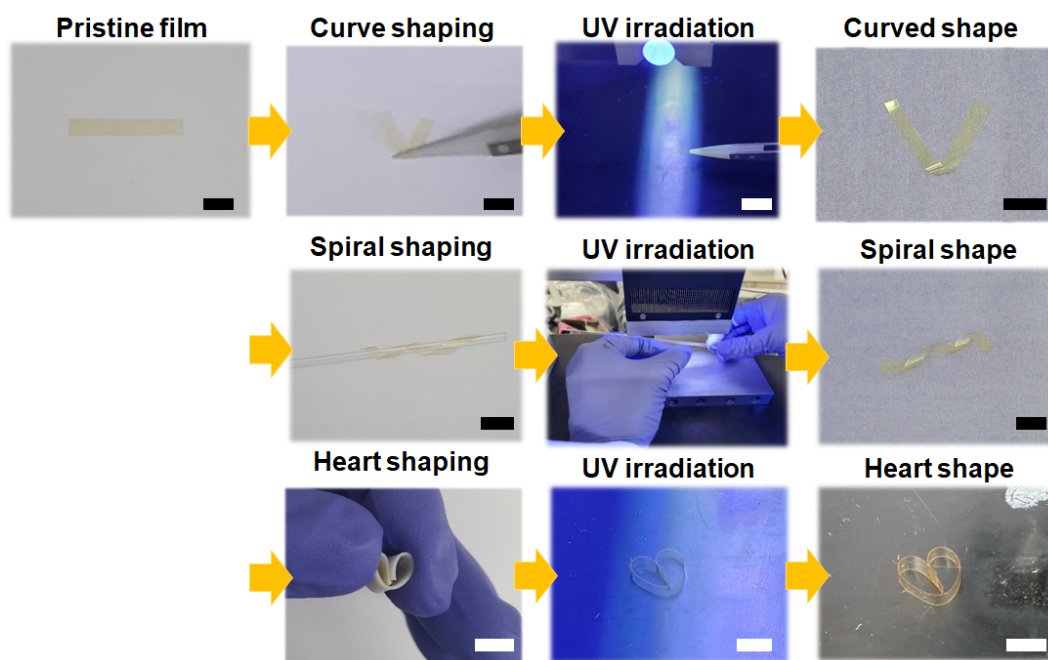
Figure 2.18. Photographs for consecutive photo-controlled shape reconfiguration processes of dye-free pc-LCN (scale bars: 5 mm).
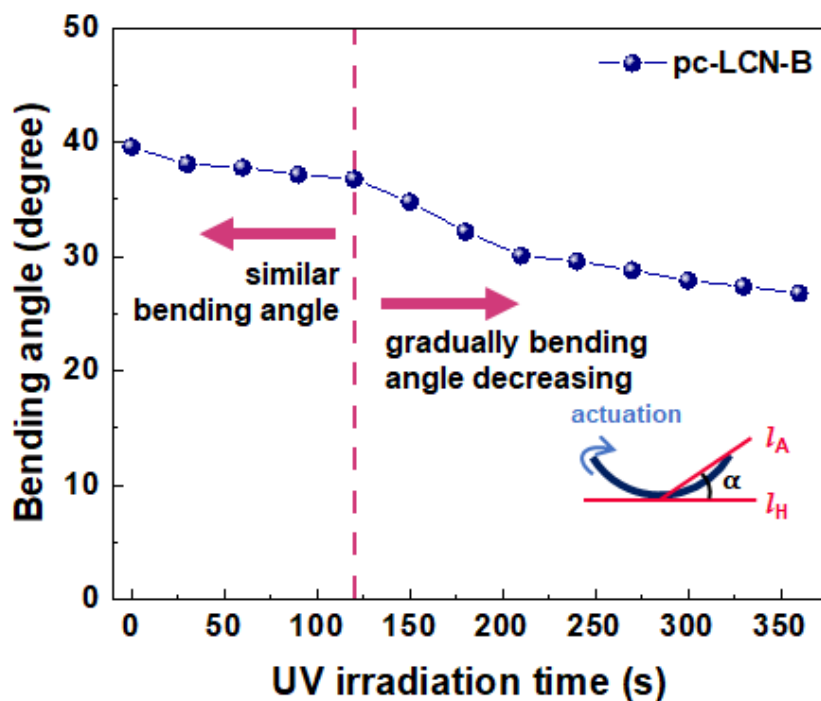
Figure 2.19. Bending angle variation of the pc-LCN-B film after UV irradiation ($0.2\ \mathrm{W\ cm^{-2}}$). Bending angles were measured at 40 s under 660 nm light irradiation. The bending angle is α between the line l_A and l_H, where l_A is the tangent line from the middle to right endpoint of the arc, and l_H is the horizontal baseline.
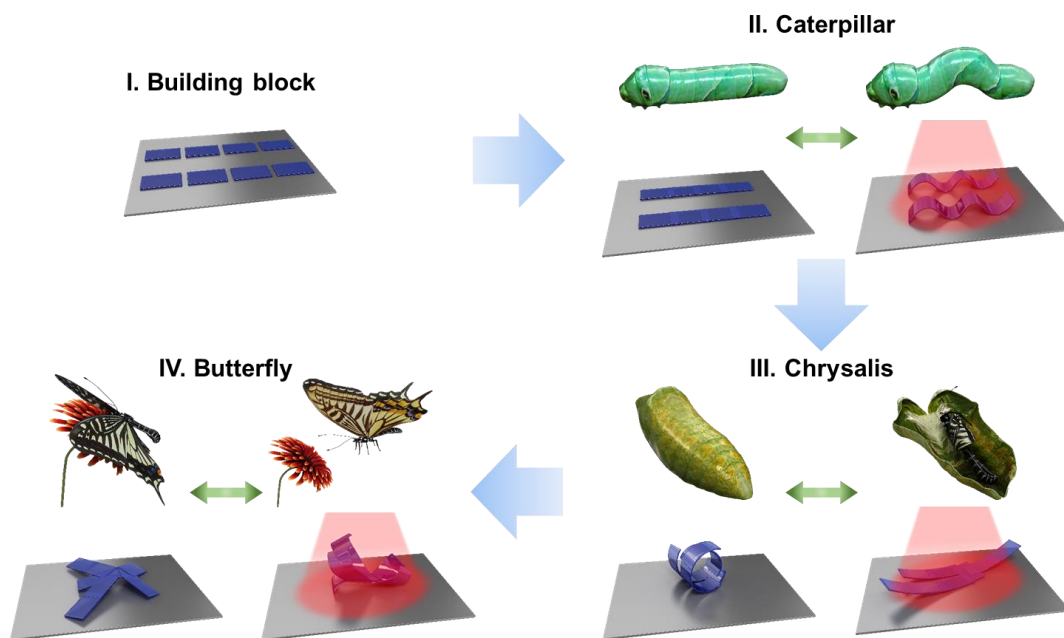
Figure 2.20. Schematic illustration for the transformation process from pc-LCN-B building blocks to caterpillar-, chrysalis-, and butterfly-mimicking structures.
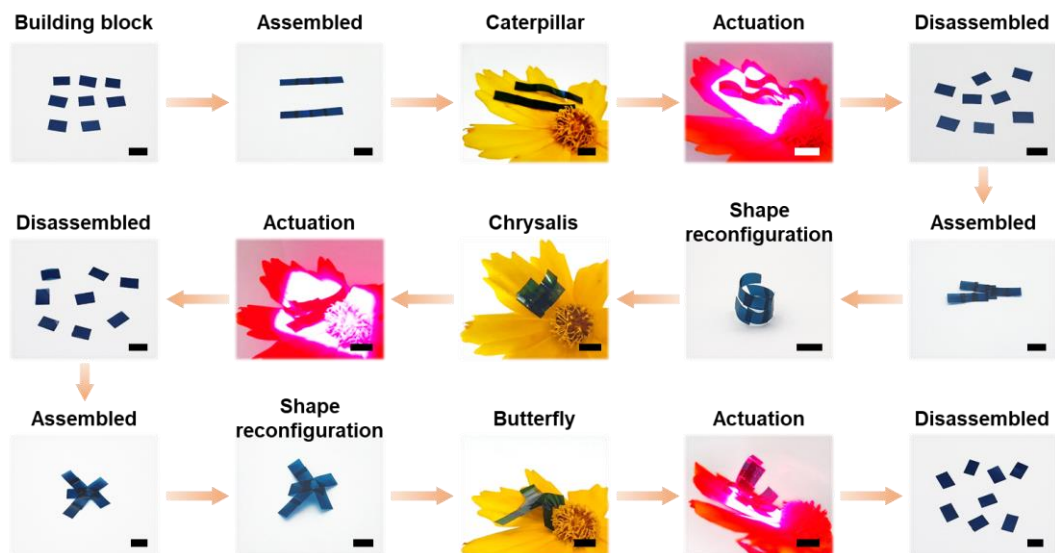
Figure 2.21. Photographs of consecutive building block assembly, shape reconfiguration, photo-responsive actuation, and disassembly of the monolithic 3D architectures (scale bars: 5 mm).
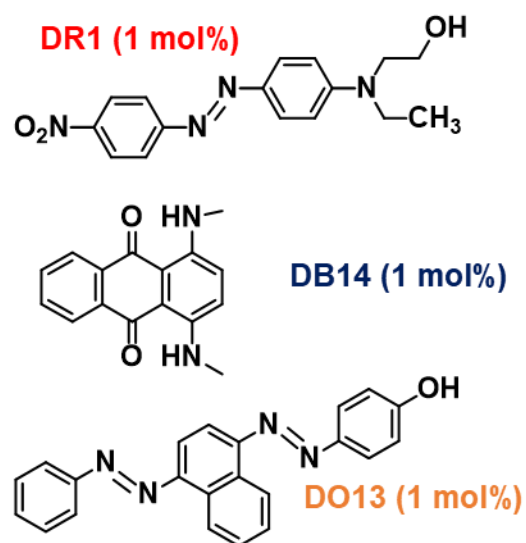
Figure 2.22. Chemical structures of three visible-light-absorbing dyes with almost non-interfered absorptions; Disperse Red 1 (DR1, 532 nm), Disperse Blue 14 (DB14, 660 nm), and Disperse Orange 13 (DO13, 405 nm).
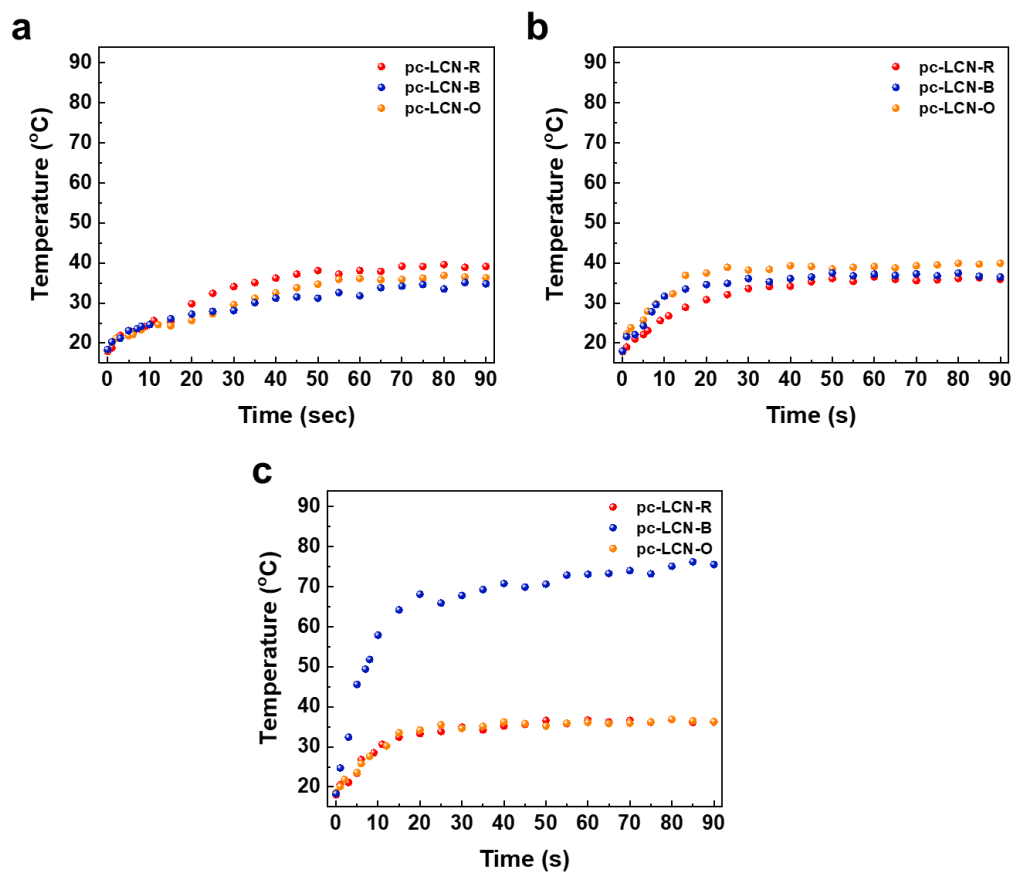
Figure 2.23. Profiles of temperature vs. time of different dye-doped pc-LCN films under a) 532 nm, b) 405 nm, and c) 660 nm light irradiation.
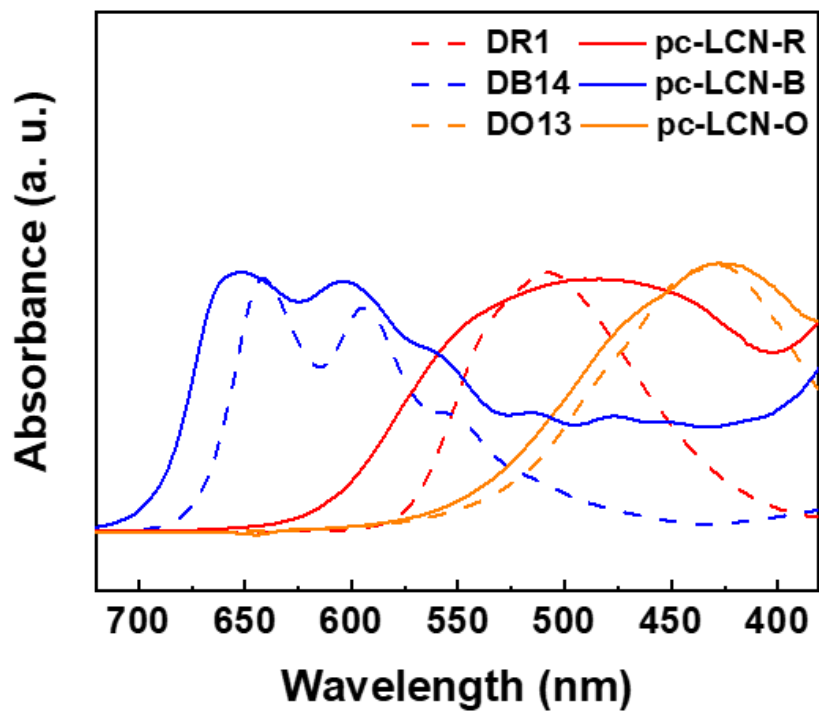
Figure 2.24. UV-Vis absorption spectra of DR1, DB14, and DO13, and the corresponding pc-LCN-R, pc-LCN-B, and pc-LCN-O films (dye content = 1 mol%), respectively.
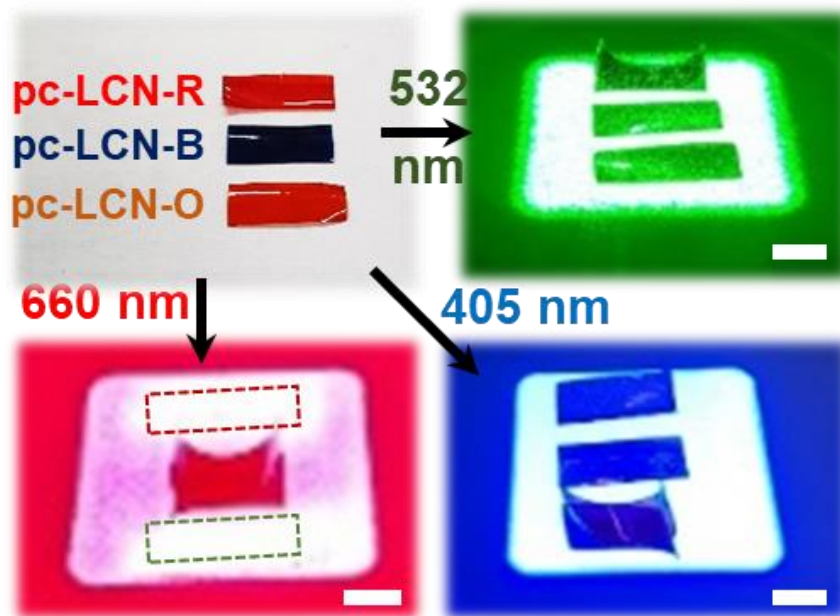
Figure 2.25. Photographs of independent bending actuation of the different dye-doped pc-LCN films under 532 nm, 660 nm, and 405 nm light irradiation (scale bars: 5 mm).
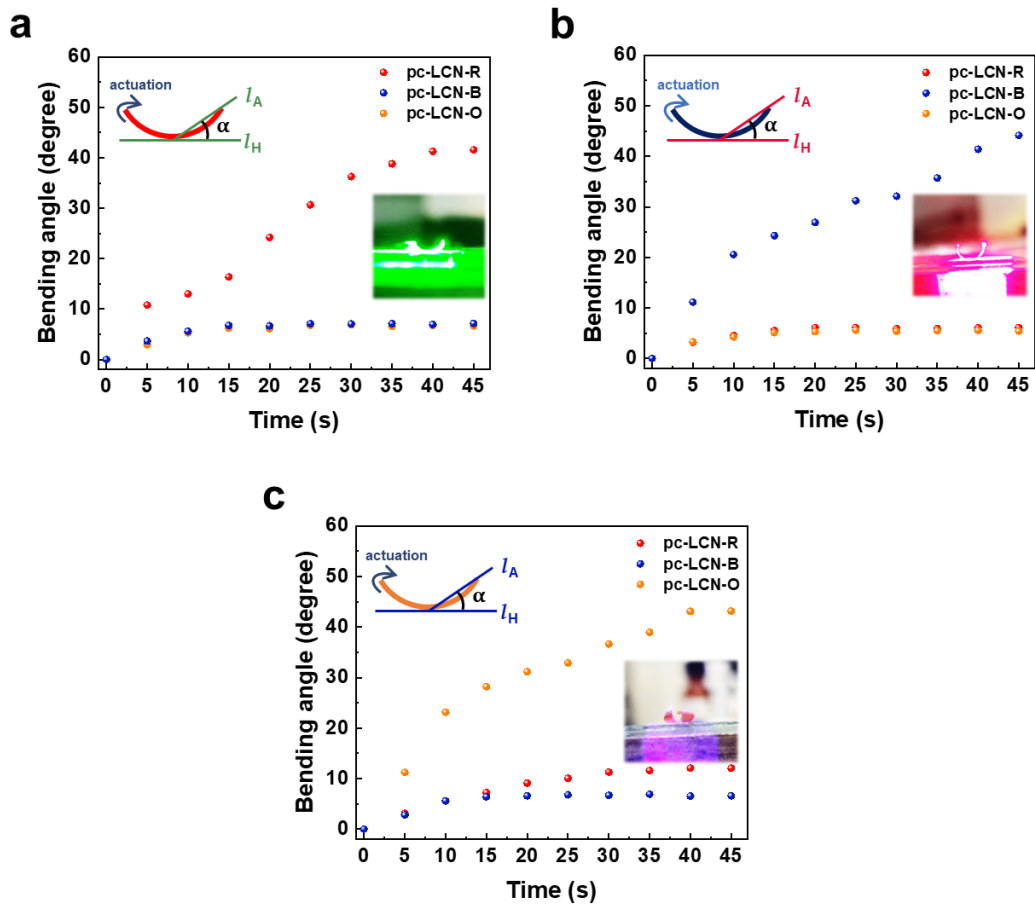
Figure 2.26. Profiles of the induced bending angle degrees of different dye-doped pc-LCN films against irradiation time under d) 532 nm, e) 660 nm, and f) 405 nm light irradiation (50 mW cm^{-2}).
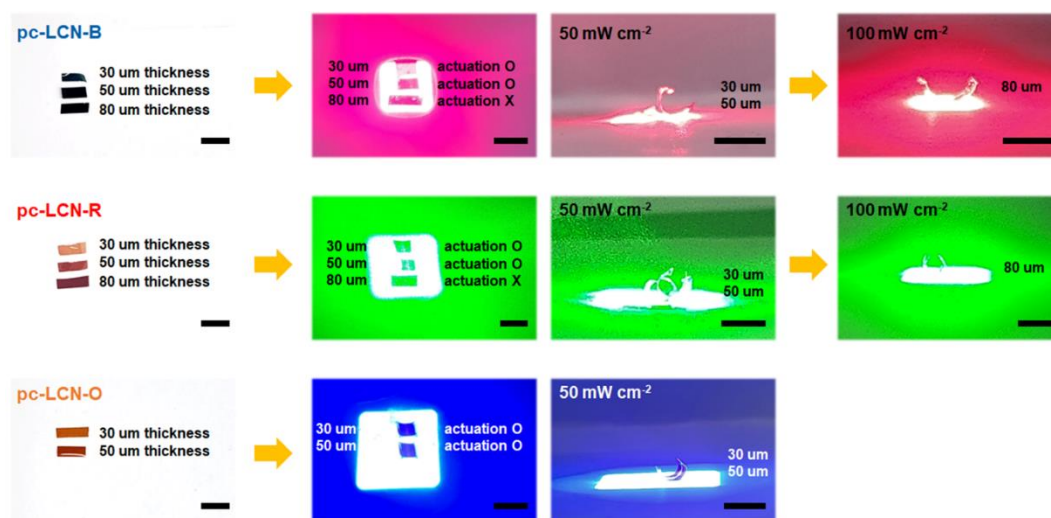
Figure 2.27. The actuation behavior of pc-LCN according to different thicknesses. All pc-LCNs with thicknesses of 30, 50, and 80 µm were demonstrated (scale bars: 10 mm).

a

Soft rolling robot   Soft tripod robot   Soft gripper

b

(III) Storage

"Unloading"   "Walking"   (IV) Obstacle

"Switching
Direction"

"Walking"

(II) Transformation   (I) Start /
Finish

"Gripping,
Loading"

"Rolling"
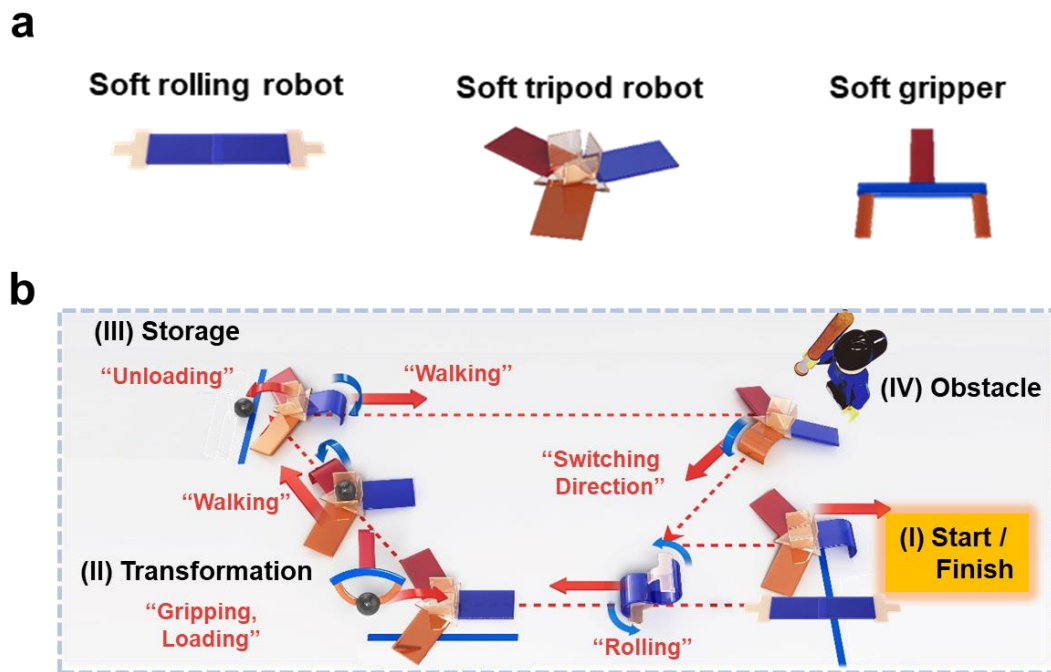
Figure 2.28. Demonstration of monolithically assembled 3D soft robots, capable of photo-controlled reversible assembly/disassembly- and shape reconfiguration-based transformation and selective visible light-driven locomotion. a) Schematic illustration of the soft rolling robot, soft tripod robot, and soft gripper. b) Overall schematic description of various locomotion and transformation of the 3D soft robots on track.
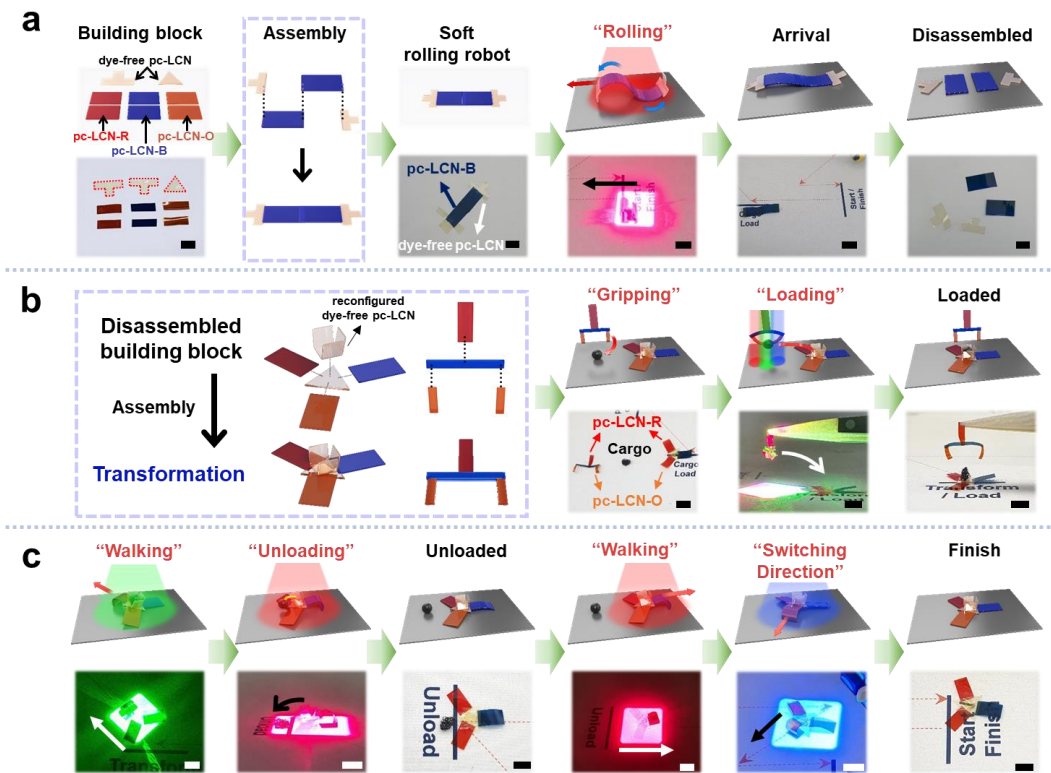
Figure 2.29. Schematic illustrations and corresponding photographs are shown at the top and bottom of the figure, respectively (scale bars: 5 mm). a) Processes of manufacturing soft rolling robot, rolling locomotion from position (I) to position (II), and disassembly. b) Transformation from soft rolling robot to soft tripod robot, assembly of soft gripper, and black cargo loading process using the soft gripper to the soft tripod robot. c) Walking locomotion of the cargo-loaded soft tripod robot from position (II) to position (III), unloading the cargo, and returning to position (I) through switching direction at position (IV).
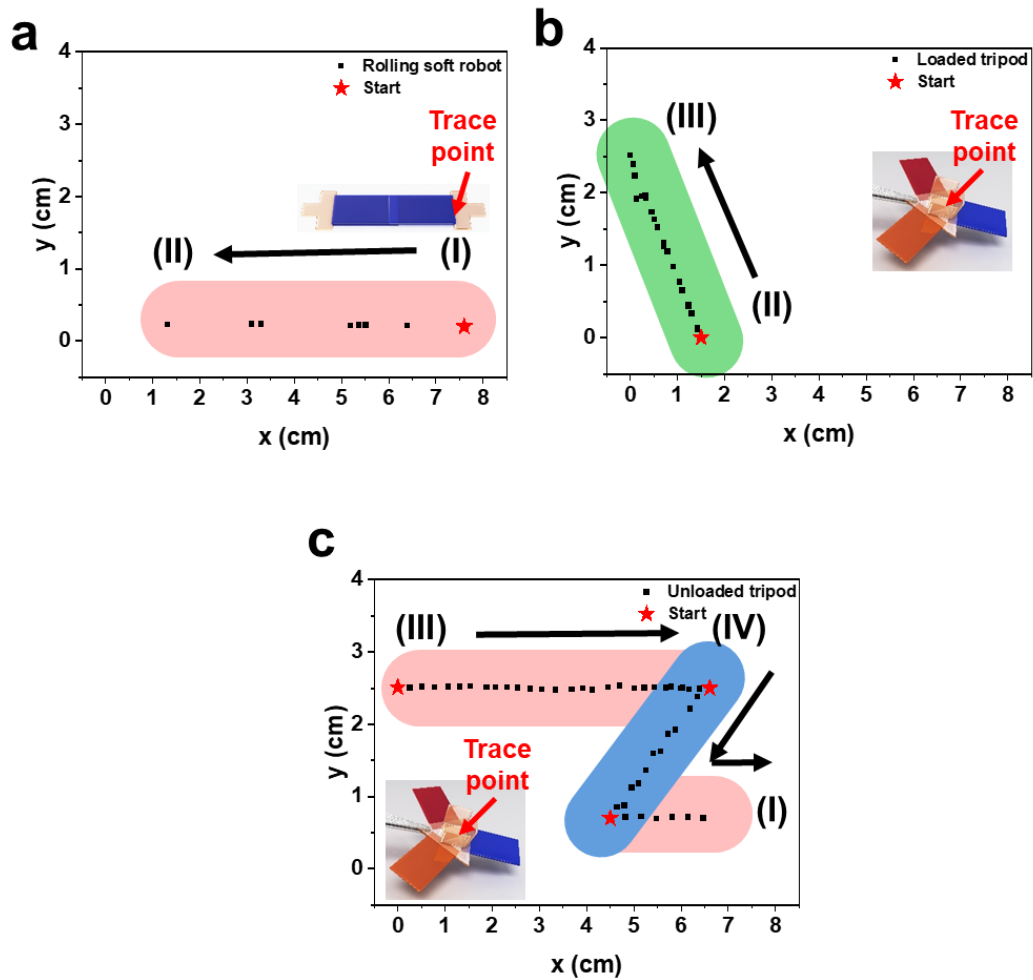
Figure 2.30. Trace coordinates of the a) soft rolling robot locomotion from position (I) to position (II), b) soft tripod robot locomotion from position (II) to position (III), and c) soft tripod robot locomotion from position (III) to position (I), via position (IV). The positions of the soft robots were traced every 5 s.
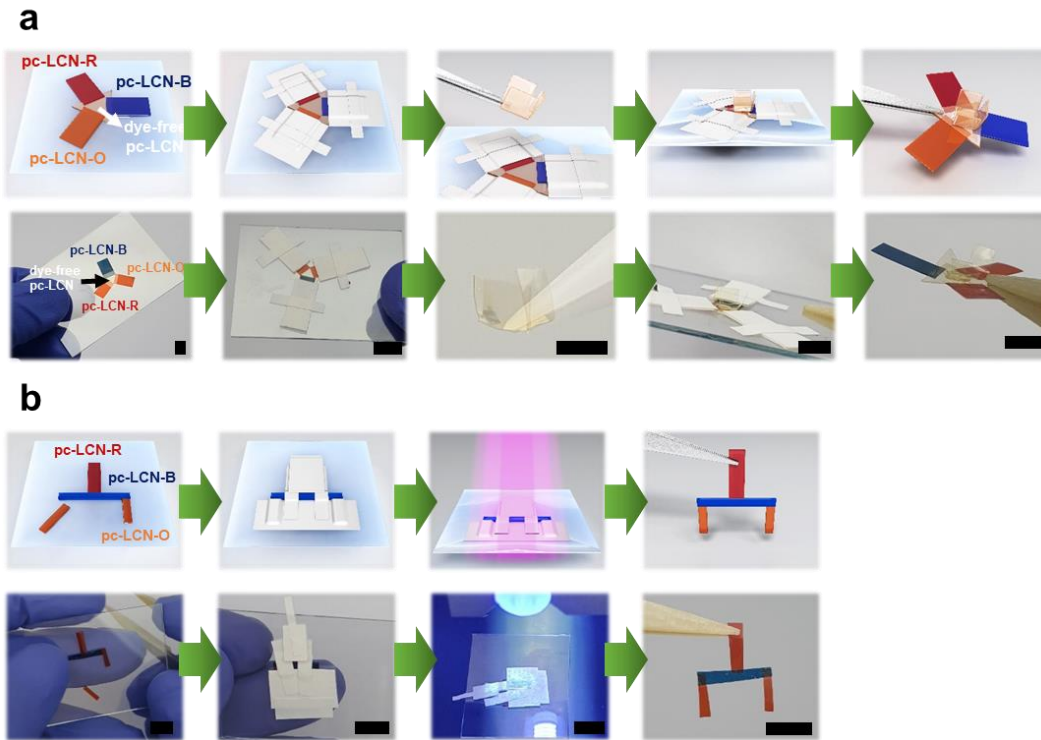
Figure 2.31. Schematic illustration and photographs of the detailed manufacturing procedures of a) soft tripod robot and b) soft gripper (scale bars: 5 mm).

Chapter 3

Multifunctional Poly(thiourethane) Vitrimer

with Variable Stiffness and Lego-like

Assembly/Disassembly Properties

for 3D Transformable Soft Robot

3.1. Introduction

Dynamic covalent polymer networks with excellent mechanical, rheological, and thermal properties have facilitated reprocessing and recycling, which was previously challenging. Since Leibler *et al.* introduced the associative dynamic ester exchange reaction into epoxy-based crosslinked polymers in 2011 [1], vitrimer or vitrimer-like materials based on dynamic covalent bond exchanges have received significant attention [2-4]. With malleability and rheological behavior in the solid state, vitrimers can be used as multifunctional materials with the incorporation of fillers [5-8]. Multifunctional vitrimers showed the great potential of various fields, such as shape morphing devices [9-13], soft robotics [14-16], carbon fiber reinforced plastic [17-19], and energy storage systems [20-23]. Although it was possible to induce macroscopic actuation or enhance the mechanical properties through fillers, manipulating the various properties in neat vitrimers without changing the composition of monomers or adding fillers is still challenging. Therefore, many pioneering studies on vitrimers that impart various properties according to the multifunctionalized network are required.

In the past decade, variable stiffness materials have received considerable attention in controlling rigidity depending on the environment effectively [24,25]. When variable stiffness properties are applied to smart materials, low stiffness in a

conformable state provides adaptability to the environment, while high stiffness in a rigid state allows for bearing heavy loads [26]. Such variable stiffness characteristics can be applied to damping structures [27,28], shape-morphing structures [29,30], soft grippers [31-33], compatible actuators for rigid robots [34,35], and even medical devices [36-38]. Thermally responsive polymers can achieve variable stiffness properties by utilizing the significant mechanical property changes based on the glass transition and melting transition of the polymer. Recently, research on the composite formation of shape memory thermoset polymers for 4D printing applications has been reported to achieve variable stiffness [39,40]. In addition, researches on physical crosslinking via metal-ligand formation to impart variable stiffness to thermoplastic or thermoset polymers have been reported [41,42]. However, designing vitrimers as variable stiffness materials based on elastic modulus changes through glass transition or using coordination bonding is very challenging due to their high crosslinking density and the requirement for specific metallic catalysts. To handle the challenges above, Chen *et al.* reported a modulated stiffness of polyurethane vitrimer composite based on the formation of the crystalline structure [43]. However, researches for applying vitrimers as smart materials based on high mechanical properties and drastic stiffness changes yet still need to be achieved.

Vitrimers can be implemented from a 2D film state to a 3D structure through a welding process [44]. However, once the welding has been conducted, the material should be reprocessed for recycling and reshaping to change the architectures. In order to utilize the vitrimers as smart materials, the assembly and disassembly of two different 2D vitrimer films should be controllable as required. The study of the realization of a 3D structure based on interfacial assembly and disassembly of liquid crystalline networks through dynamic covalent bond exchange between allyl sulfides has been reported [16]. However, the challenge of limited repetition of assembly and disassembly still exists due to the consumption of the photoinitiator. Although studies using the adhesive properties of polymer materials have been reported [45,46], adding adhesive components and the complex condition of designing the material to suit the operating condition is required. Therefore, advanced vitrimers with permanent assembly and disassembly functionality are necessary for their application in smart devices and soft robotics without additional adhesive components.

Herein, we report the multifunctional poly(thiourethane) (MFTU) vitrimer without adding fillers containing excess thiol, which exhibits tunable stiffness and allows for the assembly and disassembly of 2D films into 3D structures. As shown in Figure 3.1, we proposed an MFTU vitrimer with a slight excess thiol ratio using a zinc diethyldithiocarbamate ($Zn(DTC)_2$) catalyst, which promotes multifunctional

properties. First, MFTU, which contains an excess of thiol at the end groups, exhibits vitrimer characteristics via associative-type dynamic covalent bond exchange (Figure 3.2a). The low-toxic $Zn(DTC)_2$ can be used as a catalyst for the bulk polymerization of urethane and thiourethane based crosslinked polymers instead of the highly toxic dibutyltin dilaurate (DBTDL) [47]. The sulfurphilic diethylthiocarbamate group in $Zn(DTC)_2$ facilitates the S_N2-type dynamic thiourethane bond exchange of thiol-terminated MFTU and enables facile reprocessing and recycling. In addition, since the thiourethane bond shows a shorter bond length and lower dissociation energy than the urethane bond, the more facile dynamic covalent bond exchange is enabled (Figure 3.3) [48]. Second, MFTU exhibits variable stiffness characteristics due to the semi-crystalline structure in the network (Figure 3.2b). Through excess thiol ratio and hexamethylene diisocyanate alkyl chains (HDI), crosslinked MFTU can form a semi-crystalline structure due to the increased chain lengths of the flexible linear chains in MFTU network [49]. With excess 10 mol % of thiol, we synthesized the MFTU by tuning the 2,2 - (Ethylenedioxy)diethanethiol (DODT) chain extender and the pentaerythritol tetrakis(3-mercaptopropionate) (PETMP) crosslinker at an appropriate ratio of 17 : 3 mol %. The MFTU showed a very low T_g of 2.4 $^\circ$C, enabling chain mobility at room temperature (Figure 3.4). We realized rigid or pliable states of MFTU through stiffness modulation according to melting temperature (T_m) of a linear alkyl chain-

9 3

based semi-crystalline structure. Third, MFTU films are capable of interfacial Lego-like assembly/disassembly through dissociation-reformation of hydrogen and Zn coordination bonds (Figure 3.2c). MFTU contains thiol, oligo ether, and thiourethane moieties within the network, allowing for the formation of abundant hydrogen bond (H-bond). In addition, $Zn(DTC)_2$ induces the formation of Zn coordination bonds with the thiol end groups of MFTU, leading to thiol ligands. Due to the weak coordination bond strength of zinc in the solid state, Zn coordination bond is dissociated above the temperature of 60 °C [50], while H-bond also broken. Therefore, by applying heat treatment to the interface between the two MFTU films, the interfacial assembly is induced, resulting in the fabrication of 3D structures. Additionally, disassembly of the MFTU films is enabled by subjecting the assembled 3D structures to heat treatment again. Based on the vitrimer property, variable stiffness, and Lego-like assembly/disassembly, we fabricated a transformable robot by reversible assembly/disassembly and welding of MFTU building blocks, and demonstrated magnet actuation on the stiffness state.

3.2. Results and Discussion

3.2.1. Vitrimer Properties of MFTU

We confirmed the vitrimer properties of bulk polymerized MFTU under $Zn(DTC)_2$ catalysis according to the mole percentage of excess thiol. A series of MFTUs (MFTU-#, where # indicates the mole percentage of excess thiol in the crosslinked MFTU networks) were completely synthesized (Figure 3.5). All MFTUs were fabricated with a $Zn(DTC)_2$ content of 2 mol %. As reported by Torkelson *et al.*, poly(thiourethane) maintained the crosslinked network even in excess thiol ratio [51]. In the case of MFTU, when the ratio of excess thiol in the network exceeds 10 mol %, the crosslinking density was significantly decreased, while the MFTU-10 showed an appropriate crosslinking density and excellent thermal properties (Table 3.1 and Figure 3.6). To verify the plasticity of poly(thiourethane) networks by respective catalysts, DBTDL-based poly(thiourethane) (DTU-10) was synthesized as a comparison sample (Figure 3.7). MFTU-10 showed complete stress-relaxation behavior within 3.5 min at 140 ℃ (Figure 3.8a). However, DTU-10 showed a stress-relaxation time of 11.5 min under the same conditions, which clearly attests that $Zn(DTC)_2$-based MFTU-10 exhibits dynamic thiourethane bond exchange-based plasticity better than DTU-10 (Figure

3.8). We compared the activation energies of thiourethane bond exchange under each catalysis. The relaxation times at 120, 140, 160, and 180 $^{\circ}$C were measured, and linear approximation was performed according to the Arrhenius equation. As a result, the activation energy of MFTU-10 (51.84 KJ mol^{-1}) was 42.9 % lower than that of DTU-10 (90.75 KJ mol^{-1}) (Figure 3.9 and Table 3.2). We assumed that the dynamic thiourethane bond exchange in bulk state is more facilitated than DBTDL due to the zinc and sulfurphilic diethyldithiocarbamate group in Zn(DTC)$_2$ [52]. MFTU-10, which has a faster relaxation time than DTU-10, can be reprocessed into a smooth film when hot-pressing at 140 $^{\circ}$C for 30 min, while the reprocessed DTU-10 film has a rough surface (Figure 3.10). However, due to its high crosslinking density, MFTU-10 did not show self-healing properties without external pressure (Figure 3.11).

To confirm whether MFTU-10 maintains mechanical properties after reprocessing, we performed tensile testing. As shown in Figure 3.12, MFTU-10 maintained excellent mechanical properties even after several reprocessing procedures compared to the pristine state. The MFTU-10 also showed enhanced extensibility because the random coil of linear chains in the network increase as the content of excess thiol increases (Figure 3.13 and Table 3.3) [51,53]. Therefore, MFTU-10 containing an appropriately excessive amount of thiol has excellent mechanical properties while exhibiting vitrimer properties based on fast stress-

relaxation behavior and excellent reprocessability. MFTU can be recycled via a similar method of the bulk polymerization process. With the addition of thiol (DODT and PETMP, ratio of 17:3 mol %), MFTU-10 network can be degraded by S_N2-type dynamic thiourethane bond exchange at 100 ºC (Figure 3.14). After HDI and $Zn(DTC)_2$ are added to the liquid-phase degraded MFTU to have a 10 mol % excess of thiol in the final product, bulk polymerized MFTU-10 can be obtained again, which exhibits recyclable characteristics [51,54,55].

3.2.2. Variable Stiffness Properties of MFTU

Generally, a semi-crystalline structure can be formed when flexible long alkyl chains are included in the main chain in a polymer [49,56]. Slightly reduced crosslinking density compared to MFTU-0, MFTU-10 forms a semi-crystalline structure due to the linear chains generated through the thiourethane reaction of DODT and HDI. Such crystalline structures induce the increased rigidity of the polymer network; hence, the stiffness of the MFTU is adjusted depending on whether the crystal structure is formed or not. We adjusted the PETMP content so the T_g was 2.4 ºC to facilitate the crystal structure formation at room temperature (Figure 3.4). Immediately after polymerization or reprocessing, MFTU-10 does not show crystallinity, but a semi-crystalline structure is formed due to the alignment

between the alkyl chains during 24 h. We designated the pliable MFTU-10 without crystallinity as MFTU-10-P and the rigid MFTU that forms a semi-crystalline structure as MFTU-10-R. As shown in Figure 3.15, we confirmed the crystalline behavior of the MFTU-10 by differential scanning calorimetry (DSC). MFTU-10-P and MFTU-10-R exhibited the similar glass transition temperatures (T_g). However, MFTU-10-R, which is formed after 24 h from MFTU-10-P at room temperature, showed a melting peak at 48.1 °C during the first heating.

To rheologically characterize the semi-crystalline structure in MFTU, we also conducted dynamic mechanical analysis (DMA) tests. The tan delta value of MFTU-10-R, indicating the melting transition of crystalline, was observed in addition to the T_g region (Figure 3.16). As a result of conducting a non-isothermal creep test using DMA, the strain value of MFTU-10-P increased rapidly after the T_g region and saturated before T_m region. Because the MFTU-10-P does not form a crystalline structure, it showed an amorphous behavior. Meanwhile, MFTU-10-R could not be stretched above the T_g region due to the semi-crystalline structure. Instead, the strain increases drastically above the temperature of the T_m region where the crystal melts. Above 100 °C, the strain values of MFTU-10-P and MFTU-10-R showed saturation tendency until the dynamic thiourethane bond exchange accelerating temperature of 140 °C (Figure 3.17).

To further investigate the semi-crystalline structure, detailed morphological

9 8

characterization of the MFTU-10-R was also performed using wide-angle X-ray scattering (WAXS) (Figure 3.18). At temperatures below 55 °C, the crystalline peak of MFTU-10-R was observed at $q = 1.43$ Å^{-1} and disappeared at temperatures above 55 °C. We confirmed that the distance between the linear chains in the MFTU-10 network at the crystalline peak via Bragg`s equation is only 4.39 Å. Therefore, it is assumed that the crystalline structure is not formed within a single chain but formed by packing of aligned linear chains within the MFTU network. As a result of deconvoluting the 1D WAXS profiles of MFTU-R through the Gaussian function, the area ratio of a single crystalline peak was about 10.3 %, confirming that it corresponds to the semi-crystalline region (Figure 3.19). To confirm the various stiffness according to the formation of a crystalline structure, the mechanical properties of MFTU-10-R with a semi-crystalline structure and MFTU-10-P were compared (Figure 3.20). MFTU-10-P, which does not form the crystalline structure showed a low Young's modulus of 2.9 MPa, while the MFTU-10-R showed a difference of 70.5 times than MFTU-10-P of 204.4 MPa (Tables 3.3 and 3.4). In addition, it was confirmed that the tensile strength of MFTU-10-R was 5.2 times higher than that of MFTU-10-P.

To verify whether MFTU-10 forms a crystalline structure after the reprocessing process, the stress-strain curves of the MFTUs after 24 h were monitored after reprocessing according to the mol percentage of excess thiol.

MFTU-10 and MFTU-20 consistently form a crystalline structure between linear chains even after reprocessing, whereas MFTU-0 is densely crosslinked, challenging to form a uniform crystalline structure after reprocessing (Figure 3.21). For the MFTU-20, which contains many flexible linear chains, exhibited a significant difference in mechanical properties between the rigid and pliable states (Figure 3.22). However, the MFTU-20 film has a low crosslinking density and cannot maintain its original shape in a pliable state, follows to sagging. Therefore, we set MFTU-10 as a representative sample with a distinct crosslinking density, stiffness variation, and excellent mechanical properties while containing an appropriate excess thiol. To conduct the stiffness variation test, we programmed the MFTU-10 films into the MFTU-10-R in the shape of a wheel and installed them under the glass substrate. As shown in Figure 3.23, four MFTU-10-R films made of a wheel shape endured a heavy weight of 1 kg. However, the crystalline structure of MFTU-10-R melted after the heat was applied. As a result, MFTU-10-R turns into MFTU-10-P, which undergoes collapsing due to the decreased stiffness. After removing the object, the collapsed MFTU-10-P films recovered the shape in the form of a wheel. Since the MFTU-10 forms a semi-crystalline structure within the crosslinked network, stiffness may vary due to crystalline melting while maintaining the permanent shape by the chain entanglement within the network. Since the storage modulus (E') is proportional to stiffness [57], we *in situ* measured

E' of MFTU-10-P at room temperature to further confirm the stiffness variation. Storage modulus of MFTU-10-P in the pliable state increased over time and changed to rigid MFTU-10-R after 24 h (Figure 3.24).

3.2.3. Reversible Assembly/Disassembly of MFTU Films via Hydrogen and Zn Coordination Bonds

Generally, coordination bonds between a zinc and ligands have negative Gibbs free energy, resulting in the thermodynamically favorable, suggesting that the metal-ligand complex is formed spontaneously under standard conditions [58]. Linear polymers exhibit self-healing properties through physical crosslinking with metal-ligand complexes [59-61]. However, crosslinked polymers are challenging to assemble between films due to the low flexibility of chains. To address the aforementioned challenges, we achieved reversible assembly/disassembly of MFTU films between surfaces through the synergistic effect of dissociation-reformation of H-bonds and $Zn(DTC)_2$ based Zn coordination bonds. Abundant linear chains with thiourethane and oligoether groups in the MFTU-10 network can induce the strong H-bond, while the thiol ligand in linear chains forms the coordination bond with zinc. To confirm the reversible assembly/disassembly by H-bond, FT-IR analysis was performed after heating MFTU-10 at 60 °C. As a result,

N–H and C=O bonding of thiourethane moieties showed free H-bond peaks (Figure 3.25 and 3.26) [62,63]. After cooling at room temperature, we observed the peak shifts from the free H-bond to the H-bonded according to the formation of H-bonding inside the MFTU-10 network over time.

As the formation of Zn coordination bond between zinc and thiol ligands is enable [64], MFTUs containing excess thiol content induce Zn coordination bonds, resulting in the ligand exchanges [65]. We fabricated a modeling compound and performed *in-situ* ^{1}H NMR characterization at temperatures of 10, 25, and 45 ^{o}C to confirm the ligand exchange (Figure 3.27). The modeling compound was fabricated with a mole ratio of DODT and Zn(DTC)$_2$ of 1:4. As the temperature increased from 10 ^{o}C to 45 ^{o}C, we observed the peak aggregation of −S−CH$_2$− peaks (2.7 ppm) and −SH peaks (1.58 ppm), respectively. Peak broadening appeared due to the thiol ligand exchanges in the MFTU [66]. However, since Sn is less-electronegative than Zn, thiolate ligand exchange is relatively challenging [67]. Therefore, peak aggregation was not observed with temperature in the compound prepared with a mol ratio of DODT and DBTDL of 1:4 (Figure 3.28).

Based on the dissociation-reformation of hydrogen and Zn coordination bonds, we realized the reversible assembly/disassembly of the MFTU films by applying heat of 60 ^{o}C to the two MFTU films. We analyzed the force-extension curves of the assembled MFTU films according to excess thiol content to confirm the

interfacial assembly of the films (Figure 3.29). Assembled MFTU films are not welded state, so their mechanical properties are inferior to those of the pristine state. Meanwhile, MFTU-20, which has 20 mol % excess thiol, exhibited the highest tensile forces due to the increased sites of H-bonds and Zn coordination bonds. The assembled representative MFTU-10 sample could lift a heavy weight of 200 g (Figure 3.30). However, after the heat applies at 60 $^{\circ}$C, it was hard to support the weight, and the two MFTU-10 films were disassembled from each other. In addition, when reattaching the fracture surfaces after physically fracturing MFTU films at room temperature, they could be assembled without heat treatment (Figure 3.31 and 3.32). We assumed that flexible linear chains with thiol end-groups induce strong H-bonds and Zn coordination bonds enable the assembled MFTU-10 to carry heavy weights while enduring without being disassembled.

3.2.4. MFTU for Transformable and Recyclable 3D Soft Robot Applications

We applied the 2D multifunctional MFTU films as a 3D soft robot capable of transforming through welding and reversible assembly/disassembly, with controlling magnetic actuation through stiffness modulation. To enable MFTU-10 to perform actuation under a magnetic field, we prepared MFTU-10-Fe_3O_4

composite by dispersing Fe_3O_4 particles in thiol monomers and bulk polymerized. As shown in Figure 3.33, we welded MFTU-10-Fe_3O_4 composite film onto flat pristine MFTU-10 film, shape fixed as a permanently curved shape, resulting in the fabrication of building blocks corresponding to the parts of the palm and finger. The palm and finger building block parts made of MFTU-10 and MFTU-10-Fe_3O_4 were assembled into a soft hand robot after the heat treatment. Based on the various stiffness properties of the MFTU-10, we compared the actuation in the magnetic field when the finger part is in rigid or pliable states (Figure 3.34). When the finger part was in the MFTU-10-R state, the fingernail corresponding to the MFTU-10-Fe_3O_4 part could not actuate to the bottom surface in response to the magnetic field. Meanwhile, when the finger part was in the MFTU-10-P state, the fingernail part gradually acted toward the bottom surface in response to the magnetic field over time, and shape recovery was observed after the magnetic field was removed. Confirming the actuation of the soft hand robot in the magnetic field could be controlled according to the various stiffness between MFTU-10-R and MFTU-10-P, we performed a rock scissors paper game between two soft hand robots according to the stiffness states (Figure 3.35). After rigid or pliable programming was performed on the finger parts of each soft hand robot, a first-round game was played under the magnetic field. Since both soft hand robots were programmed only for the index and middle finger parts as pliable state, both robots actuated with scissors,

and the first-round game ended as a draw. Again, after programming to rigid or pliable states was performed on each soft hand robot, a second-round game was played under the magnetic field. The left-side soft hand robot actuated as paper because all fingers were programmed to be pliable. In the meantime, the right-side soft hand robot actuated as scissors because only the index and middle finger parts were programmed to pliable state, winning the second-round game.

We disassembled the soft hand robots that played the rock scissors paper game back into building blocks. The disassembled building blocks were welded into soft receivers after permanent shape fixing to U-shape (Figure 3.36). After programming the soft receiver in a rigid state for 24 h, we conducted a receiving demonstration for the object of 10 g dropped from a height of 12 cm (Figure 3.37). U-shape parts in the MFTU-10-R state, where actuation in the magnetic field is impossible due to high stiffness, bounced off the object. When heat treatment was applied to U-shape parts of 50 $^\circ$C in the MFTU-10-R state, they were programmed as MFTU-10-P. Due to the lowered stiffness, shape deformation of the soft receiver was enabled after dropping the object (Figure 3.38). The U-shaped parts of the MFTU-10-P state received the object with safe landing, and shape-deformed parts actuated to wrap the object under the magnetic field. After reprogramming the MFTU-10-P parts to MFTU-10-R of the soft receiver, which was wrapping the object, we flipped the soft receiver. We demonstrated the flipped soft receiver as a

gripping actuation of the object under the rigid state and cargo delivery to the target place under a pliable state. When the heat treatment of 50 ^{o}C was applied to the flipped soft receiver, the stiffness of MFTU-10 was modulated from rigid to pliable state. Therefore, MFTU-10-P parts could not bear the weight of the object, and the flipped soft receiver dropped the object. After the building blocks were fabricated into the soft hand robot and transformed into the soft receiver, parts of MFTU-10 and MFTU-10-Fe$_3$O$_4$ were recycled in a composite state (Figure 3.14 and 3.39). When the soft receiver was input to the vial and was stirred at 100 ^{o}C with excess thiol addition, it became a degraded MFTU composite of oligomer units [54,55]. The degraded MFTU was vortexed by adding HDI and Zn(DTC)$_2$ after separating the Fe$_3$O$_4$ particles with a magnet. Then, the fresh Lego-shaped MFTU-10 product was obtained after pouring the mixture into a Lego-shaped mold for bulk polymerization. In addition, we compared the mechanical properties of the pristine MFTU-10-P and the recycled MFTU-10-P, confirming that they had similar properties (Figure 3.40).

3.3. Conclusion

In conclusion, we synthesized a multifunctional poly(thiourethane) network (MFTU) based on a thiol end-group linear chain at the end by adding excess thiol. Under the newly introduced $Zn(DTC)_2$ catalysis, dynamic thiourethane bond exchange of MFTU-10 was facilitated and showed excellent reprocessability and recycling characteristics. As the MFTU-10 forms a semi-crystalline structure due to flexible linear chains at the end of the network, we modulated the stiffness of the MFTU-10 based on the melting temperature (T_m). In addition, MFTU-10 containing excess thiol enables dissociation-reformation of hydrogen and Zn coordination bonds, resulting in reversible assembly/disassembly between MFTU-10 films. We fabricated a multifunctional transformable 3D soft robot through the variable stiffness and reversible assembly/disassembly of the MFTU-10 and even realized the actuation under the magnetic field according to composite with magnetic particles. We anticipate that this multifunctional dynamic covalent polymer network fabrication strategy provides insight for advanced materials in various adaptable fields, such as shape morphing architectures, adaptable soft robots, and reliable electronic devices.

3.4. Experimental

Materials: Hexamethylene diisocyante (HMDI, ≥99.0%), 2,2′-(Ethylenedioxy)diethanethiol (DODT, 95%), Pentaerythritol tetrakis(3-mercaptopropionate) (PETMP, >95%), Zinc diethyldithiocarbamate ((ZnDTC)$_2$, 97%), Dibutyltin dilaurate (DBTDL, 95%), Iron(II,III) oxide (Fe$_3$O$_4$, powder, <5um, 95%), and N,N-dimethylformamide (DMF, anhydrous, 99.8%) were from Sigma-Aldrich. All chemicals were used as received without further purification.

Preparation of MFTUs: we designated the MFTU vitrimers as MFTU-#, where # indicates the mole percentage of excess thiol in the crosslinked MFTU networks. For the synthesis of MFTU-10, HMDI (2 g, 11.89 mmol.), PETMP (0.79 g, 1.63 mmol), DODT (1.79 g, 9.81 mmol) and Zn(DTC)$_2$ (0.17 g, 2 mol % in total monomers) were mixed via vortex for 1 min. The resulting homogeneous mixture was poured into a Teflon petri dish. After 30 min, the transparent yellowish MFTU product was obtained. MFTU-10 product was hot pressed at 140 ^{o}C under 10 Mpa for 30 min using 500um thick mold to get uniform MFTU-10 film with 0.5 mm thickness. For the MFTU-0 and MFTU-20, ratio of DODT and PETMP was maintained as 17 : 3 mol %. DTU-10 was synthesized with 2 mol % of DBTDL, instead of Zn(DTC)$_2$.

Preparation of MFTU-10-Fe$_3$O$_4$ composite film: Fe$_3$O$_4$ particles were added

to be 20 wt % of the weight of the MFTU-10-Fe$_3$O$_4$ composite. Then, thiol and Zn(DTC)$_2$ were added and vortexed to make the Fe$_3$O$_4$ particles homogeneous in the liquid phase, and HDI was added to fabricate the MFTU-10-Fe$_3$O$_4$ composite. MFTU-10-Fe$_3$O$_4$ composite film was obtained after hot pressing under the same conditions as for MFTU film production.

Fabrication of modeling compound for ligand exchange: DODT (0.73 g, 40 mmol) and Zn(DTC)$_2$ (0.36 g, 10 mmol) was mixed homogeneously via magnet stirrer for 1 h.

Preparation of soft hand robot and soft receiver: After welding the MFTU-10-Fe$_3$O$_4$ composite film (5 mm × 60 mm × 0.5 mm) to the MFTU-10 film (17 mm × 60 mm × 0.5 mm) at 140 ^{o}C. During the welding process, MFTU-10 film was permanently fixed to a curved shape at 90°. Building blocks (17 mm × 4 mm × 0.5 mm) of soft robots were fabricated by cutting the welded MFTU film at intervals of 4 mm. Areas of 4 mm × 2 mm at the extremities of the building blocks are heated at 60 ^{o}C, assembled on a 25 mm × 25 mm MFTU-10 film, and fabricated to a soft hand robot.

Transformation of soft hand robot to soft receiver: The building blocks are obtained by disassembling from a soft hand robot heated to 60 ^{o}C. The soft receiver is fabricated by welding the building blocks of the finger part to a 25 mm × 25 mm MFTU-10 film after permanent shape fixing to a U-shape at 140 ^{o}C.

Recycling of soft receiver: After the soft receiver was placed in a 100 ml vial, DODT and PETMP were added in the ratio of 17 : 3 mol % so that the final MFTU product was three times the weight of the soft receiver. The mixture of soft receiver and thiols were stirred at 100 °C for 3 h. Composed of thiol-terminated oligomers, degraded MFTU-10 liquid phase mixture was separated from Fe_3O_4 particles using a magnet. After transferring the separated mixture to another vial, HDI and $Zn(DTC)_2$ were added in an amount to obtain MFTU-10. The mixture was vortexed and poured into a Lego-shaped mold. After 30 min, a Lego-shaped MFTU-10 recycled soft receiver was obtained.

Instrumental and characterization techniques: in-situ ^{1}H-NMR spectra of coordination modeling was recorded on a Bruker Avance III 500 MHz using chloroform as solvent. Fourier transform infrared (FT-IR) spectra were recorded on an Agilent 4100 Exoscan FTIR spectrometer using attenuated total reflectance (ATR) equipment. Gel fraction (f_g) test was performed by placing a small piece (ca. 60 mg) of films into 20 ml vial filled with DMF. After stored at 25 °C for 24 h, MFTU films were dried at 100 °C under vacuum for 24 h. Gel fraction was calculated using the equation (1) below,

$$f_g = W_a / W_d \tag{1}$$

where W_d and W_a are the weights of dried film before and after the DMF solvent extraction. The thermal stability of MFTU was investigated by thermal gravimetric

analysis (TGA) using a TA Instruments TGA Q5000 under a nitrogen atmosphere. The samples were first heated to 100 °C and maintained at 100 °C for 10 min in order to evaporate residual water, and then heated to 700 °C at a heating rate of 10 °C min^{-1}. Differential scanning calorimetry (DSC) was run using a TA Instruments DSC Q1000 under a nitrogen atmosphere. Samples with a typical mass of 5–10 mg were encapsulated in sealed aluminum pans. They were heated –35 °C to 150 °C at a constant rate of 10 °C min^{-1} to characterization of T_g and crystalline region. Wide-angle X-ray scattering (WAXS) measurements were conducted at the 9A beamline at Pohang Accelerator Laboratory (PAL), Korea. The typical operating conditions were set at a wavelength of 0.6259 Å and sample-to-detector distance of 378.4245 mm. All the measurements were performed at 25 °C to 150 °C with an exposure time of 10 s. From recorded 2D patterns, a 1D intensity profile versus the scattering vector $q = (4\pi / \lambda) \sin(\theta)$ was obtained, where λ is the wavelength of the X-ray (1.54 Å) and θ is the scattering angle. Tensile storage modulus (E'), tensile loss modulus (E'') and tan δ ($\delta = E'' / E'$) data were obtained by temperature sweep experiments in multi-frequency-strain mode with a frequency of 1 Hz and a strain of 1 % using dynamic mechanical analysis (DMA; Q800; TA Instruments). The temperature was increased at a rate of 5 °C min^{-1} from –50 to 200 °C. Crosslinking density (v_e) of the vitrimers was calculated by Flory's rubber elasticity theory (Equation below) as follows,

1 1 1

$$v_e = E'_{high} / 3RT_{high} \tag{2}$$

where E', R, and T are the storage modulus at rubbery plateau region (ca. 393 K), universal gas constant (8.314 cm^3 MPa K^{-1} mol^{-1}), and absolute temperature (393 K), respectively. The stress relaxation behaviors of samples were obtained by the same TA Instruments DMA Q800 under stress relaxation mode. All samples were subjected to an instantaneous strain of 10 % and equilibrated at temperatures 120, 140, 160, and 180 °C for 5 min. The equilibrated samples were subjected to stress relaxation analysis while maintaining a constant strain (10 %) until the stress relaxation modulus was relaxed to less than 37 % (e^{-1}) of the initial value. For the non-isothermal creep test, the temperature was ramped from –50 to 200 °C with a ramp rate of 5 °C min^{-1} at a deformation frequency of 1 Hz. The applied axial force in all non-isothermal creep experiments was 0.2 N. To monitor the crystallization of MFTU-10, the storage modulus (E') was *in situ* measured for 24 h at 25 ^{o}C with a deformation frequency of 1 Hz and dynamic strain of 0.3 %. Uniaxial tensile testing was performed on an Instron LR5K universal testing machine (UTM, Lloyd Instruments) at a strain rate of 10 mm min^{-1}. For the force-extension test, MFTU-10 films were assembled after heat treatment at 60 ^{o}C after overlapping the size of 5 mm × 5 mm, then measured via UTM instrument. All samples for DMA and UTM measurement were fabricated as rectangular-shape (50 mm (L) x 5 mm (W) × 0.5 mm (T)). The actuation of the soft hand robot and soft receiver at magnetic field

used a custom-made electromagnet with a magnetic field of 3.5 mT, measured by

TM-801EXP KANETEC equipment.

3.5. References

[1] D. Montarnal, M. Capelot, F. Tournilhac, L. Leibler, *Science* **2011**, 334, 965–968.

[2] W. Denissen, J. M. Winne, F. E. Du Prez, *Chem. Sci.* **2016**, 7, 30–38.

[3] M. Guerre, C. Taplan, J. M. Winne, F. E. Du Prez, *Chem. Sci.* **2020**, 11, 4855–4870.

[4] N. J. Van Zee, R. Nicolaÿ *Prog. Polym. Sci.* **2020**, 104, 101233.

[5] Y. Yang, Y. Xu, Y. Ji, Y. Wei, *Prog. Mater Sci.* **2021**, 120, 100710.

[6] J. Zheng, Z. M. Png, S. H. Ng, G. X. Tham, E. Ye, S. S. Goh, X. J. Loh, Z. Li, *Mater. Today* **2021**, 51, 586–625.

[7] A. M. Hubbard, Y. Ren, P. Papaioannou, A. Sarvestani, C. R. Picu, D. Konkolewicz, A. K. Roy, V. Varshney, D. Nepal, *ACS Appl. Polym. Mater.* **2022**, 4, 6374–6385.

[8] V. Schenk, K. Labastie, M. Destarac, P. Olivier, M. Guerre, *Mater. Adv.* **2022,** 3, 8012–8029.

[9] L. Chen, W. Li, Y. Liu, J. Leng, *Composites part B: engineering* **2016**, 91, 75–82.

[10] Y. Yang, Z. Pei, Z. Li, Y. Wei, Y. Ji, *J. Am. Chem. Soc.* **2016**, 138, 2118–2121.

[11] Z. Yang, Q. Wang, T. Wang, *ACS Appl. Mater. Interfaces* **2016**, 8, 21691–

21699.

[12] C. Xiong, M. Li, W. Zhao, C. Duan, L. Dai, M. Shen, Y. Xu, Y. Ni, *Chem. Eng. J.* **2020**, 396, 125318.

[13] M. O. Saed, A. Gablier, E. M. Terentjev, *Chem. Rev.* **2021**, 122, 4927–4945.

[14] Z. Li, Y. Yang, Z. Wang, X. Zhang, Q. Chen, X. Qian, N. Liu, Y. Wei, Y. Ji, *J. Mater. Chem. A* **2017**, 5, 6740–6746.

[15] G. Dong, Q. He, S. Cai, *Soft Matter* **2022**, 18, 7604–7611.

[16] J. H. Hwang, J. Shin, J. Han, Y.-S. Choi, S. Park, Y. H. Kim, Y. S. Kim, H. S. Kang, D.-G. Kim, J.-C. Lee, *Advanced Intelligent Systems* **2022**, 4, 2200051.

[17] S. Wang, S. Ma, Q. Li, X. Xu, B. Wang, W. Yuan, S. Zhou, S. You, J. Zhu, *Green chem.* **2019**, 21, 1484–1497.

[18] H. Si, L. Zhou, Y. Wu, L. Song, M. Kang, X. Zhao, M. Chen, *Compos. B. Eng.* **2020**, 199, 108278.

[19] T. Liu, C. Hao, L. Shao, W. Kuang, L. Cosimbescu, K. L. Simmons, J. Zhang, *Macromol. Rapid Commun.* **2021**, 42, 2000458.

[20] J. Deng, X. Kuang, R. Liu, W. Ding, A. C. Wang, Y. C. Lai, K. Dong, Z. Wen, Y. Wang, L. Wang, *Adv. Mater.* **2018**, 30, 1705918.

[21] Z. Feng, W. Zhao, Z. Yang, Y. Deng, T. Yang, Y. Ni, *J. Mater. Chem. A* **2022**, 10, 11524–11534.

[22] W. Gu, F. Li, T. Liu, S. Gong, Q. Gao, J. Li, Z. Fang, *Adv. Sci.* **2022**, 9,

2103623.

[23] C. Xiong, M. Li, Q. Han, W. Zhao, L. Dai, Y. Ni, *J. Mater. Sci. Technol.* **2022**, 97, 190–200.

[24] S. Wolf, G. Grioli, O. Eiberger, W. Friedl, M. Grebenstein, H. Höppner, E. Burdet, D. G. Caldwell, R. Carloni, M. G. Catalano, *IEEE/ASME Trans. Mechatron.* **2015**, 21, 2418–2430.

[25] G. G. Lozano, A. Tiwari, C. Turner, S. Astwood, *Proc. Inst. Mech. Eng. B. J. Eng. Manuf.* **2016**, 230, 981–992.

[26] I. K. Kuder, A. F. Arrieta, W. E. Raither, P. Ermanni, *Prog. Aerosp. Sci.* **2013**, 63, 33–55.

[27] S. Sun, J. Yang, W. Li, H. Deng, H. Du, G. Alici, *Smart Mater. Struct.* **2015**, 24, 085021.

[28] L. M. Jugulkar, S. Singh, S. M. Sawant, *Adv. Mech. Eng.* **2016**, 8, 1687814016648638.

[29] B. Aksoy, H. Shea, *Adv. Funct. Mater.* **2020**, 30, 2001597.

[30] D. Cao, J. G. Martinez, E. S. Hara, E. W. Jager, *Adv. Mater.* **2022**, 34, 2107345.

[31] J. Shintake, V. Cacucciolo, D. Floreano, H. Shea, *Adv. Mater.* **2018**, 30, 1707035.

[32] T. T. Hoang, J. J. S. Quek, M. T. Thai, P. T. Phan, N. H. Lovell, T. N. Do, *Sens. Actuator. A Phys.* **2021**, 323, 112673.

[33] R. Coulson, C. J. Stabile, K. T. Turner, C. Majidi, *Soft Robot.* **2022**, 9, 189–200.

[34] W. Dou, G. Zhong, J. Cao, Z. Shi, B. Peng, L. Jiang, *Adv. Mater. Technol.* **2021**, 6, 2100018.

[35] Y. Yang, Y. Li, Y. Chen, *Bio-Des. Manuf.* **2018**, 1, 14–25.

[36] L. Blanc, A. Delchambre, P. Lambert, *Actuators* **2017**, 6, 23.

[37] M. Cianchetti, C. Laschi, A. Menciassi, P. Dario, *Nat. Rev. Mater.* **2018**, 3, 143–153.

[38] M. Runciman, A. Darzi, G. P. Mylonas, *Soft robot.* **2019**, 6, 423–443.

[39] M. Xie, M. Zhu, Z. Yang, S. Okada, S. Kawamura, *Nano Energy* **2021**, 79, 105438.

[40] M. Mattmann, C. De Marco, F. Briatico, S. Tagliabue, A. Colusso, X. Z. Chen, J. Lussi, C. Chautems, S. Pané, B. Nelson, *Adv. Sci.* **2022**, 9, 2103277.

[41] A. Andersen, M. Krogsgaard, H. Birkedal, *Biomacromolecules* **2017**, 19, 1402–1409.

[42] H.-Q. Wang, Z.-Y. Huang, D.-W. Yue, F.-Z. Wang, C.-H. Li, *Mater. Horiz.* **2023**, 10, 908–917.

[43] S. Ji, X. Wu, Y. Jiang, T. Wang, Z. Liu, C. Cao, B. Ji, L. Chi, D. Li, X. Chen, *ACS Nano* **2022**, 16, 16833–16842.

[44] J. Joe, J. Shin, Y. S. Choi, J. H. Hwang, S. H. Kim, J. Han, B. Park, W. Lee, S.

Park, Y. S. Kim, *Adv. Sci.* **2021**, 8, 2103682.

[45] S. Zhang, T. Liu, C. Hao, L. Wang, J. Han, H. Liu, J. Zhang, *Green Chem.* **2018**, 20, 2995–3000.

[46] A. Trejo-Machin, L. Puchot, P. Verge, *Polym. Chem.* **2020**, 11, 7026–7034.

[47] J. Y. Lim, Q. Lin, C. K. Liu, L. Guo, K. Xue, X. J. Loh, *Mater. Adv.* **2020**, 1, 3221–3232.

[48] C.-J. Fan, Z.-B. Wen, Z.-Y. Xu, Y. Xiao, D. Wu, K.-K. Yang, Y.-Z. Wang, *Macromolecules* **2020**, *53*, 4284–4293.

[49] F. Stempfle, P. Ortmann, S. Mecking, *Chem. Rev.* **2016**, 116, 4597–4641.

[50] J. Xu, X. Wang, X. Zhang, Y. Zhang, Z. Yang, S. Li, L. Tao, Q. Wang, T. Wang, *Chem. Eng. J.* **2023**, 451, 138673.

[51] L. Li, X. Chen, J. M. Torkelson, *Macromolecules* **2019**, 52, 8207–8216.

[52] X. Wu, J. A. Smith, S. Petcher, B. Zhang, D. J. Parker, J. M. Griffin, T. Hasell, *Nat. Commun.* **2019**, 10, 647.

[53] E. J. Cha, D. S. Lee, H. Kim, Y. H. Kim, B. G. Kim, Y. Yoo, Y. S. Kim, D.-G. Kim, *RSC Adv.* **2019**, 9, 15780–15784.

[54] C. Cui, X. Chen, L. Ma, Q. Zhong, Z. Li, A. Mariappan, Q. Zhang, Y. Cheng, G. He, X. Chen, Z. Dong, L. An, Y. Zhang, *ACS Appl. Mater. Interfaces* **2020**, 12, 47975–47983.

[55] A. S. Kuenstler, J. J. Hernandez, M. Trujillo-Lemon, A. Osterbaan, C. N.

Bowman, *ACS Appl. Mater. Interfaces* **2023**, 15, 11111–11121.

[56] H. Busch, S. Majumder, G. n. Reiter, S. Mecking, *Macromolecules* **2017**, 50, 2706–2713.

[57] H. H. Winter, *Korea Aust. Rheol. J.* **1999**, 11, 275–278.

[58] C. H. Li, J. L. Zuo, *Adv. Mater.* **2020**, 32, 1903762.

[59] C.-H. Li, C. Wang, C. Keplinger, J.-L. Zuo, L. Jin, Y. Sun, P. Zheng, Y. Cao, F. Lissel, C. Linder, X.-Z. You, Z. Bao, *Nat. Chem.* **2016**, 8, 618–624.

[60] J.-C. Lai, L. Li, D.-P. Wang, M.-H. Zhang, S.-R. Mo, X. Wang, K.-Y. Zeng, C.-H. Li, Q. Jiang, X.-Z. You, J.-L. Zuo, *Nat. Commun.* **2018**, 9, 2725.

[61] J.-C. Lai, X.-Y. Jia, D.-P. Wang, Y.-B. Deng, P. Zheng, C.-H. Li, J.-L. Zuo, Z. Bao, *Nat. Commun.* **2019**, 10, 1164.

[62] I. S. Ryu, X. Liu, Y. Jin, J. Sun, Y. J. Lee, *RSC Adv.* **2018**, 8, 23481–23488.

[63] Y. Xue, C. Li, W. Wang, Z. Liu, Z. Guo, J. Tan, Q. Zhang, *Macromol. Rapid Commun.* **2022**, 43, 2100510.

[64] W. M. Seo, M. Ballesteros, E. Y. Tsui, *J. Am. Chem. Soc.* **2022**, 144, 20630–20640.

[65] W. Maret, K. S. Larsen, B. L. Vallee, *Proc. Natl. Acad. Sci. U. S. A.* **1997**, 94, 2233–2237.

[66] M. Kluenker, M. Mondeshki, M. N. Tahir, W. Tremel, *Langmuir* **2018**, 34, 1700–1710.

[67] J. Xie, L. Wang, J. S. Anderson, *Chem. Sci.* **2020**, 11, 8350–8372.

Table 3.1. Gel fraction and crosslinking density of MFTUs by different excess thiol ratio.

Sample	f_g[a] (%)	E'_{high}[b] (MPa)	v_e [c] (mol m⁻³)
MFTU-0	89.92	6.85 ± 0.7	659.90
MFTU-10	85.89	3.01 ± 0.5	303.40
MFTU-20	62.93	1.04 ± 0.2	104.96

[a]Gel fraction of MFTUs from DMF solvent extraction. [b]Storage modulus of the MFTUs at the rubbery plateau. [c]Crosslinking densities of the MFTUs.

Table 3.2. Determined average relaxation times from stress relaxation measurements.

Sample	at 120 °C		at 140 °C		at 160 °C		at 180 °C	
	time (s)	*τ*[a] *(s)*	*time (s)*	*τ (s)*	*time (s)*	*τ (s)*	*time (s)*	*τ (s)*
MFTU-10	722.67	6.58	224.23	5.41	120.36	4.79	88.17	4.48
DTU-10	3461.52	8.15	721.29	6.58	172.35	5.15	96.01	4.56
MFTU-0	271.61	5.60	108.12	4.68	78.22	4.36	71.69	4.27
DTU-0	3525.07	8.17	414.32	6.03	156.91	5.06	88.51	4.48

[a] Representative relaxation time value ($\tau = \ln (t)$ (t is time)).

Table 3.3. Mechanical properties of MFTU-0-P, MFTU-10-P, and MFTU-20-P films (pristine, 1st, and 2nd reprocessed, respectively).

Sample name	E[a] (MPa)	ε_b[a] (%)	σ_y[a] (MPa)
Pristine MFTU-0-P	6.1 ± 1.5	199.1 ± 15.3	8.6 ± 0.8
1st Reprocessed MFTU-0-P	5.4 ± 0.3	170.7 ± 6.4	5.8 ± 0.7
2nd Reprocessed MFTU-0-P	4.7 ± 0.4	204.5 ± 0.3	5.5 ± 0.3
Pristine MFTU-10-P	2.9 ± 0.4	403.5 ± 12.9	5.4 ± 0.4
1st Reprocessed MFTU-10-P	2.6 ± 0.8	412.3 ± 5.9	5.3 ± 0.03
2nd Reprocessed MFTU-10-P	2.6 ± 0.2	400.5 ± 14.1	5.4 ± 0.2
Pristine MFTU-0-P	0.9 ± 0.2	522.3 ± 9.7	1.9 ± 0.1
1st Reprocessed MFTU-20-P	0.6 ± 0.1	481.0 ± 5.6	1.7 ± 0.2
2nd Reprocessed MFTU-20-P	0.8 ± 0.1	468.4 ± 11.7	1.7 ± 0.1

[a] Determined from tensile testing at room temperature (24 ± 1 °C) and a strain rate of 0.013 s^{-1}, where E, σ_y, and ε_b are elastic modulus, strain at break, and yield stress, respectively.

Table 3.4. Mechanical properties of MFTU-0-R, MFTU-10-R, and MFTU-20-R films (pristine, 1st, and 2nd reprocessed, respectively).

Sample name	$E^{[a]}$ (MPa)	$\varepsilon_b^{[a]}$ (%)	$\sigma_y^{[a]}$ (MPa)
Pristine MFTU-0-R	6.9 ± 0.8	195.6 ± 4.3	13.9 ± 0.5
1st Reprocessed MFTU-0-R	4.7 ± 1.3	151.2 ± 4.2	6.7 ± 0.4
2nd Reprocessed MFTU-0-R	4.4 ± 1.0	172.0 ± 9.1	7.8 ± 0.6
Pristine MFTU-10-R	204.4 ± 10.7	202.5 ± 19.1	25.7 ± 1.3
1st Reprocessed MFTU-10-R	205.9 ± 3.0	211.6 ± 6.7	23.0 ± 1.2
2nd Reprocessed MFTU-10-R	201.8 ± 2.6	220.7 ± 9.0	22.6 ± 0.7
Pristine MFTU-0-R	280.0 ± 38.9	50.2 ± 1.0	28.9 ± 2.8
1st Reprocessed MFTU-20-R	237.5 ± 12.7	49.6 ± 3.5	23.9 ± 0.1
2nd Reprocessed MFTU-20-R	264.2 ± 34.8	53.0 ± 9.8	24.8 ± 0.8

[a] Determined from tensile testing at room temperature (24 ± 1 °C) and a strain rate of 0.013 s^{-1}, where E, σ_y, and ε_b are elastic modulus, strain at break, and yield stress, respectively.
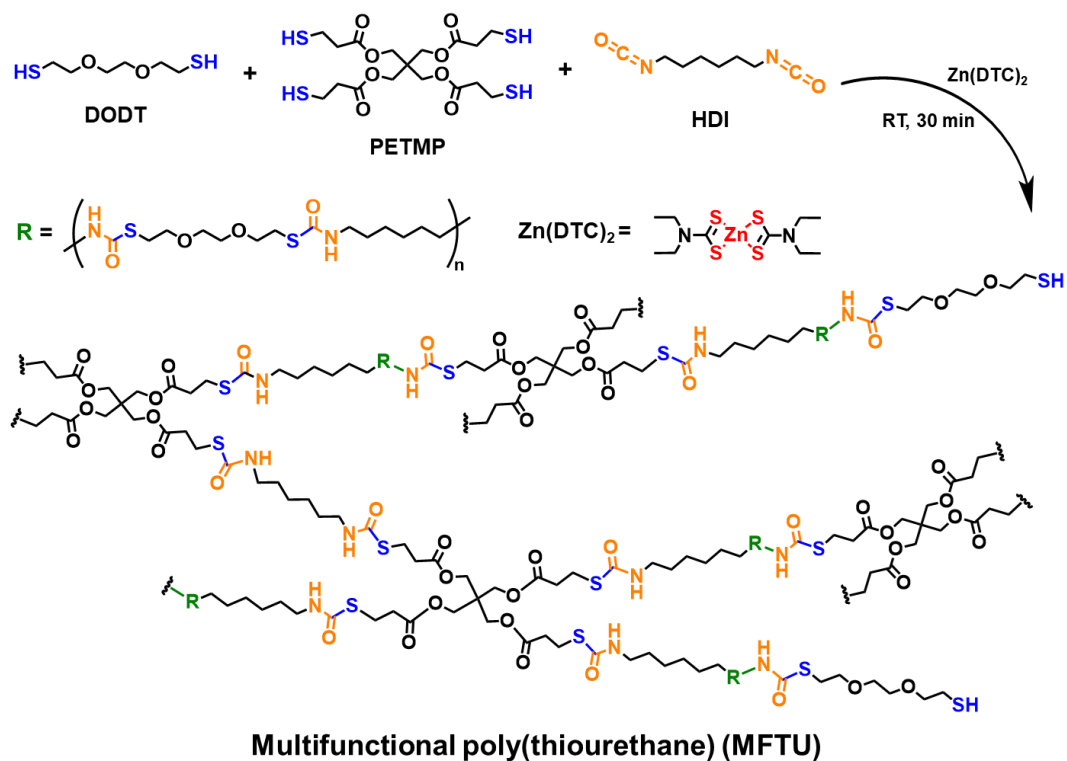
Figure 3.1. Schematic chemical structures for the synthesis of excess thiol multifunctional poly(thiourethane) (MFTU).
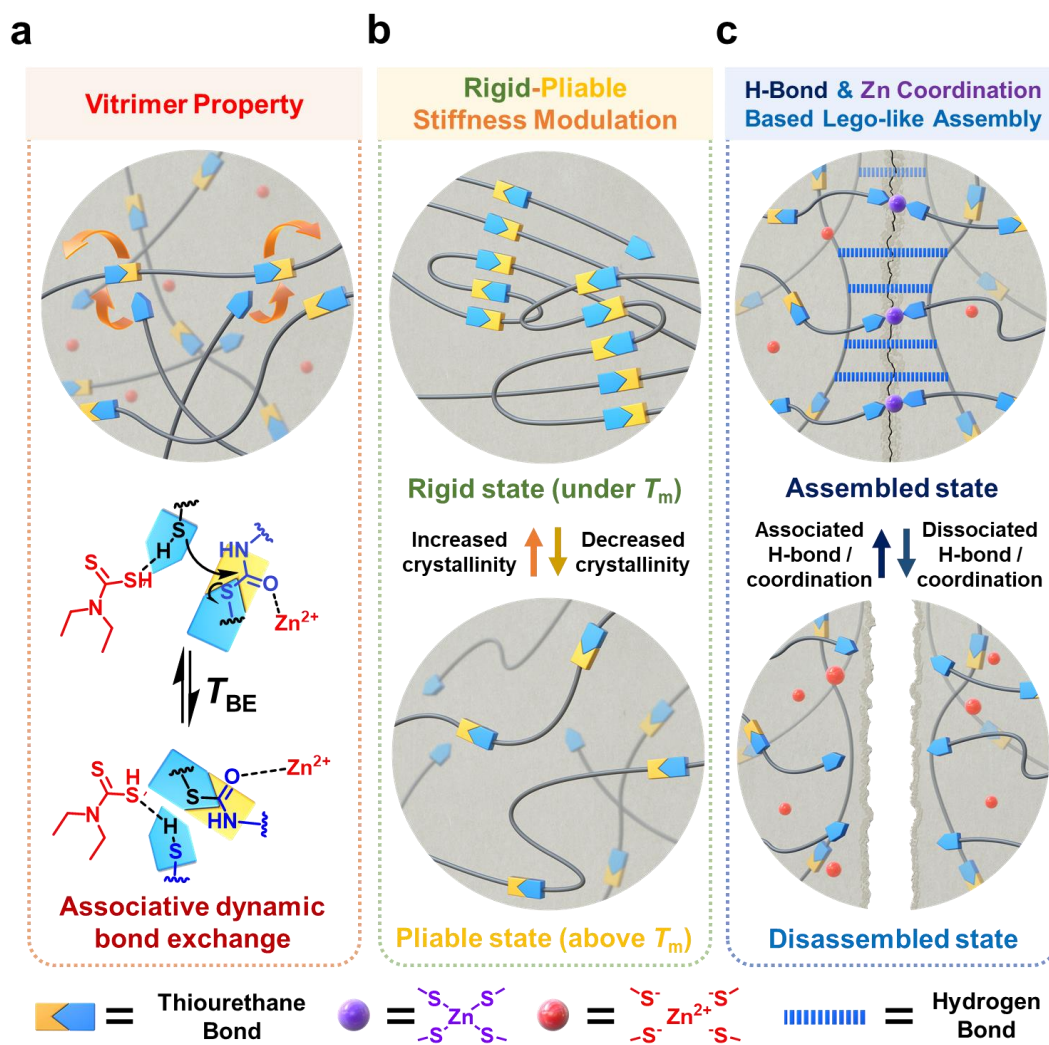
Figure 3.2. Schematic illustrations of the MFTU with (a) vitrimer properties via dynamic thiourethane bond exchange under Zn(DTC)$_2$ catalysis, (b) stiffness modulation to rigid and pliable states via controlling crystallinity, and (c) Lego-like reversible assembly/disassembly through hydrogen and Zn coordination bond.

1 2 6
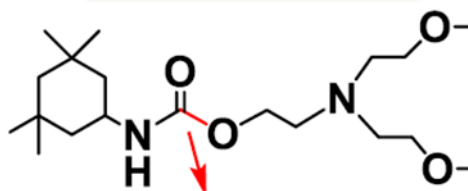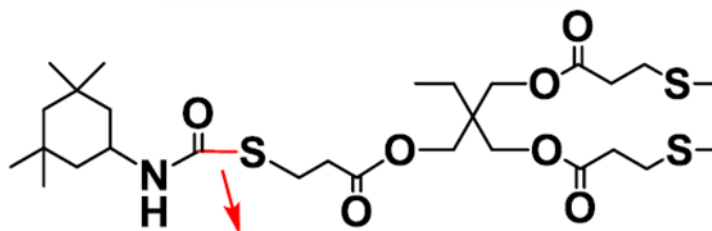
Figure 3.3. Bond lengths and bond dissociation energies of (a) urethane bond and (b) thiourethane bond.
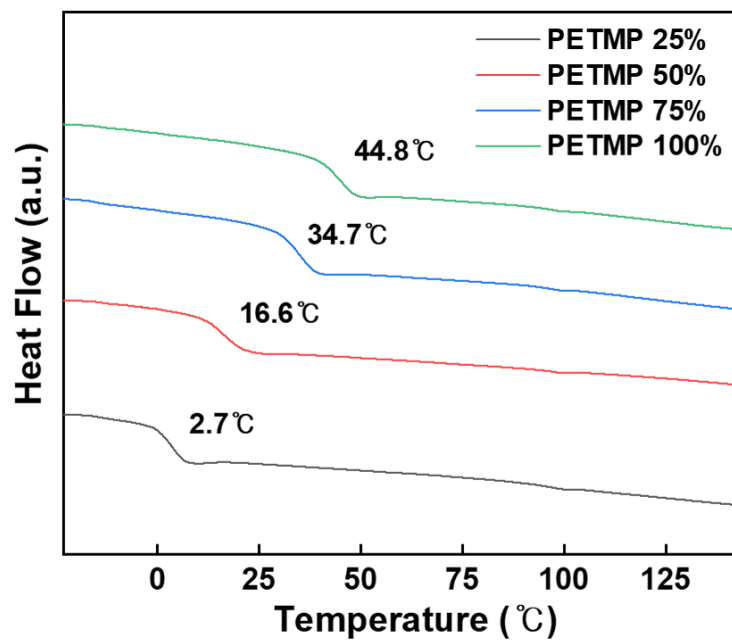
Figure 3.4. DSC thermograms of poly(thiourethane) by different ratio of PETMP with excess thiol of 10 mol %.
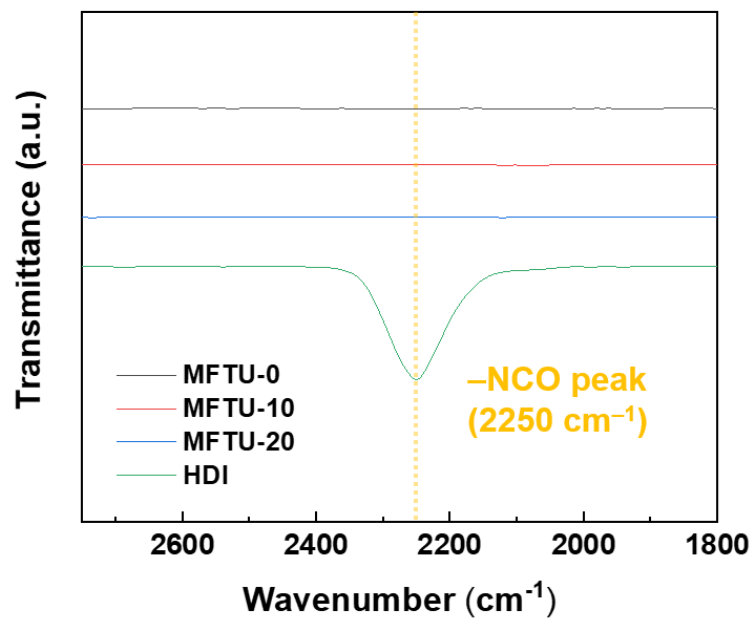
Figure 3.5. FT-IR spectra of MFTUs by different excess thiol ratio.
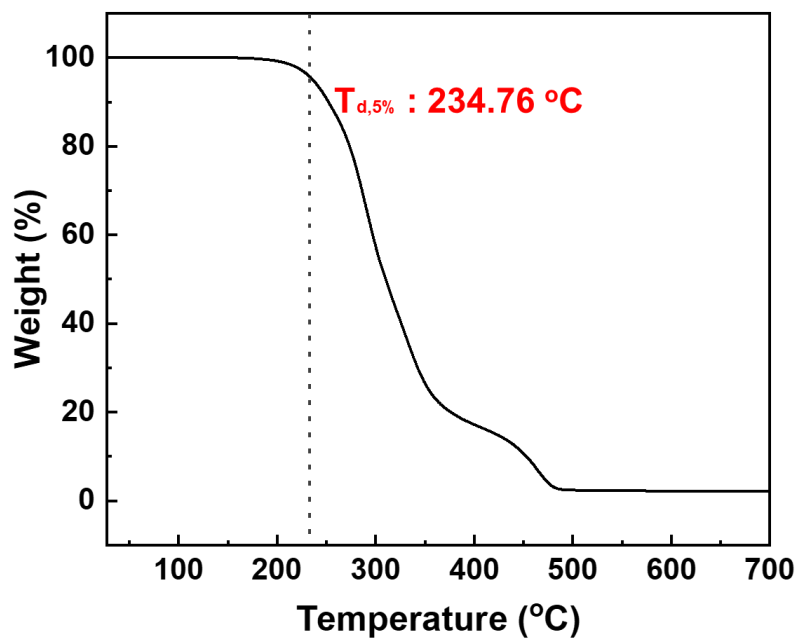
Figure 3.6. TGA curve of MFTU-10.

a

**Dissociative Bond Exchange under
Stoichiometrically Balanced Ratio of Poly(thiourethane)**
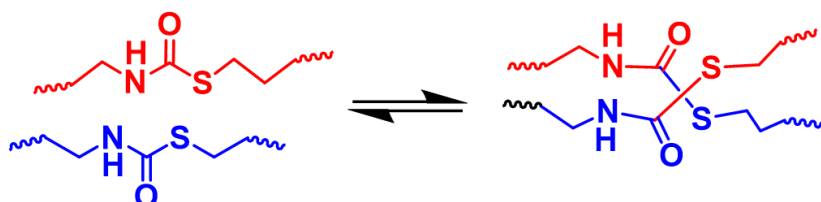
b

**Associative Bond Exchange under
Excess Thiol Ratio of Poly(thiourethane)**
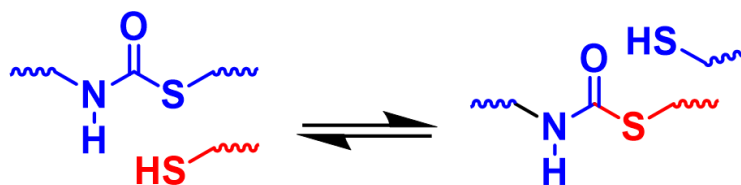
Figure 3.7. Proposed pathways of thiourethane dynamic bond exchange chemistry.
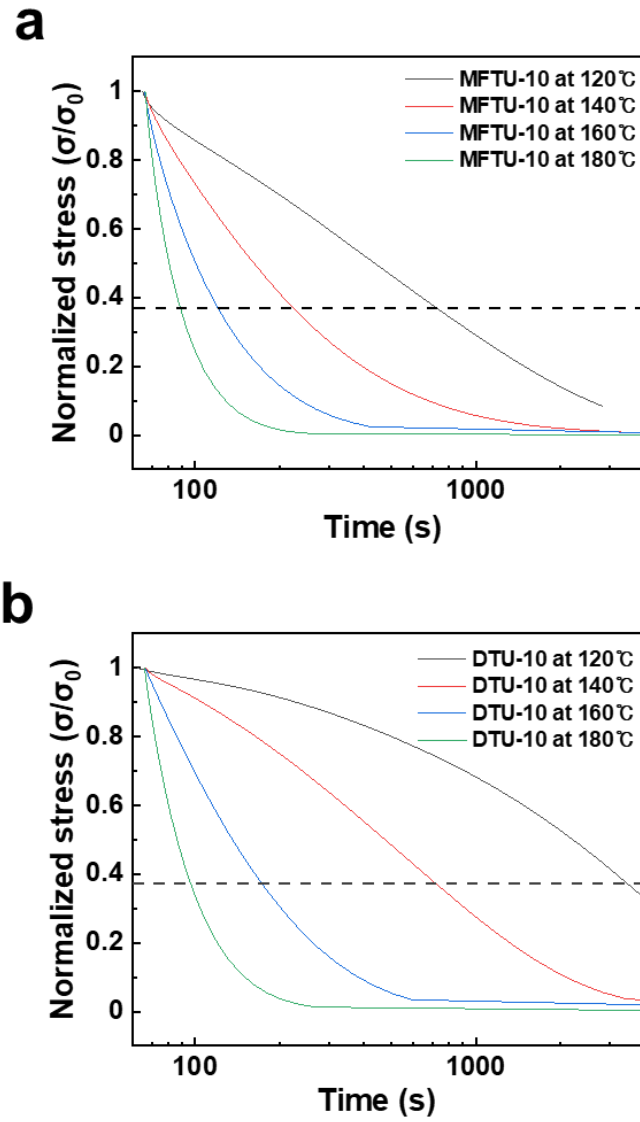
Figure 3.8. Normalized stress-relaxation of (a) MFTU-10 and DTU-10 under different temperatures of at 120, 140, 160, and 180 °C. The dashed line indicates $\sigma/\sigma_0 = e^{-1}$ ($\approx$37 % of the initial stress).
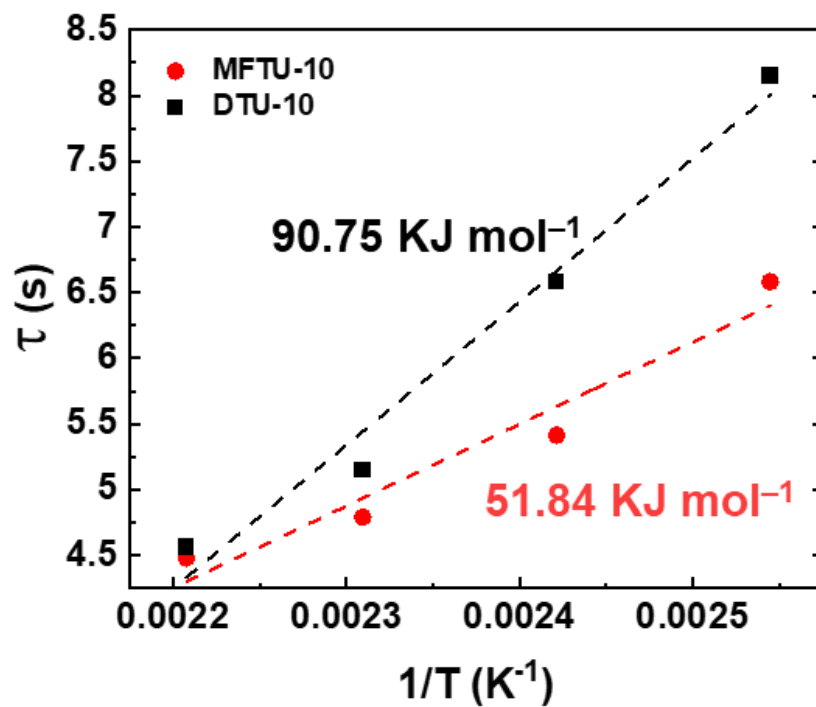
Figure 3.9. Activation energy comparison of MFTU-10 and DTU-10, fitted to Arrhenius equations.
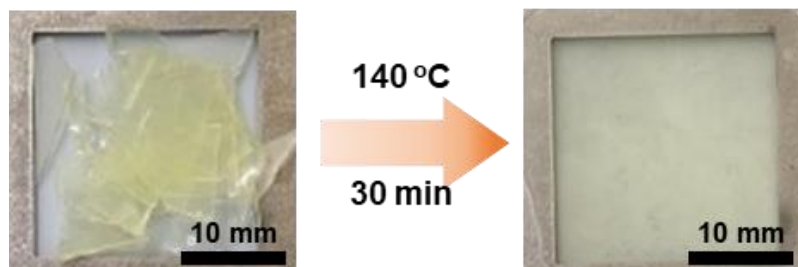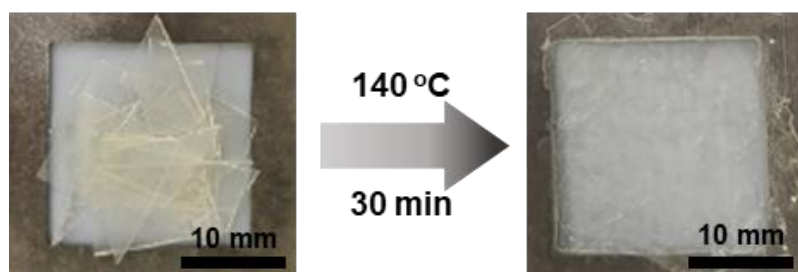
Figure 3.10. Compared images for the reprocessability of MFTU-10 and DTU-10 (scale bars: 10 mm).
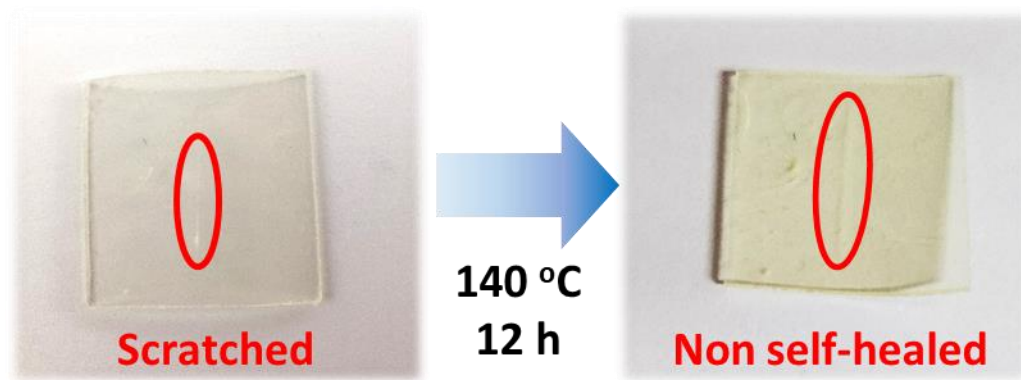
Figure 3.11. Self-healing properties of MFTU-10 (140 °C for 12 h).
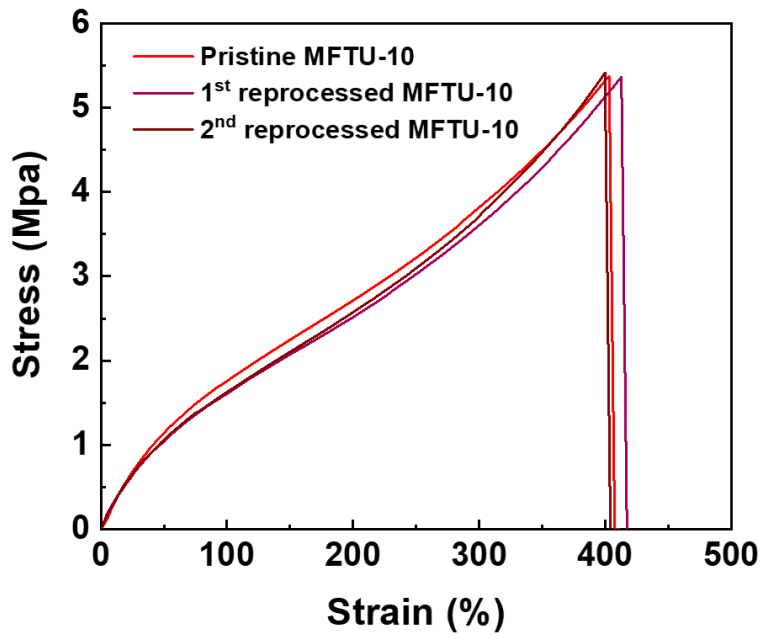
Figure 3.12. Representative stress-strain curves of MFTU-10 after reprocessing (under 10 MPa at 140 °C for 30 min).
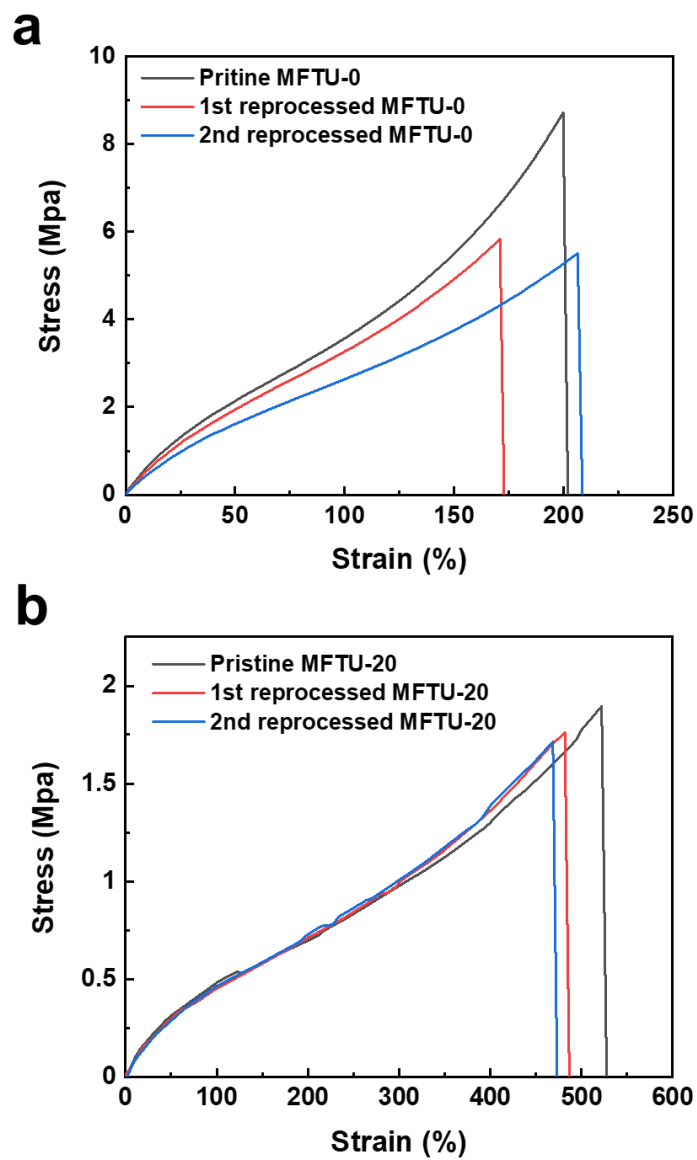
Figure 3.13. Stress-strain curves of reprocessed (a) MFTU-0-P and (b) MFTU-20-P films (pristine, 1st, and 2nd reprocessed).
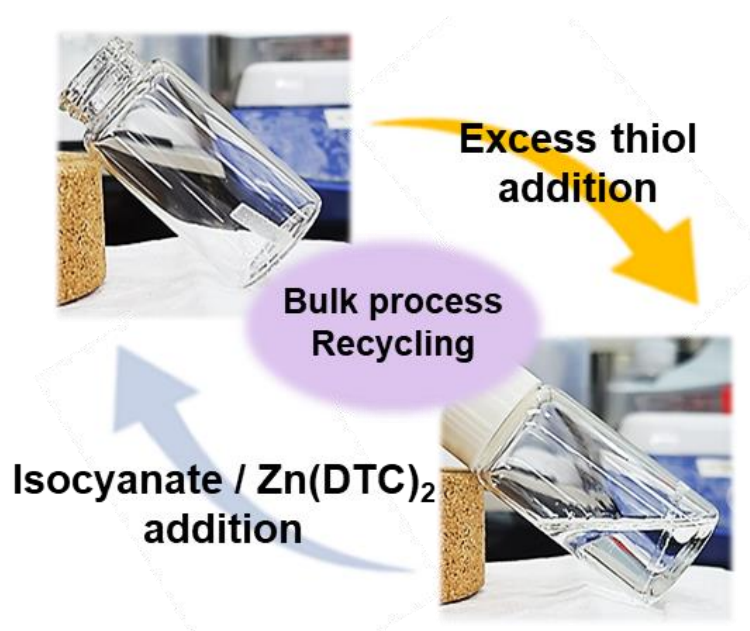
Figure 3.14. Recycling of MFTU-10 via the bulk process with excess thiol addition.
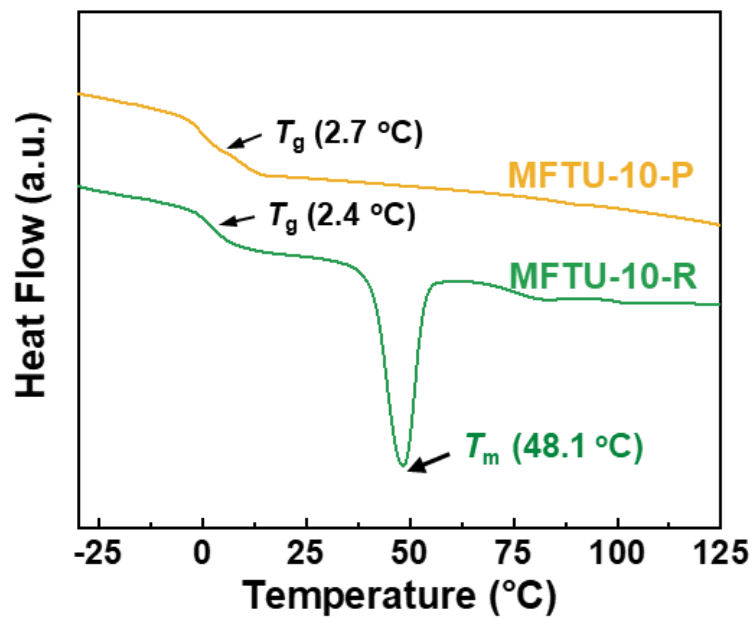
Figure 3.15. DSC thermograms of MFTU-10-R and MFTU-10-P.
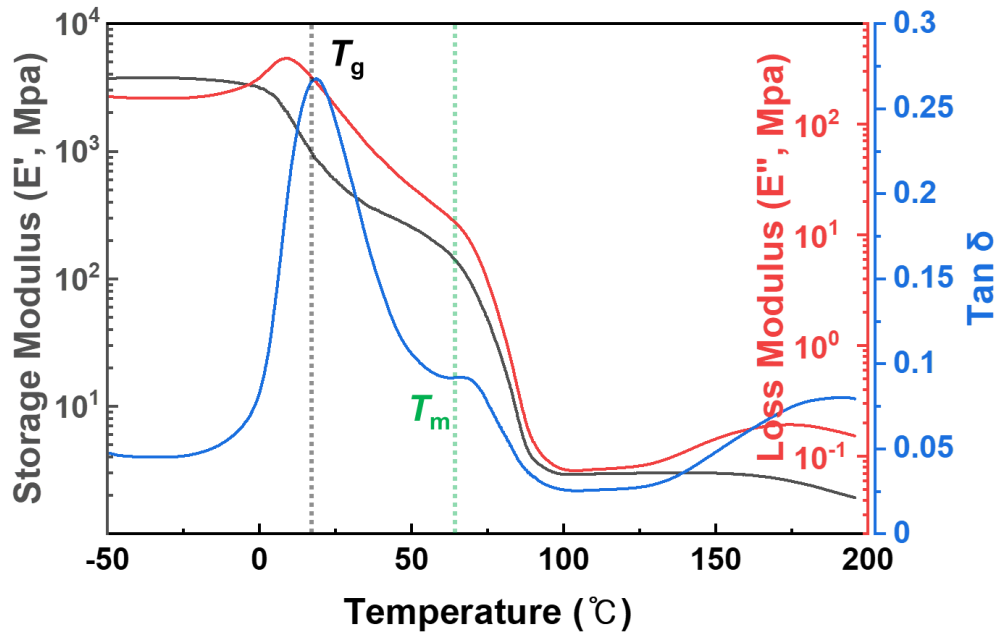
Figure 3.16. DMA curve of MFTU-10 at a constant frequency of 1 Hz and a heating rate of 5 °C min^{-1}, and dynamic strain of 1 %.
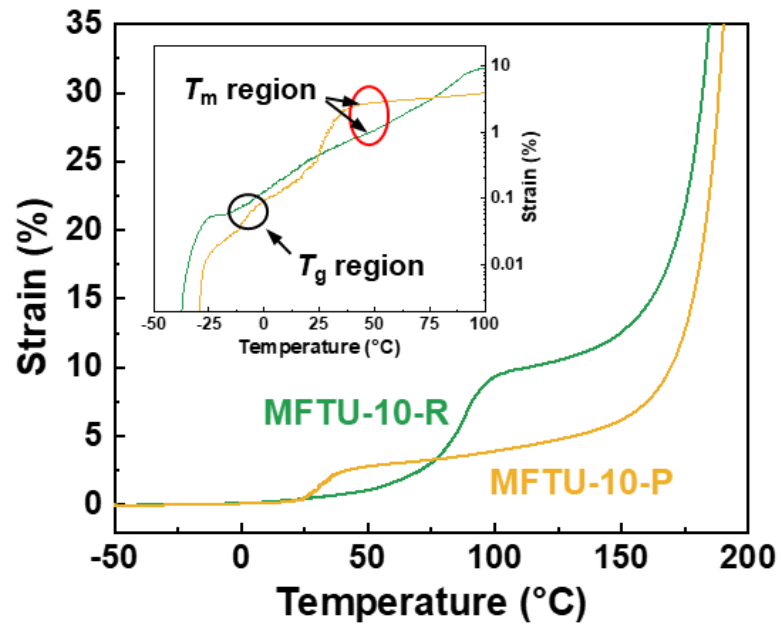
Figure 3.17. Non-isothermal creep test of MFTU-10 by temperature sweep.
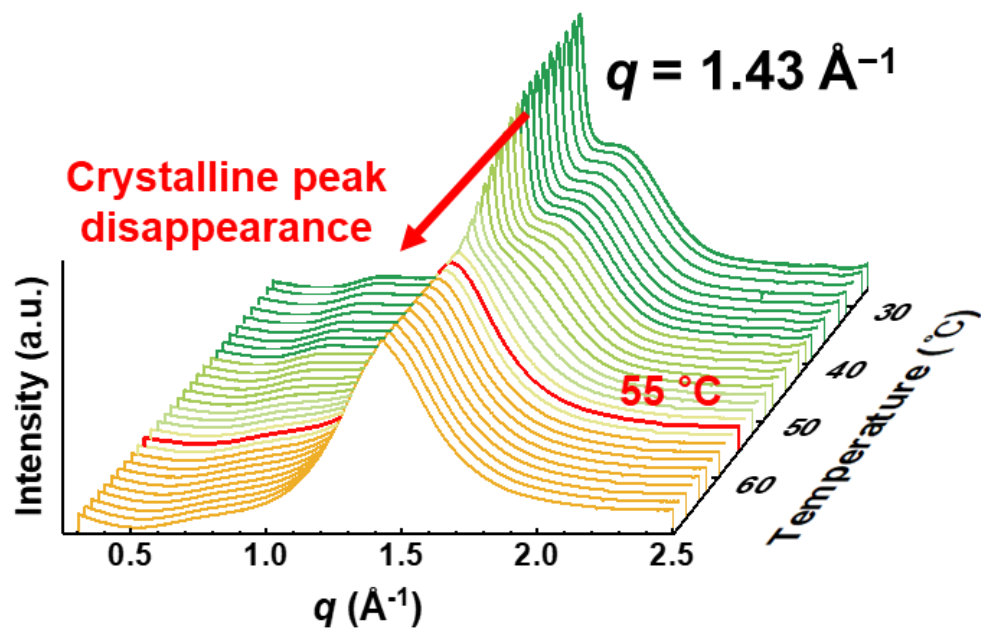
Figure 3.18. Baseline-subtracted *in-situ* 1D WAXS profiles of MFTU-10.
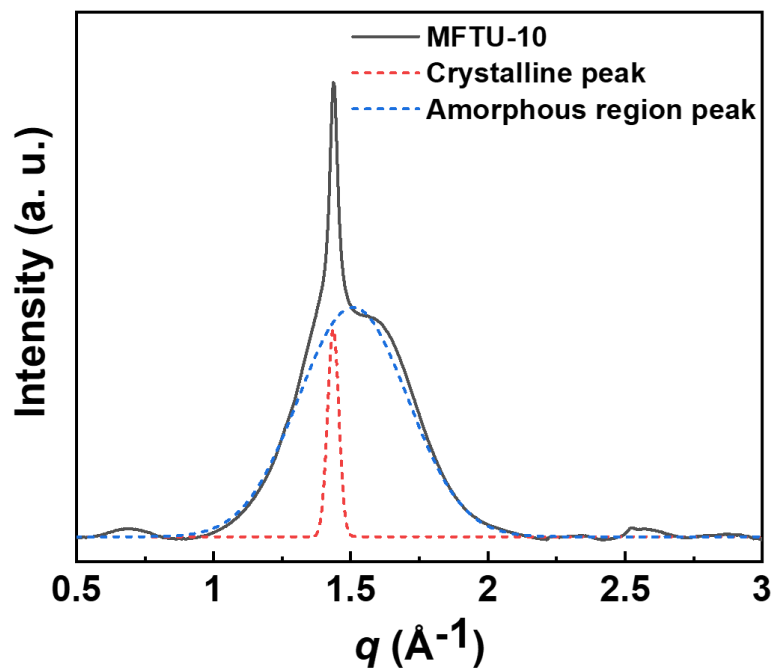
Figure 3.19. Baseline-subtracted 1D WAXS profile of MFTU-10 at 26.8 °C. The solid lines represent measured data, and the dashed lines represent deconvoluted peaks using Gaussian functions.
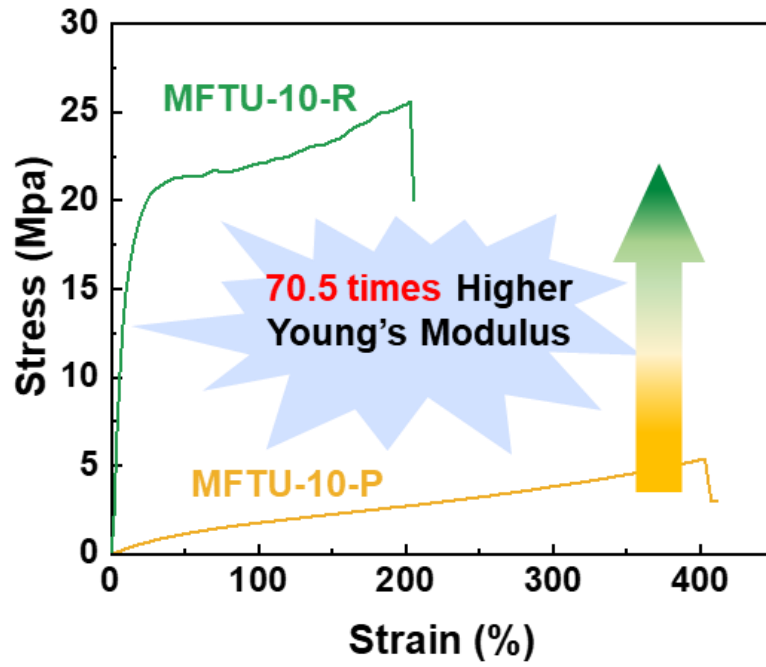
Figure 3.20. Respective stress-strain curves of MFTU-10-R and MFTU-10-P.
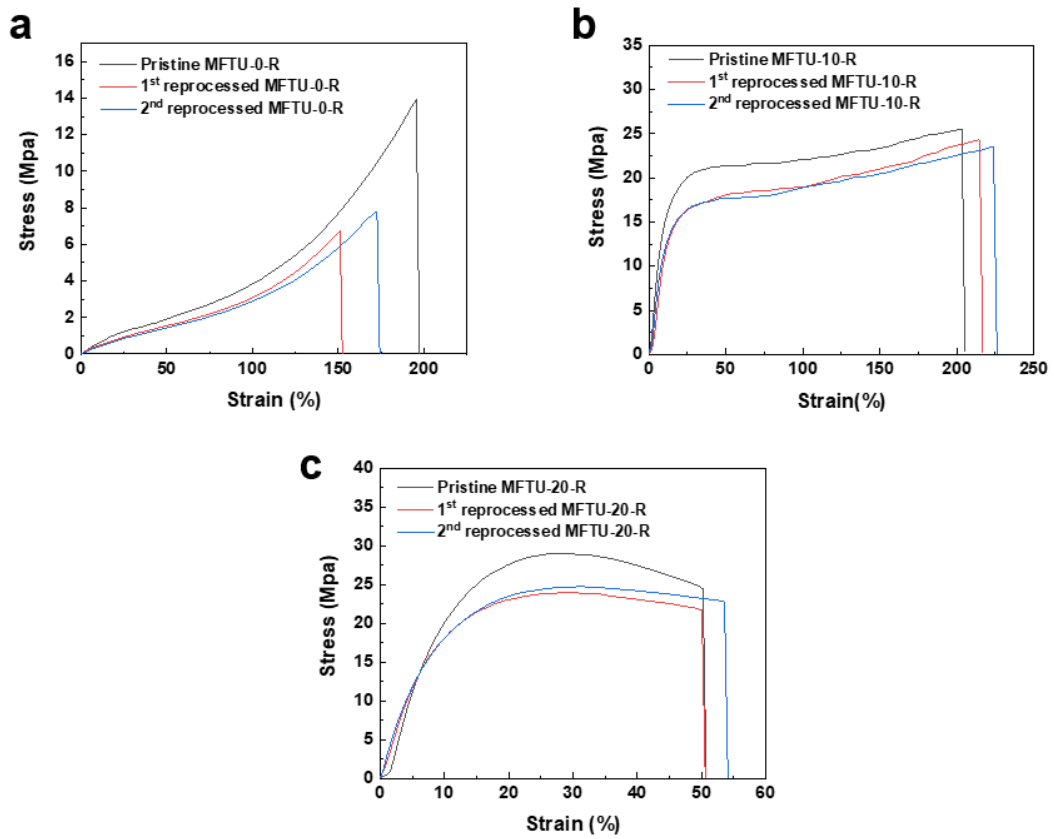
Figure 3.21. The respective stress-strain curves of (a) MFTU-0-R, (b) MFTU-10-R, and (c) MFTU-20-R with programmed as rigid states after reprocessed (pristine, 1st, and 2nd reprocessed).
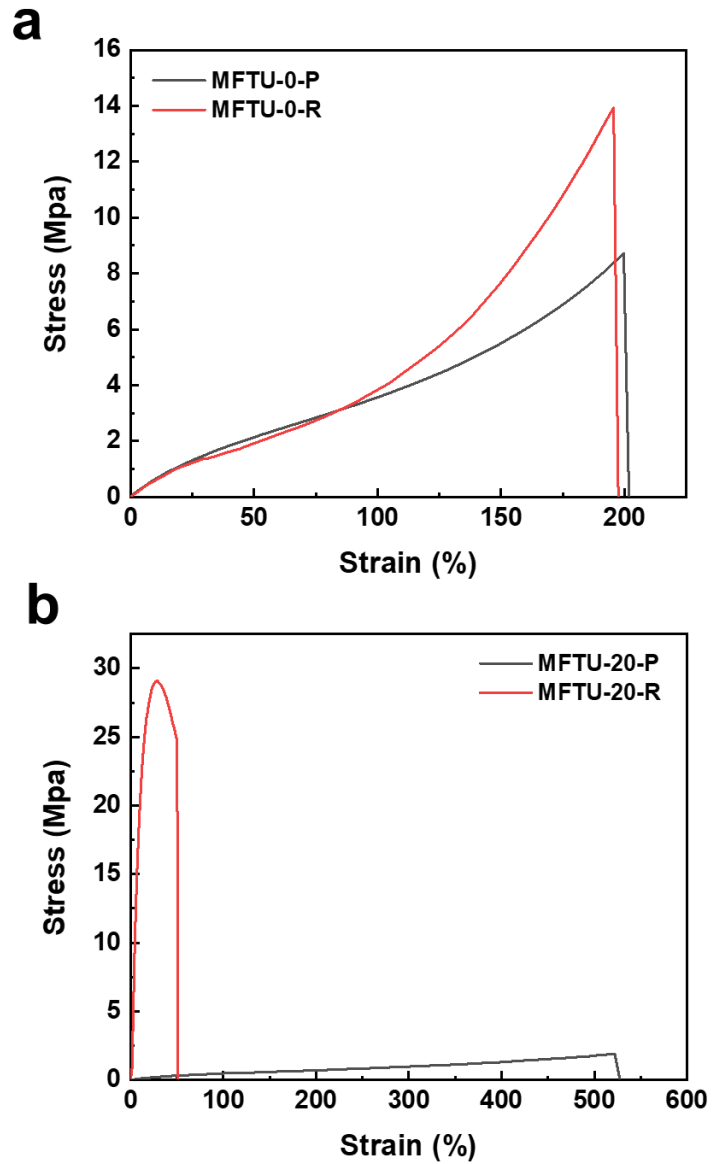
Figure 3.22. The stress-strain curves of (a) MFTU and (b) MFTU-20 according to stiffness programming after reprocessed, respectively.
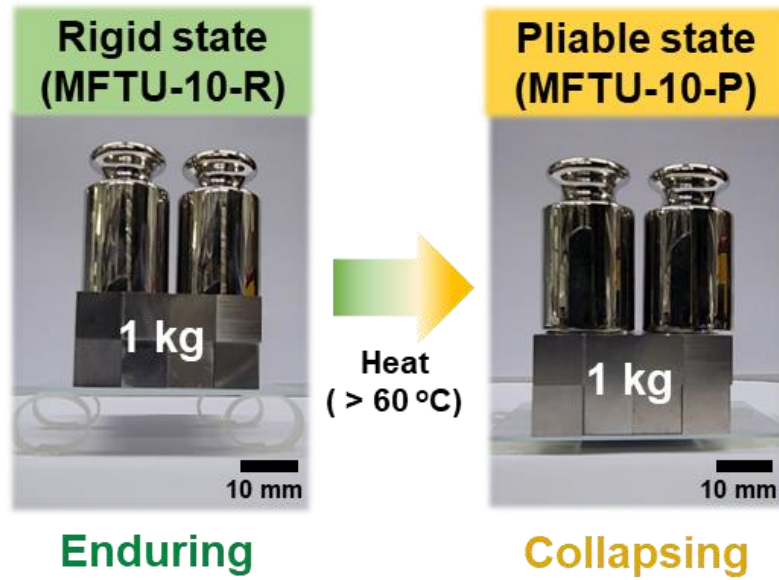
Figure 3.23. Demonstration of 1 kg weight support test by stiffness states of four wheel-shape MFTU-10s.
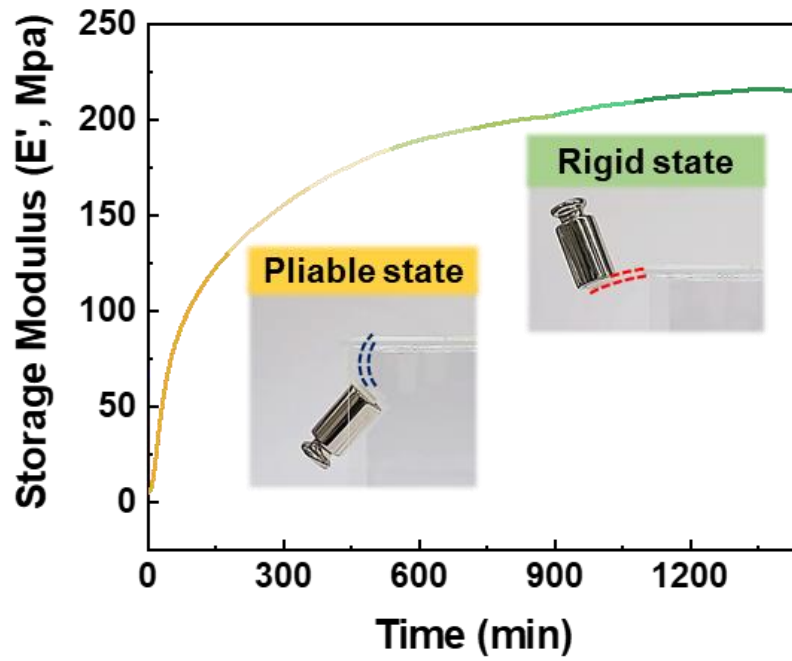
Figure 3.24. *In-situ* measurement of storage modulus (*E'*) of MFTU-10-P as a function of time.
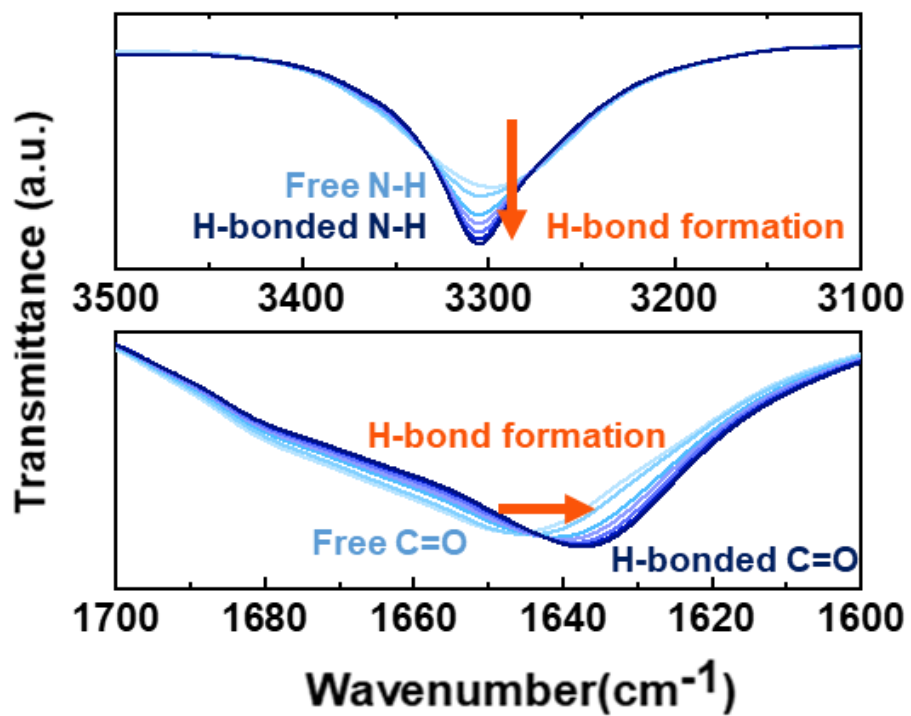
Figure 3.25. Real-time FT-IR spectra of the H-bonds of MFTU-10 cooled down to RT after heating.
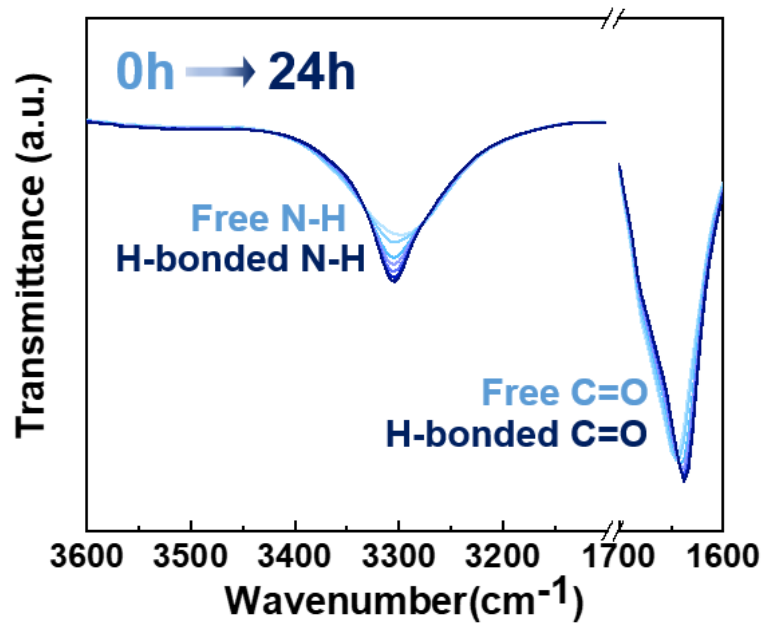
Figure 3.26. Real-time FT-IR spectra for the hydrogen bond of MFTU-10 cooled down to RT after heating.
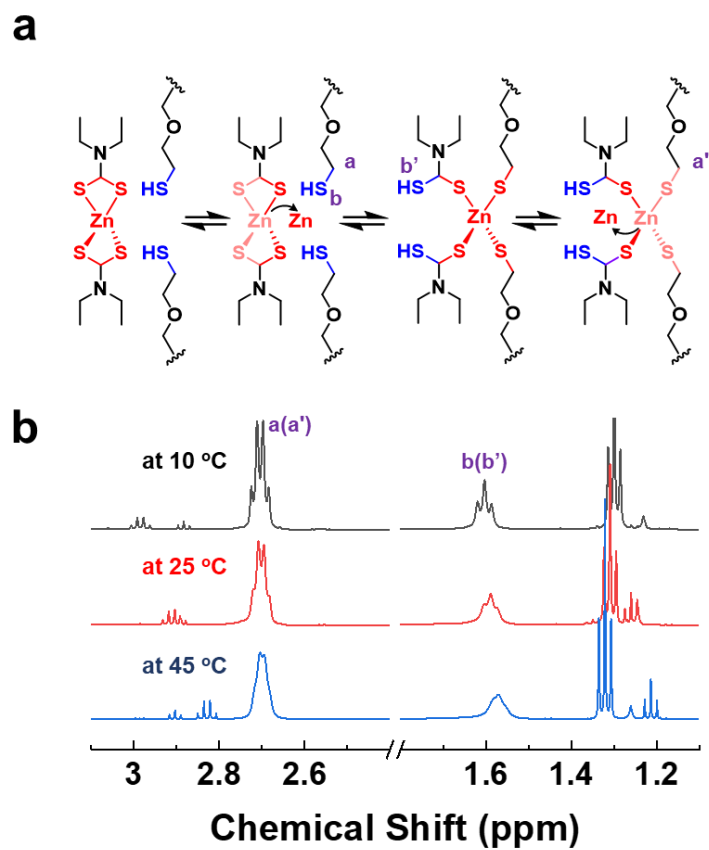
Figure 3.27. (a) Supposed stereochemical structures for DODT and Zn(DTC)$_2$ mixture. (b) *In-situ* ^{1}H NMR spectra of Zn(DTC)$_2$-based modeling compound at variable temperatures of 10°C, 25 °C, and 45 °C, respectively.
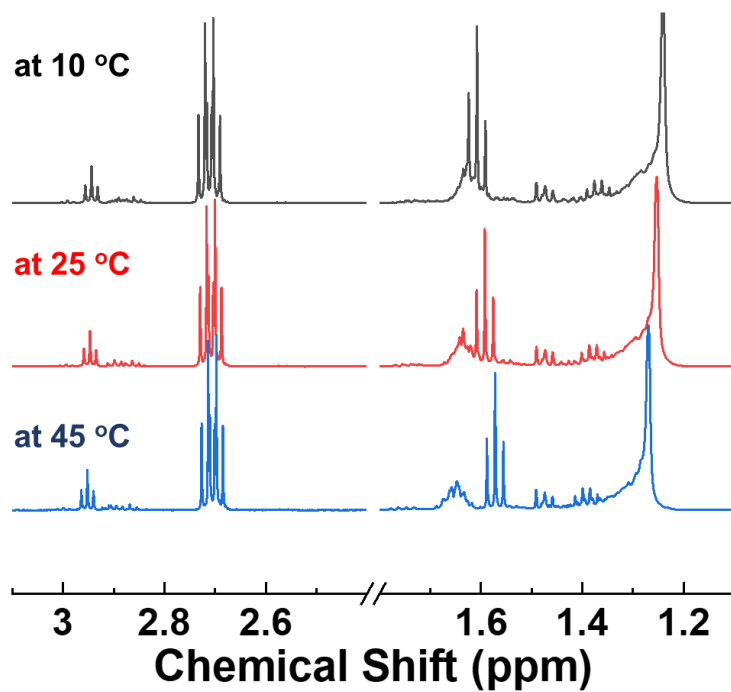
Figure 3.28. *In-situ* ^{1}H NMR spectra of DBTDL-based modeling compound at variable temperatures of 10℃, 25 ℃, and 45 ℃, respectively.
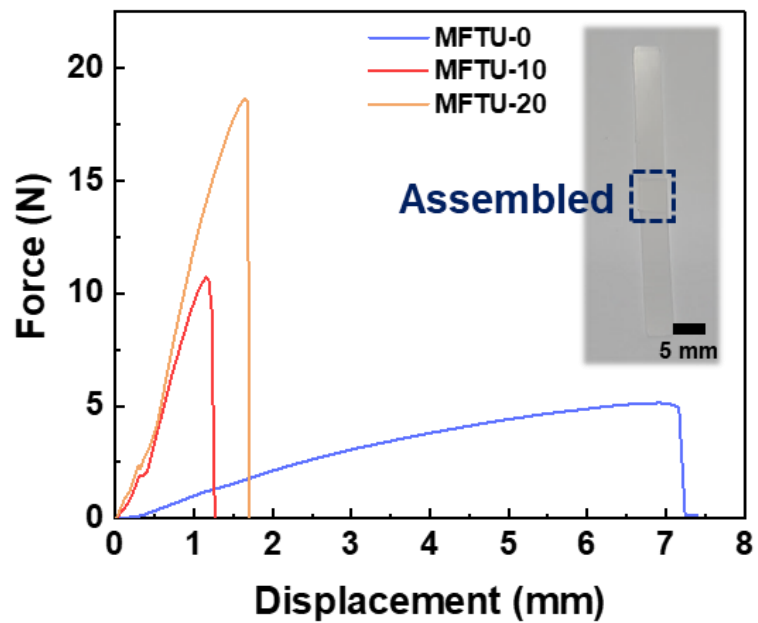
Figure 3.29. Respective stress-strain curves of assembled MFTU films by different excess thiol ratios.
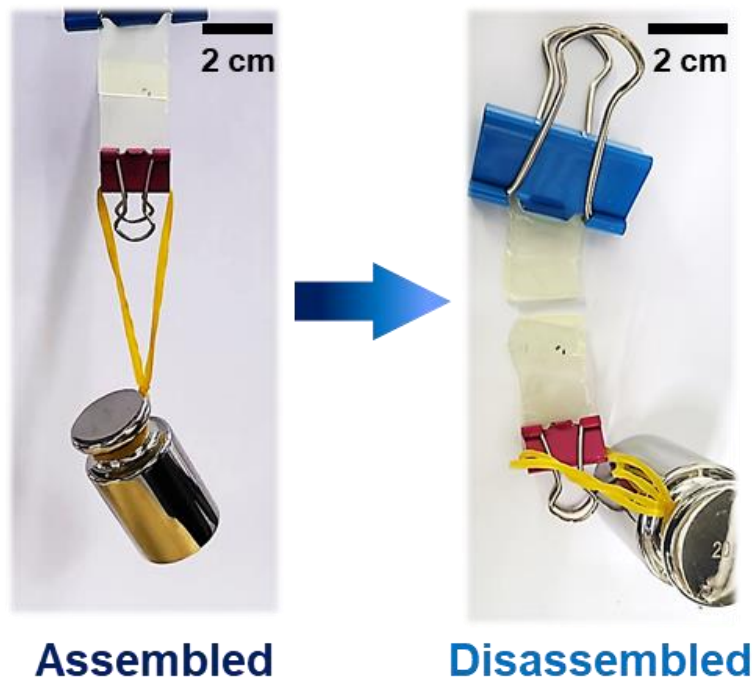
Figure 3.30. Images before and after heat application for 60 °C to an assembled MFTU-10 film capable of withstanding a weight of 200 g.
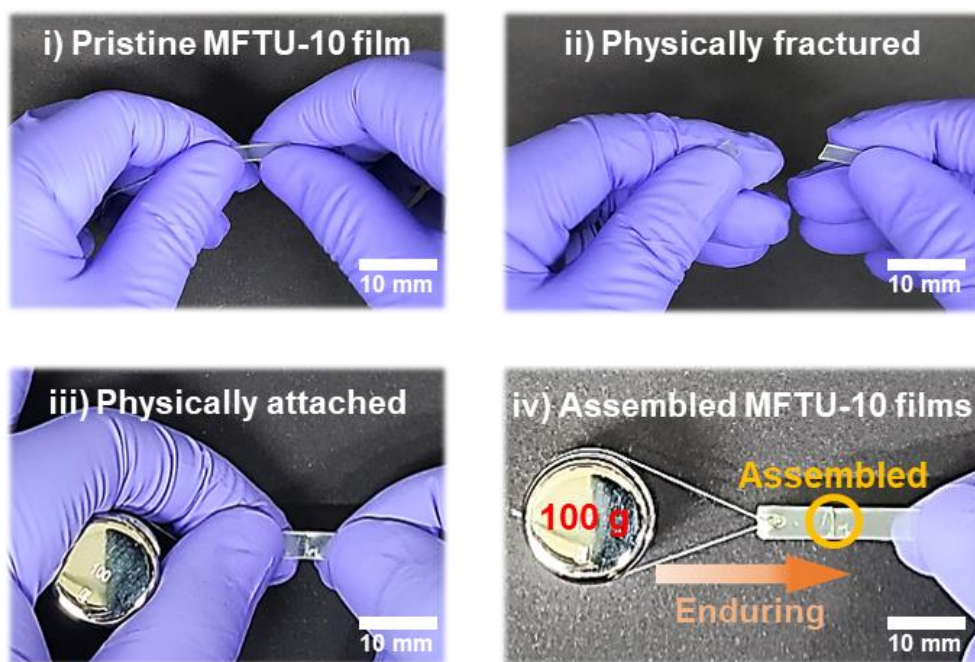
Figure 3.31. Images of the assembly process of MFTU film after physically fractured.
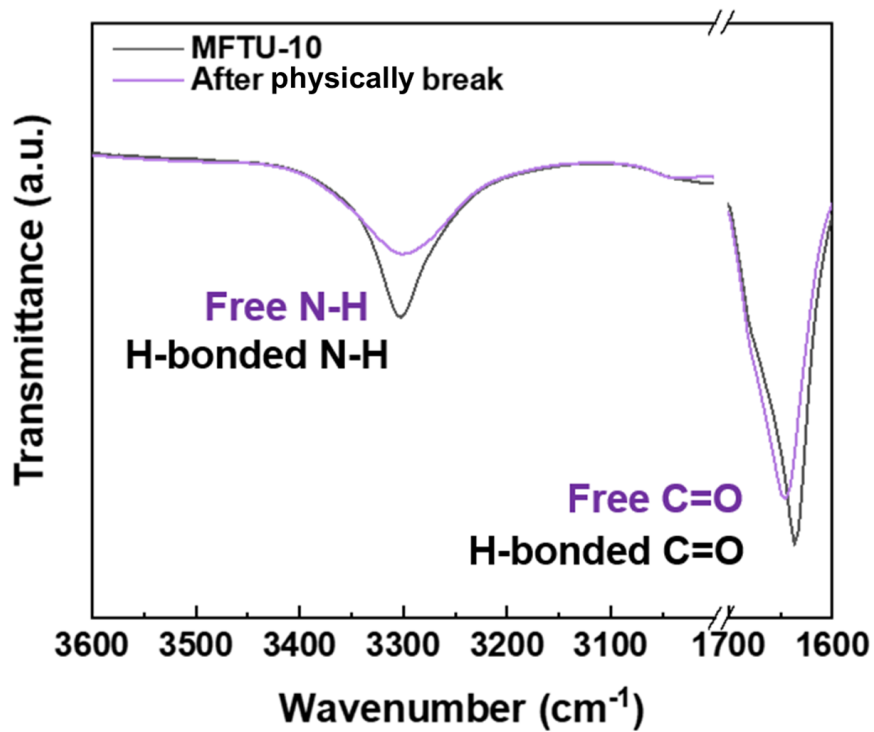
Figure 3.32. Compared FT-IR spectra of hydrogen bonds for pristine and physically fractured surface of MFTU-10.
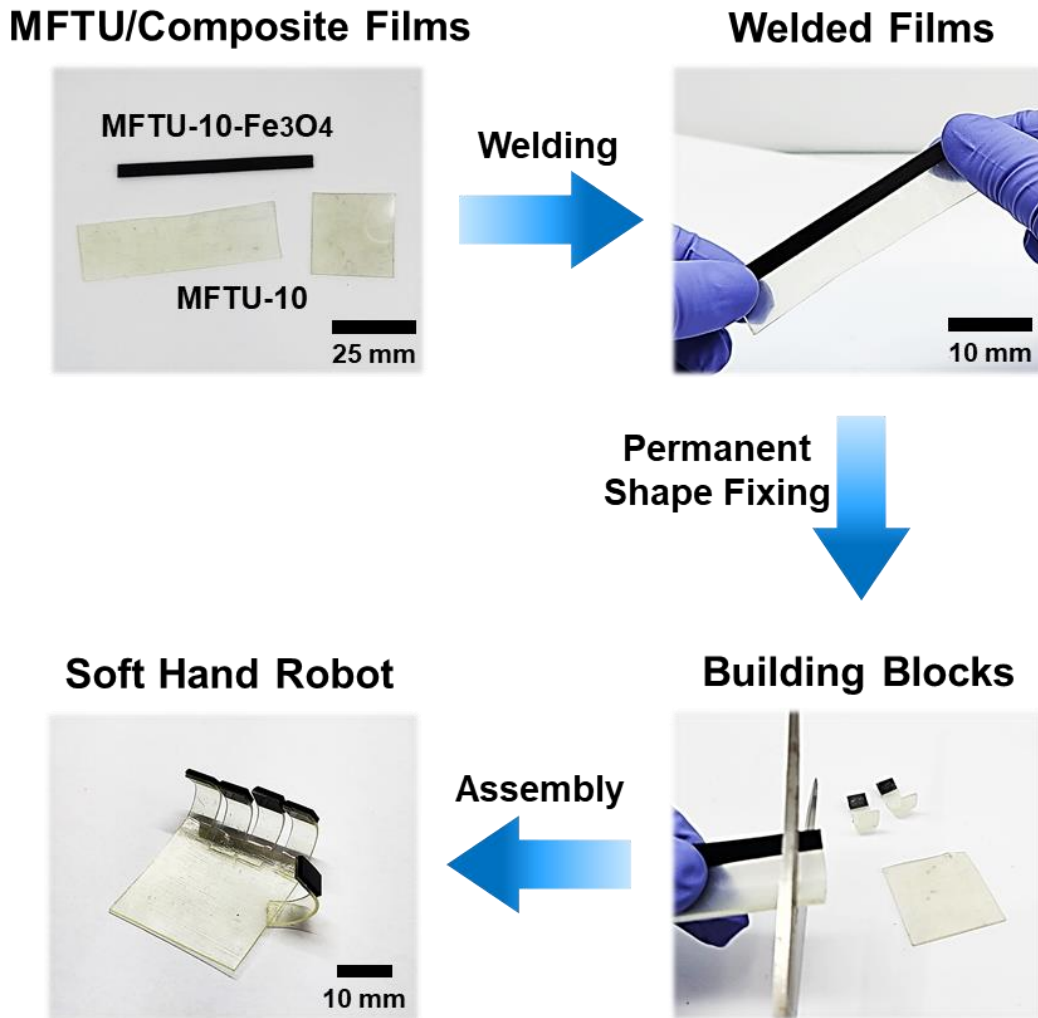
Figure 3.33. Fabrication processes of the soft hand robot through building blocks made after welding MFTU-10 and MFTU-10-Fe_3O_4 composite films with permanent shape fixing.
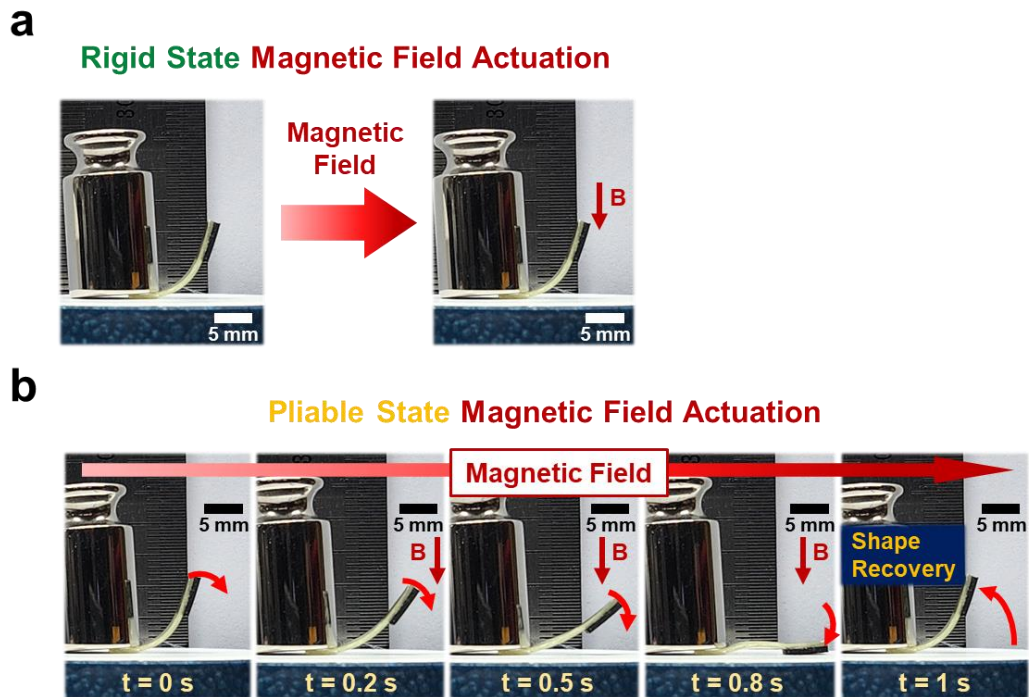
Figure 3.34. Magnetic field actuation test of finger parts of soft hand robot according to (a) rigid and (b) pliable states of the MFTU-10.
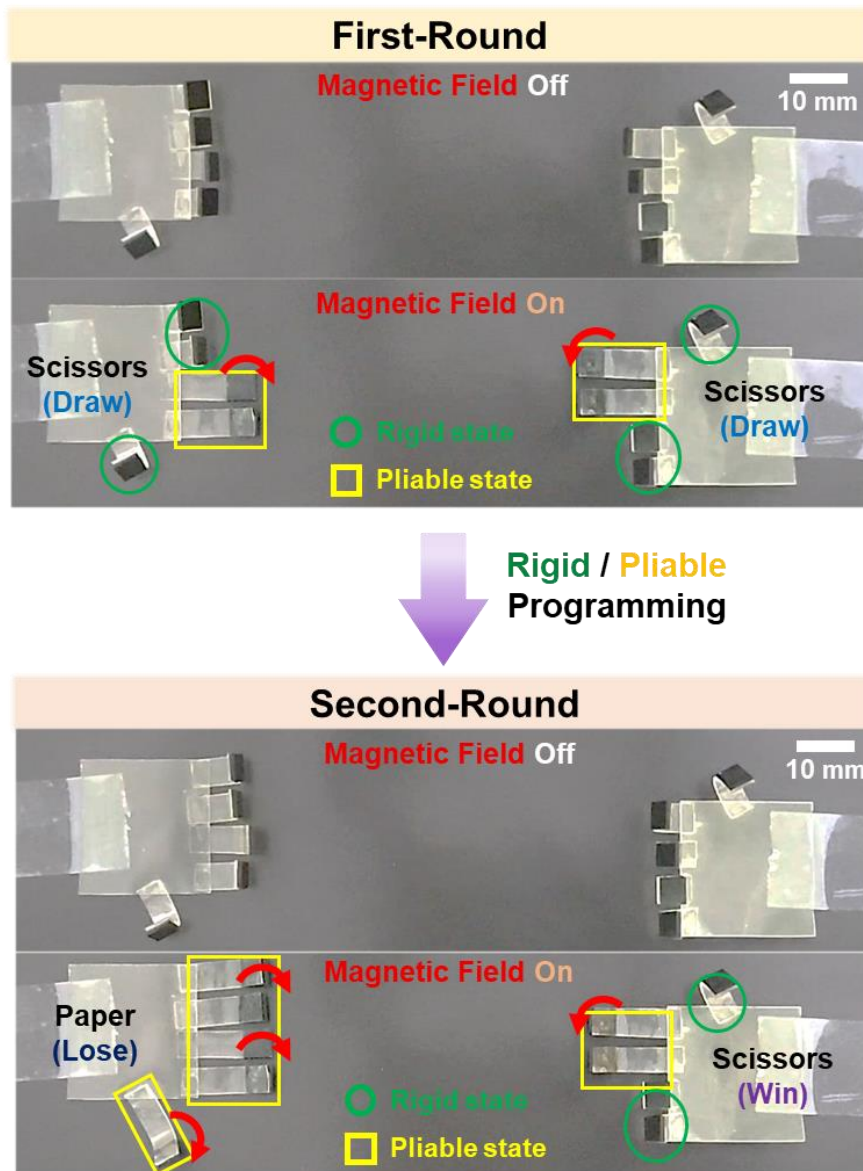
Figure 3.35. Demonstration of the rock scissors paper game using actuation under the magnetic field according to the stiffness state of the MFTU-10.
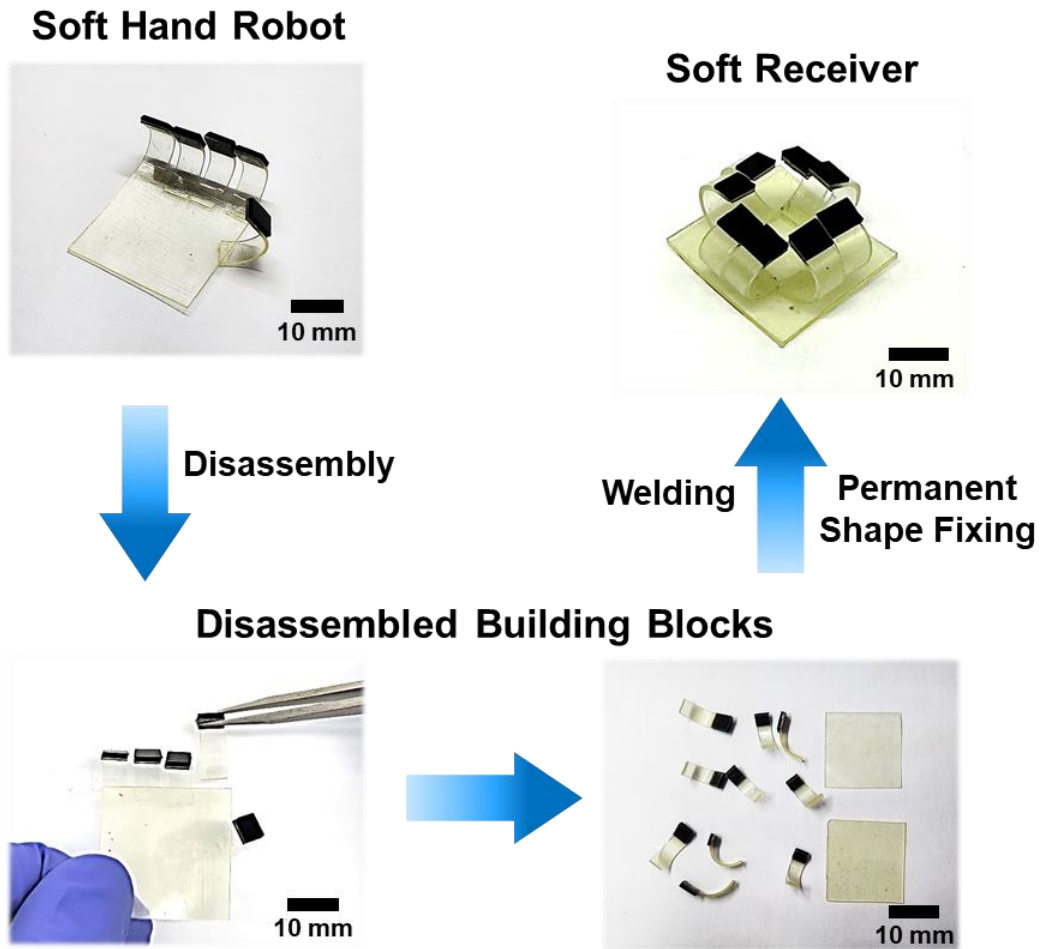
Figure 3.36. Transforming process to a soft receiver from a soft hand robot by disassembling, permanently shape fixing, and welding.
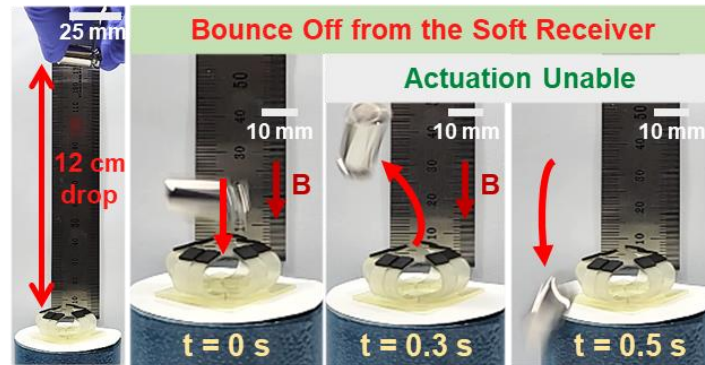
Figure 3.37. Actuation of rigid state soft receiver under magnetic field.

Figure 3.38. Demonstrations of the soft receiver with cargo delivery actuation by programming to a pliable state after gripping by programming from a pliable to a rigid state.
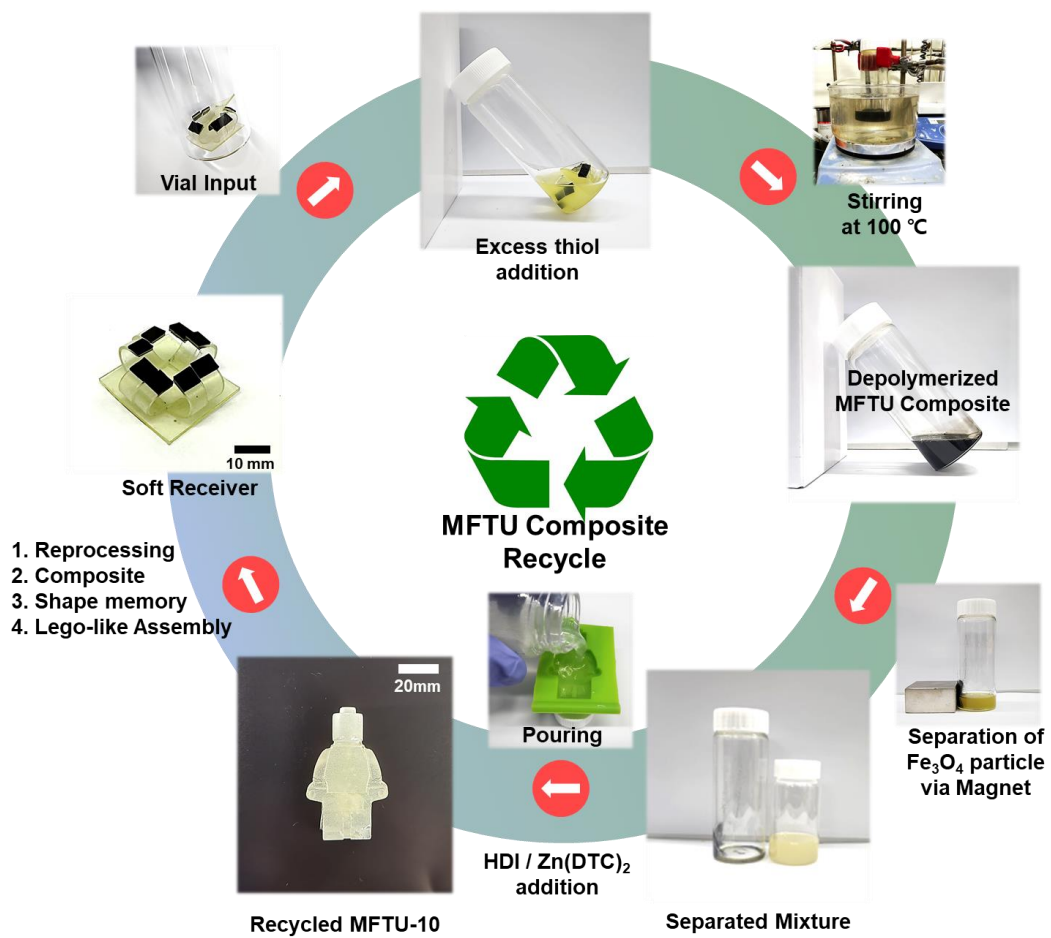
Figure 3.39. Recycling mechanism of the soft receiver via bulk depolymerization and polymerization processes.
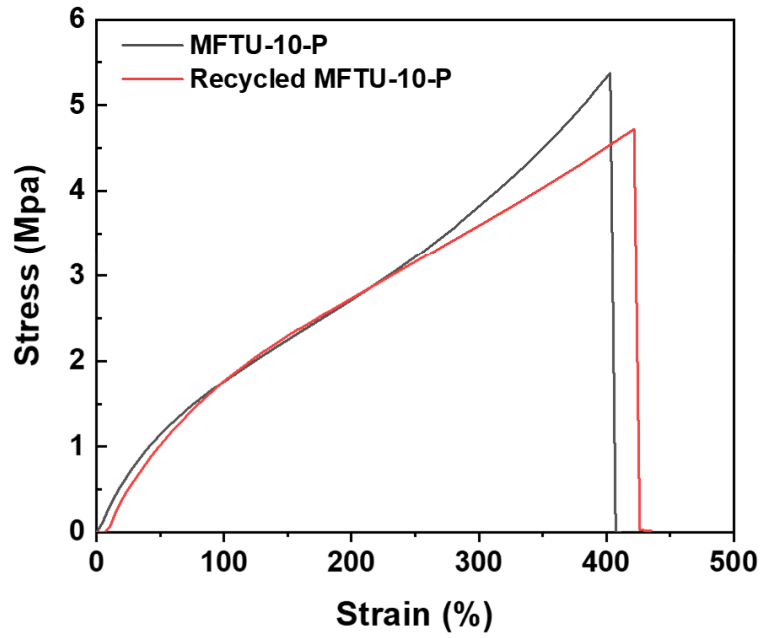
Figure 3.40. Comparison of stress-strain curves for MFTU-10-P and recycled MFTU-10-P.

Chapter 4

A Microphase Separation Strategy for the

Conundrum of Infrared Transparency

and Thermomechanical Property

in Sulfur-Rich Copolymers

4.1. Introduction

Infrared (IR) optical technologies are indispensable in medical (*e.g.*, thermal imaging for COVID-19 screening), transportation (*e.g.*, night vision for autonomous driving), and military (*e.g.*, thermal sensing for missile detection) applications [1,2]. Optically functional materials with high IR transparency and refractive index (*n*), have been identified as critical components for advanced IR optical devices. Inorganic semiconductors and chalcogenide glasses have traditionally been used in thermal imaging applications, owing to their low transmission losses in the IR spectrum ranging from 1–12 µm and high *n* values exceeding 2.0 [2]. However, these materials are intrinsically toxic, brittle, and difficult to process, resulting in high fabrication costs [3,4]. Although inexpensive and readily processable polymeric materials have been explored as alternatives, IR optical applications of polymeric materials still remain challenging due to their high IR absorptions originating from carbon- and hydrogen-rich chains and limited *n* values ranging from 1.6–1.8 originating from low molar refractions [5–7]. Following the discovery of inverse vulcanization of elemental sulfur (ES) in 2013 [8], Pyun et al. pioneered the studies on inverse vulcanized copolymers for IR optical applications [9–11]. Initial chemistry used 1,3-diisopropenylbenzene (DIB) to stabilize polysulfide chains and named poly(sulfur-*random*-DIB)s, (poly(S-*r*-

DIB)s). Such materials exhibited excellent mid-wave infrared (MWIR) transparency and high refractive index values ($n > 1.8$, in the visible to near IR light spectrum range) by the high sulfur content (60–80 wt %), along with good processability and self-healability through dynamic S–S bonds [12–14]. Based on the inverse vulcanization technique, follow-up studies have been conducted to further enhance the n values by incorporating selenium atoms [15–17], or to enhance the long-wave infrared (LWIR) transparency by utilizing organometallic tetravinyltin[18] and norbornene-based crosslinkers [19].

The widespread and practical utilization of inverse vulcanized copolymers for IR optical applications is often limited by their poor thermomechanical properties. The incorporation of the high content of S–S bonds (50−90 wt % of sulfur content) into poly(S-r-DIB)s can enhance their IR optical properties; however, a large number of polysulfide chains eventually lower the glass transition temperature (T_g) of the polymers, ranging from −14 to 28 °C [8], making them unsuitable for some practical applications [2]. In an effort to reinforce the thermomechanical properties of inverse vulcanized copolymers, Pyun et al. utilized a 1,3,5-triisopropenylbenzene (TIB) crosslinker to yield highly crosslinked poly(S-r-TIB)s, exhibiting drastically increased T_g (51.2 °C) compared to that of poly(S-r-DIB)s (9.9 °C) at the sulfur content of 70 wt % [20]. However, owing to the low ceiling temperature in radical polymerization, neither DIB nor TIB could form homopolymerized domains

1 6 7

[21,22]. Based on homopolymerization-assisted crosslinking of 1,3-divinylbenzene (DVB), Char and Lim et al. reported that much improved thermal properties (*e.g.*, $T_g \approx 70-80$ °C) could be obtained from poly(S-*r*-DVB)s with 70 wt % of sulfur content via additional hot pressing and curing process after prepolymer formation [23]. More recently, Char and Lim et al. also reported that thermomechanical properties of inverse vulcanized copolymers can be improved by introducing epoxy crosslinked domains [24]. Furthermore, Hasell et al. demonstrated that the use of catalysts, such as zinc diethyldithiocarbamate, could also contribute to the enhancement of T_g of inverse vulcanized copolymers by ≈ 10 °C due to enhanced degree of crosslinking [25,26]. Despite the progress in the synthesis and processing of the inverse vulcanized copolymers, the trade-off relationship between IR optical and thermomechanical properties is still considered an unresolved conundrum. Therefore, the development of a new synthetic strategy is necessary for thermomechanically robust and highly IR-transparent sulfur-rich copolymers [27–31].

Herein, we present an *in-situ* microphase separation strategy for the inverse vulcanization to significantly improve the thermomechanical properties of sulfur-rich copolymers while maintaining both high IR transparency and *n* values. For the inverse vulcanization of ES, we selected 1,3,5-trivinylbenzene (TVB) as a trifunctional organic crosslinker. Unlike the α-methylstyrene moiety in DIB, the

styrene moiety in TVB has a high ceiling temperature of radical polymerization [21,32]. Importantly, the three vinyl groups of TVB can participate in self-crosslinking to form TVB-rich domain and thus microphase separation in addition to the reaction with sulfur radicals (Figure 4.1). The self-crosslinking of aromatic TVB is expected to yield a hard domain with superior thermomechanical properties. Hence, we hypothesized that the hard domain with self-crosslinked TVBs could contribute to the enhancement of overall thermomechanical properties by restricting the soft segmental motions of the polysulfide chains [33], whereas the sulfur-rich domain could still be responsible for the excellent IR optical properties and processability (Figure 4.1) [13,18]. By tailoring the chemical composition of the networks, we have further controlled their thermomechanical properties, consequently achieving a remarkable modulus of $\approx$2.0 GPa at 30 °C and high T_g of 92.6 °C for the sulfur-rich domain, even with 80 wt % sulfur content. Such high sulfur content of poly(S-r-TVB) was also found to lead to excellent mid-wave and long-wave IR transmittance (37.95 %T and 1.96 %T at 3−5 μm and 7−14 μm, respectively, with 1.1 mm-thick film) and high refractive index (n = 1.88 at 829 nm), as well as good processability via a simple hot pressing. To the best of our knowledge, this is the first example of *in-situ* microphase-separated copolymers with a high sulfur content (> 80 wt %), synthesized by one-pot inverse vulcanization, for achieving well-balanced thermomechanical and optical properties.

1 6 9

4.2. Results and Discussion

A series of poly(S_x-r-TVB$_y$)s were synthesized by a solvent-free inverse vulcanization reaction of ES with TVB, where x and y indicate the average weight percentage (wt %) of ES and TVB, respectively. TVB, like other organic crosslinkers with phenyl groups [22], was found to be highly miscible with molten sulfur. After the ES melted and turned into a yellowish liquid in a vial at 160 °C, TVB was added dropwise under vigorous stirring to induce inverse vulcanization. After further stirring for 10 min, the vitrified poly(S-r-TVB) was obtained (Figure 4.2). The poly(S-r-TVB)s in this study were found to be insoluble in organic solvents with high gel fraction (f_g) (Table 4.1), indicating successful inverse vulcanization reaction. Complete consumption of ES and vinyl groups of TVB was confirmed by Fourier transform infrared (FT-IR) spectroscopy and X-ray diffraction (XRD) analysis (Figure 4.3 and 4.4a). When the TVB content (y) in the polymer was below 10 wt % (Figure 4.4b), unreacted residual sulfur was observed. However, when the sulfur content was reduced below 70 wt %, a heterogeneous and incomplete product was obtained due to the accelerated reaction (Figure 4.5). Thus, y was controlled to be in the range of 10–30 wt % (Table 4.1). To confirm self-crosslinking of TVB, solid-state cross-polarization magic angle spinning ^{13}C nuclear magnetic resonance spectroscopy was performed. Characteristic chemical

shifts at around 42 and 125 ppm were observed, which correspond to –CH– and phenyl–CH of the self-crosslinked TVB structure, respectively (Figure 4.6). As shown in Figure 4.5, The chemical shifts of PTVB and poly(S-r-TVB)s were confirmed through ^{13}C CP-MAS solid-state NMR. The chemical shifts at ca. 148, 138, and 125 ppm (–C_{ph}(Self), –C_{ph}(Self), and –$C_{ph}H$(Self), respectively) were observed in poly(S-r-TVB)s, which correspond to phenyl C resonances of self-crosslinked TVB-rich domain. In addition, the shoulder peak at ca. 42 ppm corresponds to the –CH– of the self-crosslinked TVB-rich domain. On the other hand, the chemical shifts at ca. 142 and 128 ppm (–C_{ph}(Co) and –$C_{ph}H$(Co)) were observed, which correspond to phenyl C resonance of the polysulfide-rich domain in poly(S-r-TVB) copolymers. C–S bond formations ((–CH–(Co) and (–CH_2–(Co)) in copolymer structure are verified at ca. 50 ppm. Since all TVBs are difficult to crosslink in the form of entirely self-crosslinked TVBs due to steric hindrance, residual TVB is observed at chemical shifts of ca. 162 and 114 ppm. This clearly attests the self-crosslinking of TVBs in addition to the C–S bond formation during the one-pot inverse vulcanization process.

Motivated by the presence of self-crosslinked TVBs, we further investigated the microphase separation in poly(S-r-TVB)s by atomic force microscopy (AFM) and differential scanning calorimetry (DSC). As shown in Figure 4.7 and 4.8a, AFM revealed microphase separation of the poly(S-r-TVB)s with 10–20 wt % of

TVB, clearly demonstrating relatively hard (*i.e.*, bright-colored) and soft (*i.e.*, dark-colored) domains [34]. In the case of poly(S-*r*-TVB)s with 25–30 wt % of TVB, phase images have no distinct separation. As the surfaces of all samples are topologically flat with root-mean-square height deviations less than 0.4 nm (Figure 4.8b), topological roughness effects can be excluded from the microphase separation in the phase images. Microphase separation of poly(S-*r*-TVB) was confirmed through tapping mode AFM analysis. Samples of poly(S-*r*-TVB)s with 10–30 wt% of TVB were prepared with flat fragments by cracking bulk poly(S-*r*-TVB)s in liquid nitrogen. In the phase-contrast images, microphase-separated morphologies with discontinuous domains surrounded in the continuous matrix are observed for poly(S$_{80}$-*r*-TVB$_{20}$), poly(S$_{85}$-*r*-TVB$_{15}$), and poly(S$_{90}$-*r*-TVB$_{10}$). The bright-coloured part is the self-crosslinked TVB-rich domain and the dark-coloured part is the polysulfide-rich domain, confirming distinct phase separation of poly(S$_{80}$-*r*-TVB$_{20}$), poly(S$_{85}$-*r*-TVB$_{15}$), and poly(S$_{90}$-*r*-TVB$_{10}$). On the other hand, no distinction is observed in poly(S$_{70}$-*r*-TVB$_{30}$) and poly(S$_{75}$-*r*-TVB$_{25}$). As microphase-separated polymers exhibit double T_g phenomena, DSC was performed on the poly(S-*r*-TVB)s to investigate microphase separation (Figure 4.9). As expected, the microphase-separated poly(S-*r*-TVB)s with 10–20 wt % of TVB exhibited distinctively separated two T_g values [35], where the first T_g, corresponding to the sulfur-rich domain, drastically increases from 19.4 to 92.6 °C.

It is because the soft segmental motion is restricted as the content of glassy self-crosslinked TVBs increases. With increasing TVB content, the second T_g from the self-crosslinked TVB-rich domain also increases slightly from 137.8 to 139.8 °C. From poly(S_{75}-r-TVB_{25}), two T_gs are eventually merged into a single T_g of 148.6 °C, which is consistent with the AFM image without any distinct phase separation. Poly(S_{70}-r-TVB_{30}) exhibits a T_g value of 173.1 °C, to the best of our knowledge, which is a record high among the inverse vulcanized sulfur-rich copolymers with 70 wt % sulfur content.

To further investigate the microphase separation, detailed morphological characterization of the poly(S-r-TVB)s was also performed using small-, medium-, and wide-angle X-ray scattering (SAXS, MAXS, and WAXS) (Figure 4.10). In the SAXS region, all the poly(S-r-TVB)s exhibit strong upturns with a power-law exponent of 4 at $q < 0.03$ Å^{-1}, where q is the scattering vector, indicating phase-separated heterogeneous structures with sharp interfaces and large fractal agglomerates [36]. As shown in Figure 4.11, the normalized dimensionless Kratky plot of poly(S_{80}-r-TVB_{20}) displays a bell-shaped curve following Guinier's law rather than the asymptotic Debye model. Furthermore, at $q_{max}R_g = \sqrt{3}$, the maximum $(qR_g)^2 I(q)/I(0)$ (where $I(0)$ and R_g is the scattering intensity of zero q and the radius of gyration, respectively) value of 1.110 indicates that it is close to the ideal spherical case, which corresponds to the AFM micrographs [37]. In the

WAXS region, two separated peaks are observed when peak fitting is conducted using Gaussian functions after the baseline subtraction (Figure 4.12a). One peak (q_s) at 1.32 Å^{-1} arises from the self-crosslinked TVB-rich domain, as confirmed by the WAXS profile of self-polymerized TVB (Figure 4.12b). The other peak (q_c) at 1.71 Å^{-1} originates from the phenyl groups of sulfur-rich copolymer network domain. The calculated characteristic distances from q_s and q_c are 4.76 and 3.67 Å, attributed to T-shaped and parallel-displaced configurations of phenyl groups in poly(S-r-TVB)s, respectively [38,39]. In the self-crosslinked TVB-rich domain (*i.e.*, high concentration of phenyl groups), the phenyl groups that form the π–π interaction are packed in an upright state and exhibit a T-shaped configuration [40]. However, in the polysulfide-rich domain (*i.e.*, low concentration of phenyl groups), reclining of the phenyl groups is favorable, thus leading to parallel-displacement configuration [40]. When the TVB content in the microphase-separated poly(S-r-TVB)s is 10 to 20%, the difference in peak area between q_s and q_c decreases gradually with increasing TVB content, but still appears as large as 44 to 86% (Figure 4.13). When the TVB contents increase, the area ratio of q_s peak (A_s) rises from 7 to 32 %. Meanwhile, the peak area difference no longer decreases and remains to be 31 to 36% for poly(S75-r-TVB25) and poly(S70-r-TVB30) that present no distinct phase separation. This result is also consistent with the AFM phase images and thermal transition behavior of poly(S-r-TVB)s.

The thermogravimetric analysis clearly demonstrates that the thermal stability of poly(S-*r*-TVB)s is improved with increasing TVB content (Table 4.1 and Figure 4.14). As shown in Table S1 and Figure S8, the thermal decomposition of poly(S-*r*-TVB)s at a range from $T = 196.14$ to 248.50 °C was confirmed through TGA analysis. The TGA thermogram slopes of poly(S-*r*-TVB) are changed by polysulfide decomposition (ca. 253–258 °C) and self-crosslinked TVB decomposition (ca. 481–498 °C), according to the phase separation. Poly(S$_{90}$-*r*-TVB$_{10}$), which has the lowest TVB content, has a relatively small region of the self-crosslinked TVB-rich domain, inducing dramatic weight loss. On the other hand, as the TVB ratio in poly(S-*r*-TVB) increases, the self-crosslinked TVB-rich domain enlarges, resulting in relatively smaller weight loss. PTVB shows high thermal stability with $T_{d,5\%}$ of 468.75 °C. All the poly(S-*r*-TVB)s exhibit insignificant weight loss until 175 °C, and sulfur-rich copolymers with 10–20 wt % of TVB can be readily hot-pressed into films at 165–175 °C with the pressure of 10 MPa (Figure 4.15). The exchange of dynamic S–S bonds in sulfur-rich copolymers at elevated temperatures should contribute to the rearrangement of network structures, facilitating the melt processing [13,14]. Meanwhile, the same hot pressing process could not be applied to the poly(S$_{75}$-*r*-TVB$_{25}$) and poly(S$_{70}$-*r*-TVB$_{30}$) with a single T_g ranging from 148.6 to 173.1 °C, which is attributed to a large amount of highly crosslinked TVB domains as well as limited amount of dynamic S–S bonds for

effective network rearrangement.

Considering the thermal processability, we have chosen the poly(S-*r*-TVB)s with 10–20 wt% of TVB to further explore their thermomechanical and rheological behaviors as well as optical properties after reprocessing the bulk solids into films via hot pressing. Dynamic mechanical analysis (DMA) was performed on the poly(S-*r*-TVB)s from the glass transition to the rubbery plateau region (*i.e.*, 30–140 °C) (Figure 4.16). The T_g from the maximum tan δ shows a drastic enhancement from 47.1 to 91.6 °C, according to the increased TVB contents from 10 to 20 wt %. The increased T_g results in a tremendous reinforcement of mechanical stiffness. The storage modulus (E') increases from 0.30 GPa for poly(S$_{90}$-*r*-TVB$_{10}$) to 1.96 GPa for poly(S$_{80}$-*r*-TVB$_{20}$) at 30 °C, originating from the glassy nature of the poly(S$_{80}$-*r*-TVB$_{20}$). Using Boltzmann time-temperature superposition (TTS) at T_{ref} of 130 °C, viscoelastic master curves were constructed from frequency sweeps in the linear viscoelasticity (LVE) region (Figure 4.17 and 4.18). For quantitative comparison, we extracted the plateau modulus (G_N^0) by reporting the G' (shear storage modulus) at a frequency for the minimum tan δ from the viscoelastic master curve. In Figure 4.19 and Table 4.2, the calculated crosslinking density (v_e) increases from 1294.9 to 2273.3 mol m^{-3} as a result of increased TVB content from 10 to 20 wt %. Following the trend of v_e variation, the G_N^0 increases from 2.51 to 5.28 MPa with a frequency shift for the minimum tan δ from 465.0 to 3.0 rad s^{-1}. In addition, the

zero-shear viscosity (η^0) can be estimated by fitting the Carreau–Yasuda model with the complex viscosity data in the viscoelastic master curve (Figure 4.20). The relaxation time (λ) is defined by dividing the η^0 by $G_N{}^0$, and both are found to increase at higher TVB content (Table 4.3). Considering the above thermomechanical and rheological characterizations, poly(S_{80}-r-TVB_{20}) with enhanced thermomechanical stability at room temperature in addition to the reprocessability seems to offer a great potential for practical applications (Figure 4.21).

To confirm the potential application of poly(S_{80}-r-TVB_{20}) for thermomechanically robust and readily processable IR transmitting lenses or windows, MWIR and LWIR optical transmittance were first analyzed by FT-IR spectroscopy using a 1.1 mm-thick of poly(S_{80}-r-TVB_{20}) film. Previously reported poly(S_{80}-r-DVB_{20}) [23], poly(S_{80}-r-DIB_{20}) [8], poly(S_{80}-r-TIB_{20}) [20], and poly(methyl methacrylate) (PMMA) were also prepared with the same thickness (*i.e.*, 1.1 mm) for comparison. MWIR transmittance of poly(S_{80}-r-TVB_{20}) in the range of 3–5 μm is somewhat lower than that of poly(S_{80}-r-DVB_{20}), possibly because of the relatively greater number of MWIR-absorbing sp^3 C–H bonds in the crosslinker structure. However, poly(S_{80}-r-TVB_{20}) still shows higher MWIR transmittance than poly(S_{80}-r-DIB_{20}) and poly(S_{80}-r-TIB_{20}) (Figure 4.22a and Table 4.4). We attribute this to the lower IR absorption by sp^3 C–H bonds of the poly(S_{80}-

r-TVB$_{20}$), due to the absence of methyl groups in the isopropenyl moieties, compared with poly(S$_{80}$-*r*-DIB$_{20}$) and poly(S$_{80}$-*r*-TIB$_{20}$). Meanwhile, owing to the smaller content of phenyl groups which generally show absorption peaks in the fingerprint region of 7–14 μm [19], poly(S$_{80}$-*r*-TVB$_{20}$) also exhibits 1.62–2.15 times higher LWIR transmittance than poly(S$_{80}$-*r*-DIB$_{20}$) and poly(S$_{80}$-*r*-DVB$_{20}$). The relatively higher content of phenyl groups in the poly(S$_{80}$-*r*-TVB$_{20}$) could result in somewhat lower LWIR transparency compared to the poly(S$_{80}$-*r*-TIB$_{20}$) (Figure 4.22a and Table 4.4), but it is quite difficult to precisely interpret the difference in the IR fingerprint peak absorptions with the chemical structures [19,20,23]. The refractive index of poly(S$_{80}$-*r*-TVB$_{20}$) is found to be $n = 1.88$–1.95 in the range of 532–829 nm (Table 4.5 and Figure 4.22b), which is close to the inverse vulcanized copolymers with a sulfur content of ≥70 wt % in the literature [12,17–19,41,42]. It is worth noting here that poly(S$_{80}$-*r*-TVB$_{20}$) possesses a much higher T_g value of 92.6 °C, even with the excellent IR optical transparency and high n value, whereas the previously reported sulfur-rich copolymers with 80 wt % of sulfur show T_g values below 30 °C, thus significantly restricting their practical applications at room temperature (Figure 4.23). The optical properties of poly(S-*r*-TVB)s can also be further improved by increasing the sulfur content at the expense of somewhat sacrificing their thermomechanical properties (Figure 4.22b, Figure 4.24, Table 4.5, and Table 4.6).

Following the investigation of IR transmittance and refractive index of poly(S_{80}-r-TVB$_{20}$), its applicability in MWIR and LWIR thermal imaging was further explored. Similar to the direct image without any window sample, an MWIR thermal image captured through the 1.1 mm-thick poly(S_{80}-r-TVB$_{20}$) window shows low attenuation and detailed resolution of a human subject (Figure 4.25a and 4.25c). Conversely, a large attenuation of MWIR is seen in the thermal image captured through a 1.1 mm-thick PMMA window (Figure 4.25b). To assess the LWIR thermal imaging capability, a letter-patterned poly(lactic acid) (PLA) sheet was placed at a 30 cm distance from an 80 °C hot plate (*i.e.*, a black body radiator), and thermal imaging of the PLA sheet was conducted using an LWIR camera with and without the window samples at a distance of 50 cm from the PLA sheet (Figure 4.26) [19]. A high-resolution LWIR image is observed from the 1.1 mm-thick poly(S_{80}-r-TVB$_{20}$) window (Figure 4.27c), whereas the PMMA window with the same thickness exhibits an almost opaque image (Figure 4.27b). LWIR thermal imaging can be largely affected by the measurement condition (*i.e.,* the temperature of the subject and surroundings) [19]. For example, aside from the experimental setup using a hot plate and patterned PLA sheet (Figure 4.26), the 1.1 mm-thick poly(S_{80}-r-TVB$_{20}$) window also shows a large attenuation of the LWIR light in a typical thermal imaging environment (Figure 4.28). However, it is found that a human subject can be clearly detected even at the outside with an ambient

1 7 9

temperature of around 19 °C, by applying a thinner poly(S_{80}-r-TVB_{20}) window with a thickness of 300 μm (Figure 4.29). In addition, although we have focused on poly(S_{80}-r-TVB_{20}) for IR optical applications requiring robust thermomechanical properties, poly(S-r-TVB) windows with higher sulfur content can definitely be utilized for capturing higher resolution thermal images (Figure 4.30).

4.3. Conclusion

In summary, we successfully synthesized thermomechanically robust and highly IR transparent sulfur-rich copolymers via *in-situ* microphase separation during one-pot inverse vulcanization of elemental sulfur (ES) by using self-crosslinkable 1,3,5-trivinylbenzene (TVB) as a new type of organic crosslinker. Based on the microphase-separated architecture with rigid self-crosslinked TVB-rich domain, the poly(S-*r*-TVB)s exhibit high modulus (≈2.0 GPa at 30 °C) and T_g (92.6 °C) values even with the sulfur content of 80 wt %. The large content of dynamic sulfur linkages can also impart good processability to poly(S-*r*-TVB)s as well as excellent IR transparency and high refractive index, thereby holding great promise for IR optical applications. We also envision that this *in-situ* microphase separation strategy will provide insights for advancement in diverse fields that require sulfur-rich copolymers with robust thermomechanical properties, including structural composite materials and reliable electronic devices.

4.4. Experimental

Materials: Elemental sulfur (ES, ≥99.5%), divinylbenzene (DVB, 80%), *N,N*-dimethylformamide (DMF, 99.8%, anhydrous), and poly(methyl methacrylate) (PMMA, Mw ~350,000) from Sigma-Aldrich, were used as received. 1,3-diisopropenylbenzene (DIB, 97%) from BOC Sciences, was used as received. 2,2'-azobis(isobutyronitrile) (AIBN, ≥98%) from TCI, was used after recrystallization. 1,3,5-triisopropenylbenzene (TIB, 97%) and 1,3,5-trivinylbenzene (TVB, 96%) were purchased from Uniplus. All other solvents and reagents were used as received from standard vendors.

General procedure for the preparation of poly(S-r-TVB)s: Poly(sulfur-*random*-trivinylbenzene) copolymer is designated as poly(S_x-*r*-TVB_y), where *x* and *y* indicate the average weight percentage (wt %) of ES and TVB in the polymer, respectively. A 50 ml vial equipped with a magnetic stirring bar was filled with elemental sulfur (S_8, detail masses are specified below) and heated in a thermostated oil bath at 160 °C. After the sulfur was molten and turned into a yellowish liquid, trivinylbenzene (TVB, detail masses are specified below) was added dropwise using a pipette (≈1 s per drop) under vigorous stirring; the complete addition of TVB took around 6 to 20 s depending on the different comonomer feeds. The mixture was further stirred at 160 °C for around 10 minutes until it became

1 8 2

vitrificated. The vial containing the resulting polymer was taken out of the oil bath and naturally cooled down to room temperature. The vial was then quenched by placing it in liquid nitrogen, and then the product was obtained by breaking the vial. In order to control the structure and properties of poly(S-*r*-TVB)s, inverse vulcanization was carried out with five different comonomer feeds (i.e., 30, 25, 20, 15, and 10 wt % of TVB in the feed).

Synthesis of poly(S$_{70}$-r-TVB$_{30}$): The inverse vulcanization was carried out following the general procedure shown above with ES (2.1 g, 8.22 mmol) and TVB (0.9 g, 5.76 mmol) to yield a dark red solid (91.0%). CHNS Elemental Analysis*;* C: 27.35%, H: 2.08%, S: 70.57%.

Synthesis of poly(S$_{75}$-r-TVB$_{25}$): The inverse vulcanization was carried out following the general procedure shown above with ES (2.25 g, 8.81 mmol) and TVB (0.75 g, 4.8 mmol) to yield a red solid (90.3%). CHNS Elemental Analysis; C: 22.61%, H: 1.74%, S: 75.65%.

Synthesis of poly(S$_{80}$-r-TVB$_{20}$): The inverse vulcanization was carried out following the general procedure shown above with ES (2.4 g, 9.39 mmol) and TVB (0.6 g, 3.84 mmol) to yield a reddish brown solid (90.7%) CHNS Elemental Analysis; C: 18.02%, H: 1.41 %, S: 80.57%.

Synthesis of poly(S$_{85}$-r-TVB$_{15}$): The inverse vulcanization was carried out following the general procedure shown above with ES (2.55 g, 9.98 mmol) and TVB (0.45 g,

2.88 mmol) to yield a brown solid (90.3%) CHNS Elemental Analysis; C: 13.83%, H: 0.98 %, S: 85.19%.

Synthesis of poly(S₉₀-r-TVB₁₀): The inverse vulcanization was carried out following the general procedure shown above with ES (2.7 g, 10.57 mmol) and TVB (0.3 g, 1.92 mmol) to yield a yellowish brown solid (88.3%). CHNS Elemental Analysis; C: 9.24%, H: 0.63%, S: 90.13%.

Synthesis of poly(S₈₀-r-DVB₂₀): Referring to reference 22, a 50ml vial equipped with a magnetic stirring bar was filled with ES (4.0 g, 15.65 mmol) and heated in a thermostated oil bath at 160 °C. After the ES was molten and turned into a yellowish liquid, DVB (1.0 g, 7.68 mmol) was added dropwise using a pipette (≈1 s per drop) under vigorous stirring. The mixture was stirred at 160 °C for 20 minutes until it became vitrificated. The vial containing the resulting polymer was taken out of the oil bath and naturally cooled down to room temperature. The vial was then quenched by placing it in liquid nitrogen, and then the product was obtained by breaking the vial. The obtained polymer was then cured additionally for 4 h at 140 °C to yield a yellow solid (92.3%). CHNS Elemental Analysis; C: 17.92%, H: 1.46%, S: 80.62%.

Synthesis of poly(S₈₀-r-DIB₂₀): Referring to reference 7, a 50ml vial equipped with a magnetic stirring bar was filled with ES (4.0 g, 15.65 mmol) and heated in a thermostated oil bath at 160 °C. After the ES was molten and turned into a yellowish

liquid, DIB (1.0 g, 6.32 mmol) was dropwise using a pipette (≈1 s per drop) under vigorous stirring. The mixture was stirred at 160 ℃ for 20 minutes until it became vitrificated. The vial containing the resulting polymer was taken out of the oil bath and naturally cooled down to room temperature. The vial was then quenched by placing it in liquid nitrogen, and then the product was obtained by breaking the vial. The obtained polymer was then cured additionally for 4 h at 140 ℃ to yield a red solid (91.2%). CHNS Elemental Analysis; C: 17.84 %, H: 1.65 %, S: 80.51 %.

Synthesis of poly(S_{80}-r-TIB$_{20}$): Referring to reference 19, a 50ml vial equipped with a magnetic stirring bar was filled with ES (4.0 g, 15.65 mmol) and heated in a thermostated oil bath at 160 ℃. After the ES was molten and turned into a yellowish liquid, TIB (1.0 g, 5.04 mmol) was dropwise using a pipette (≈1 s per drop) under vigorous stirring. The mixture was stirred at 160 ℃ for 15 minutes until it became vitrificated. The vial containing the resulting polymer was taken out of the oil bath and naturally cooled down to room temperature. The vial was then quenched by placing it in liquid nitrogen, and then the product was obtained by breaking the vial. The obtained polymer was then cured additionally for 4 h at 140 ℃ to yield a red solid (93.4%). CHNS Elemental Analysis; C: 17.56 %, H: 1.58 %, S: 80.86 %.

Synthesis of self-polymerized TVB (PTVB): A mixture of TVB (3.0 g, 19.2 mmol) and AIBN (0.12 g, 0.73 mmol) in a DMF (25 mL) was heated at 80 ℃ under a nitrogen atmosphere for 18 h. The mixture was cooled to room temperature and

precipitated and filtered with ethyl acetate (200 mL). White PTVB (80.7%) powder was obtained after drying under vacuum.

Preparation of free-standing poly(S-r-TVB) films: Poly(S-r-TVB) films were prepared by placing the bulk poly(S-r-TVB)s into a mold (40 mm (L) $\times$ 40 mm (W) $\times$ 1.1 mm (T)), made of Kapton® polyimide films and stainless steel spacer, and pressing (10 MPa) for 5 min (Figure 4.14). Different processing temperatures were applied for the poly(S-r-TVB)s with different TVB contents. 165, 170, and 175 °C were applied for the hot pressing of poly(S$_{90}$-r-TVB$_{10}$), poly(S$_{85}$-r-TVB$_{15}$), and poly(S$_{80}$-r-TVB$_{20}$), respectively. The thickness of the film was controlled using the stainless steel spacer inserted between two polyimide films. After the pressure was removed, the sample was allowed to cool to room temperature before the polyimide film was removed. The poly(S-r-TVB) samples for dynamic mechanical analysis (DMA) and rheological characterization were also prepared using the same procedure, but with spacers with different shapes and dimensions. Rectangular- and circular-shaped spacers of dimensions with 2 mm (L) $\times$ 20 mm (W) $\times$ 0.5 mm (T) and 60 mm (D) $\times$ 0.6 mm (T) were applied for preparing the samples of DMA and rheological characterization, respectively. The same processing procedure was utilized for the preparation of PMMA films with 300 µm and 1.1 mm thicknesses for comparative IR thermal imaging.

Instrumental and characterization techniques: The elemental content of poly(S-*r*-TVB)s was analyzed using an elemental analyzer (EA, Flash 2000, Thermo Scientific). ^{13}C cross-polarization magic-angle spinning solid-state nuclear magnetic resonance spectroscopy (^{13}C CP-MAS NMR) data were acquired at ambient temperature on Bruker AVANCE III HD 400 MHz Solid-state NMR spectrometer with an external magnetic field of 9.4 T. The operating frequency was 100.66 MHz for ^{13}C, and the spectra were referenced to TMS. The samples were contained in an HX CPMAS probe, with a 4 mm o.d. Zirconia rotor. AFM images were acquired using a Bruker Multimode8 AFM with a Nanoscope V controller using tapping mode in air, with all parameters including set-point, scan rate, and feedback gains adjusted to optimize image quality. Fourier transform infrared (FT-IR) spectra were recorded on a Bruker Alpha II FTIR spectrometer using attenuated total reflectance (ATR) and transmission modes. The thermal stability of poly(S-*r*-TVB)s were investigated by thermal gravimetric analysis (TGA) using a TA Instruments TGA Q5000 under a nitrogen atmosphere. The samples were heated from 25 °C to 800 °C at a heating rate of 10 °C min^{-1}. Differential scanning calorimetry (DSC) was run using a TA Instruments DSC Q2000 under a nitrogen atmosphere. Samples with a typical mass of 5–10 mg were encapsulated in sealed aluminum pans. All samples were first heated from –25 °C to 160 °C and then cooled down to –25 °C, which were followed by second heating at a constant rate

187

of 10 °C min^{-1}. During the measurement, different maximum temperatures of second heating were set for each sample to prevent contamination of the device due to possible degradation of poly(S-r-TVB) having a low TVB content. For poly(S$_{90}$-r-TVB$_{10}$), poly(S$_{85}$-r-TVB$_{15}$), and poly(S$_{80}$-r-TVB$_{20}$), the maximum second heating temperature was 160 °C. For poly(S$_{75}$-r-TVB$_{25}$) and poly(S$_{70}$-r-TVB$_{30}$), the maximum second heating temperatures were 180 °C and 200 °C. The small-, medium-, and wide- angle X-ray scattering (SAXS, MAXS, and WAXS) measurements were conducted at the 9A beamline at the Pohang Accelerator Laboratory (PAL), Korea. The scattering data were collected using MX170-HS and LX170-HS 2D CCD detector (Rayonix). The MX170-HS is located at 6 m and 2 m from the sample to collect SAXS and MAXS patterns. The LX170-HS detector is positioned at 0.22 m from the sample to collect WAXS data. The SAXS measurement was conducted separately, and MAXS and WAXS measurements were conducted simultaneously. 1D intensity profile versus the scattering vector q = $(4\pi / \lambda) \sin(\theta)$ was obtained from recorded 2D patterns, where $\lambda = 0.62$ Å (E = 20 KeV) is a wavelength of X-ray and θ is the scattering angle. The quantification of the microphase separation was calculated through the Guinier equation (1) and Debye equation (2) below,

$$\ln I(q) = \ln I(0) - q^2 R_g^2 / 3 \tag{1}$$

$$D(x) = \ln I(q) / \ln I(0) = 2(\exp(-x) + x - 1) / x^2 \tag{2}$$

where $I(0)$ is the scattering intensity of zero q, R_g is the radius of gyration, and $x =$ $(qR_g)^2$ [43]. Powder X-ray diffraction (XRD) patterns were recorded using Rigaku Ultima IVX-ray diffractometer with Cu-Kα radiation using 40 kV/40 mA as accelerating voltage/tube current. The sample powders were mounted on an aluminum holder and scanned from 5° to 90°. A solvent extraction experiment was performed by placing a small piece (ca. 30 mg) of poly(S-r-TVB) films into a 20 ml vial filled with toluene. After being stored in an oven at room temperature for 24 h, the film was recovered and dried at 60 °C under vacuum for 18 h. Gel fraction (f_g) was calculated using the equation,

$$f_g = W_a / W_d \tag{3}$$

where W_d and W_a are the weights of the dried film before and after the toluene solvent extraction, respectively. The dynamic mechanical analyzer (DMA, TA Instruments, Q800) was utilized to measure thermomechanical parameters. The temperature sweep was conducted at a heating rate of 3 °C min^{-1} and a frequency of 1 Hz. The rheological parameters of poly(S-r-TVB) were measured by a rheometer (Anton Paar, MCR 302e). The strain sweep was conducted with 100 rad s^{-1} of frequency. The frequency sweep was conducted in the linear viscoelastic (LVE) regime from 110 °C to 150 °C with 10 °C temperature intervals in the frequency range from 1 rad s^{-1} to 100 rad s^{-1}. The relaxation timescale (λ) was calculated as below,

$$\lambda = \eta^0 / G_N^0 \tag{4}$$

where η^0 and G_N^0 are the zero shear viscosity and plateau modulus at the tan delta minima, respectively. Refractive index measurement of poly(S-*r*-TVB) films was conducted on a Metricon 2010/M prism coupler at 532 nm, 632.8 nm, and 829 nm. Mid-wave infrared (MWIR) images of subjects were taken using a COX CC640 IR camera (3–5 µm transmitting range). An long-wave infrared (LWIR) camera (E54, FLIR) was utilized to capture ambient temperature LWIR (7.5–14 µm) thermograms. An FDM-type 3D printer (Stealth 450, ROKIT) was used to prepare a patterned PLA sheet for IR imaging.

4.5. References

[1] J. G. Smith, *Organic Chemistry*, McGraw Hill, **2011**.

[2] M. Vollmer, K. -P. Möllmann, *Infrared Thermal Imaging,* Wiley-VCH Verlag GmbH, **2017**.

[3] J. S. Sanghera, L. B. Shaw, I. D. Aggarwal, *C. R. Chimie.* **2002**, *5*, 873–883.

[4] X. Zhang, B. Bureau, P. Lucas, C. Boussard-Pledel, J. Lucas, *Chem. Eur. J.* **2008**, *14*, 432-442.

[5] J. Brandrup, E. H. Immergut, E. A. Grulke, *Polymer Handbook*, Wiley, **1999**.

[6] A. Javadi, A. Shockravi, A. Rafieimanesh, A. Malek, S. Ando, *Polym. Int.* **2015**, *64*, 486–495

[7] T. Higashihara, M. Ueda, *Macromolecules* **2015**, *48*, 1915–1929.

[8] W. J. Chung, J. J. Griebel, E. T. Kim, H. Yoon, A. G. Simmonds, H. J. Ji, P. T. Dirlam, R. S. Glass, J. J. Wie, N. A. Nguyen, B. W. Guralnick, J. Park, Á. Somogyi, P. Theato, M. E. Mackay, Y.-E. Sung, K. Char, J. Pyun, *Nat. Chem.* **2013**, *5*, 518–524.

[9] T. S. Kleine, R. S. Glass, D. L. Lichtenberger, M. E. Mackay, K. Char, R. A. Norwood, J. Pyun, *ACS Macro Lett.* **2020**, *9*, 245–259.

[10] T. Lee, P. T. Dirlam, J. T. Njardarson, R. S. Glass, J. Pyun, *J. Am. Chem. Soc.* **2022**, *144*, 5–22.

[11] A. Nishant, K. J. Kim, S. A. Showghi, R. Himmelhuber, T. S. Kleine, T. Lee, J. Pyun, R. A. Norwood, *Adv. Optical Mater.* **2022**, 2200176.

[12] J. J. Griebel, S. Namnabat, E. T. Kim, R. Himmelhuber, D. H. Moronta, W. J. Chung, A. G. Simmonds, K.-J. Kim, J. van der Laan, N. A. Nguyen, E. L. Dereniak, M. E. Mackay, K. Char, R. S. Glass, R. A. Norwood, J. Pyun, *Adv. Mater.* **2014**, *26*, 3014–3018.

[13] J. J. Griebel, N. A. Nguyen, S. Namnabat, L. E. Anderson, R. S. Glass, R. A. Norwood, M. E. Mackay, K. Char, J. Pyun, *ACS Macro Lett.* **2015**, *4*, 862–866.

[14] J. J. Griebel, N. A. Nguyen, A. V. Astashkin, R. S. Glass, M. E. Mackay, K. Char, J. Pyun, *ACS Macro Lett.* **2014**, *3*, 1258–1261.

[15] L. E. Anderson, T. S. Kleine, Y. Zhang, D. D. Phan, S. Namnabat, E. A. LaVilla, K. M. Konopka, L. Ruiz Diaz, M. S. Manchester, J. Schwiegerling, R. S. Glass, M. E. Mackay, K. Char, R. A. Norwood, J. Pyun, *ACS Macro Lett.* **2017**, *6*, 500–504.

[16] D. A. Boyd, C. C. Baker, J. D. Myers, V. Q. Nguyen, G. A. Drake, C. C. McClain, F. H. Kung, S. R. Bowman, W. Kim, J. S. Sanghera, *Chem. Commun.* **2017**, *53*, 259–262.

[17] T. S. Kleine, L. R. Diaz, K. M. Konopka, L. E. Anderson, N. G. Pavlopolous, N. P. Lyons, E. T. Kim, Y. Kim, R. S. Glass, K. Char, R. A. Norwood, J. Pyun, *ACS Macro Lett.* **2018**, *7*, 875–880.

[18] D. A. Boyd, V. Q. Nguyen, C. C. McClain, F. H. Kung, C. C. Baker, J. D. Myers, M. P. Hunt, W. Kim, J. S. Sanghera, *ACS Macro Lett.* **2019**, *8*, 113–116.

[19] T. S. Kleine, T. Lee, K. J. Carothers, M. O. Hamilton, L. E. Anderson, L. Ruiz Diaz, N. P. Lyons, K. R. Coasey, W. O. Parker Jr, L. Borghi, M. E. Mackay, K. Char, R. S. Glass, D. L. Lichtenberger, R. A. Norwood, J. Pyun, *Angew. Chem. Int. Ed.* **2019**, *58*, 17656–17660; *Angew. Chem.* **2019**, *131*, 17820–17824.

[20] T. S. Kleine, N. A. Nguyen, L. E. Anderson, S. Namnabat, E. A. LaVilla, S. A. Showghi, P. T. Dirlam, C. B. Arrington, M. S. Manchester, J. Schwiegerling, R. S. Glass, K. Char, R. A. Norwood, M. E. Mackay, J. Pyun, *ACS Macro Lett.* **2016**, *5*, 1152–1156.

[21] H. W. McCormick, *J. Polym. Sci.* **1957**, *25*, 488–490.

[22] J. J. Griebel, R. S. Glass, K. Char, J. Pyun, *Prog. Polym. Sci.* **2016**, *58*, 90–125.

[23] S. Park, D. Lee, H. Cho, J. Lim, K. Char, *ACS Macro Lett.* **2019**, *8*, 1670–1675.

[24] S. Park, M. Chung, A. Lamprou, K. Seidel, S. Song, C. Schade, J. Lim, K. Char, *Chem. Sci.* **2022**, *13*, 566–572.

[25] X. Wu, J. A. Smith, S. Petcher, B. Zhang, D. J. Parker, J. M. Griffin, T. Hasell, *Nat. Commun.* **2019**, *10*, 647.

[26] L. J. Dodd, Ö. Omar, X. Wu, T. Hasell, *ACS Catal.* **2021**, *11*, 4441–4455.

[27] S. Diez, A. Hoefling, P. Theato, W. Pauer, Polymers **2017**, *9*, 59.

[28] J. A. Smith, X. Wu, N. G. Berry, T. Hasell, *J. Polym. Sci. A Polym. Chem.* **2018**, *56*, 1777–1781.

[29] J. A. Smith, S. J. Green, S. Petcher, D. J. Parker, B. Zhang, M. J. H. Worthington, X. Wu, C. A. Kelly, T. Baker, C. T. Gibson, J. A. Campbell, D. A. Lewis, M. J. Jenkins, H. Willcock, J. M. Chalker, T. Hasell, *Chem. Eur. J.* **2019**, *25*, 10433–10440.

[30] B. Zhang, S. Petcher, T. Hasell, *Chem. Commun.* **2019**, *55*, 10681–10684.

[31] J. M. Scheiger, M. Hoffmann, P. Falkenstein, Z. Wang, M. Rutschmann, V. W. Scheiger, A. Grimm, K. Urbschat, T. Sengpiel, J. Matysik, *Angew. Chem. Int. Ed.* **2022**, *61*, e202114896; Angew. Chem. **2022**, *134*, e202114896.

[32] E. Uzunlar, J. Schwartz, O. Phillips, P. A. Kohl, *J. Electom. Packag.* **2016**, *138*, 020802.

[33] B. Morèse-Séguéla, M. St-Jacques, J. M. Renaud, J. Prod'homme, *Macromolecules*, **1980**, *13*, 100–106.

[34] M. Qu, F. Deng, S. M. Kalkhoran, A. Gouldstone, A. Robisson, K. J. Van Vliet, *Soft Matter* **2011**, *7*, 1066–1077.

[35] J. Choi, S. Won, H. J. Yoon, J. H. Lee, H. W. Jang, J. Jeon, A. Y. Kim, S. H. Park, J. H. Youk, M. Lee, J. J. Wie, *Nano Energy* **2022**, *92*, 106761.

[36] T. Suzuki, N. Osaka, H. Endo, M. Shibayama, Y. Ikeda, H. Asai, N. Higashitani, Y. Kokubo, S. Kohjiya, *Macromolecules* **2010**, *43*, 1556–1563.

[37] S.-K. Kim, N. A. Nguyen, J. J. Wie, H. S. Park, *Nanoscale.* **2015**, *7*, 8864–8872.

[38] R.A. DiStasio Jr, G. von Helden, R.P. Steele, M. Head-Gordon, *Chem. Phys. Lett.* **2007**, *437*, 277–283.

[39] C. R. López-Barrón, H. Zhou, J. M. Younker, J. A. Mann, *Macromolecules* **2017**, *50*, 9048–9057.

[40] Y. Hong, S. Bao, X. Xiang, X. Wang, *ACS Macro Lett.* **2020**, *9*, 889–894.

[41] J. M. Lee, G. Y. Noh, B. G. Kim, Y. Yoo, W. J. Choi, D.-G. Kim, H. G. Yoon, Y. S. Kim, *ACS Macro Lett.* **2019**, *8*, 912–916.

[42] D. H. Kim, W. Jang, K. Choi, J. S. Choi, J. Pyun, J. Lim, K. Char, S. G. Im, *Sci. Adv.* **2020**, *6*, eabb5320.

[43] R.-J. Roe, *Methods of X-Ray and Neutron Scattering in Polymer Science*, Oxford U. Press: New York, **2000**.

Table 4.1. Characteristics of the poly(S-*r*-TVB)s with 70 to 90 wt % feed ratio.

	poly(S$_{70}$-*r*-TVB$_{30}$)	poly(S$_{75}$-*r*-TVB$_{25}$)	poly(S$_{80}$-*r*-TVB$_{20}$)	poly(S$_{85}$-*r*-TVB$_{15}$)	poly(S$_{90}$-*r*-TVB$_{10}$)
f_g[a]	0.999	0.999	0.998	0.998	0.992
$T_{d, 5\%}$[b] (°C)	248.5	245.9	243.3	220.1	196.1
1st T_g[c] (°C)	173.1[d]	148.6[d]	92.6	47.6	19.4
2nd T_g[c] (°C)			139.8	138.6	137.8
Color[e]	Dark red	Red	Redish brown	Brown	Yellowish brown

[a]Gel fraction from toluene solvent extraction. [b]Decomposition temperature, defined as 5 wt % loss. [c]Glass transition temperature, determined by differential scanning calorimetry (DSC). [d]Single glass transition temperature. [e]Apparent color.

Table 4.2. E' at 30 °C, T_g, Tan δ max, and crosslinking density of poly(S-*r*-TVB)s extracted and calculated from temperature sweep curves of DMA temperature sweep.

Sample	E'[a] at 30 °C (MPa)	E'_{high}[b] (MPa)	T_g[c] (tan δ, °C)	Tan δ Max[d]	v_e [e] (mol m^{-3})
poly(S$_{80}$-*r*-TVB$_{20}$)	1963.0 ± 137.3	23.5 ± 2.7	91.6 ± 1.2	0.72 ± 0.02	2273.3
poly(S$_{85}$-*r*-TVB$_{15}$)	2315.3 ± 457.9	19.2 ± 1.7	50.7 ± 3.3	0.97 ± 0.06	2052.6
poly(S$_{90}$-*r*-TVB$_{10}$)	300.9 ± 79.2	11.9 ± 3.7	47.1 ± 3.1	0.94 ± 0.15	1294.9

[a]Storage modulus of poly(S-*r*-TVB)s at 30 °C. [b]Storage modulus of the poly(S-*r*-TVB)s at the rubbery plateau. [c]Glass transition temperatures of the poly(S-*r*-TVB)s at the tan delta maxima. [d]Tan delta values of the poly(S-*r*-TVB)s at the tan delta maxima. [e]Crosslinking densities of the poly(S-*r*-TVB)s.

Table 4.3. Rheological parameters of poly(S-*r*-TVB)s extracted and calculated from the viscoelastic master curve.

Sample name	$G_N^{0[a]}$ (MPa)	$\eta^{0[b]}$ (Pa·s)	$\lambda^{[c]}$ (s)
poly(S$_{80}$-*r*-TVB$_{20}$)	5.28 (3.0 rad s^{-1})	3.33 x 10^8	63.1
poly(S$_{85}$-*r*-TVB$_{15}$)	4.16 (at 13.3 rad s^{-1})	1.99 x 10^8	47.8
poly(S$_{90}$-*r*-TVB$_{10}$)	2.51 (at 465.0 rad s^{-1})	1.51 x 10^7	6.0

[a] Plateau modulus of the poly(S-*r*-TVB)s at the tan delta minima. [b] Zero shear viscosity of the poly(S-*r*-TVB)s. [c]Relaxation timescale of the poly(S-*r*-TVB)s.

Table 4.4. IR transmittances of poly(S_{80}-*r*-TVB$_{20}$), poly(S_{80}-*r*-DVB$_{20}$), poly(S_{80}-*r*-DIB$_{20}$), poly(S_{80}-*r*-TIB$_{20}$), and PMMA.

Sample[a]	Transmittance (%T)	
	(3–5um)	(7–14um)
poly(S_{80}-*r*-TVB$_{20}$)	37.95 ± 2.0	1.31 ± 0.4
poly(S_{80}-*r*-DVB$_{20}$)	39.45 ± 2.2	0.81 ± 0.3
poly(S_{80}-*r*-DIB$_{20}$)	36.71 ± 1.9	0.61 ± 0.1
poly(S_{80}-*r*-TIB$_{20}$)	35.25 ± 2.1	1.38 ± 0.4
PMMA	6.09 ± 0.8	0.36 ± 0.1

[a]The thickness of all poly(S-*r*-TVB) films is 1.1 mm.

Table 4.5. Refractive indices versus wavelength plot of poly(S-*r*-TVB) films.

Sample[a]	532 nm	632.8 nm	829 nm
poly(S$_{80}$-*r*-TVB$_{20}$)	1.95	1.92	1.88
poly(S$_{85}$-*r*-TVB$_{15}$)	1.99	1.95	1.92
poly(S$_{90}$-*r*-TVB$_{10}$)	2.00	1.97	1.94

[a]The thickness of all poly(S-*r*-TVB) films is 1.1 mm.

Table 4.6. IR transmittances of poly(S_{80}-r-TVB$_{20}$), poly(S_{80}-r-DVB$_{20}$), poly(S_{80}-r-DIB$_{20}$), poly(S_{80}-r-TIB$_{20}$), and PMMA.

Sample[a]	Transmittance (%T)	
	(3–5um)	(7–14um)
poly(S_{80}-r-TVB$_{20}$)	37.95 ± 2.0	1.31 ± 0.4
poly(S_{80}-r-DVB$_{20}$)	39.45 ± 2.2	0.81 ± 0.3
poly(S_{80}-r-DIB$_{20}$)	36.71 ± 1.9	0.61 ± 0.1
poly(S_{80}-r-TIB$_{20}$)	35.25 ± 2.1	1.38 ± 0.4
PMMA	6.09 ± 0.8	0.36 ± 0.1

[a]The thickness of all poly(S-r-TVB) films is 1.1 mm.

Figure 4.1. Schematic illustration for the synthesis of poly(S-*r*-TVB) from the ES and TVB, and its *in-situ* microphase-separated architecture for IR optical applications.
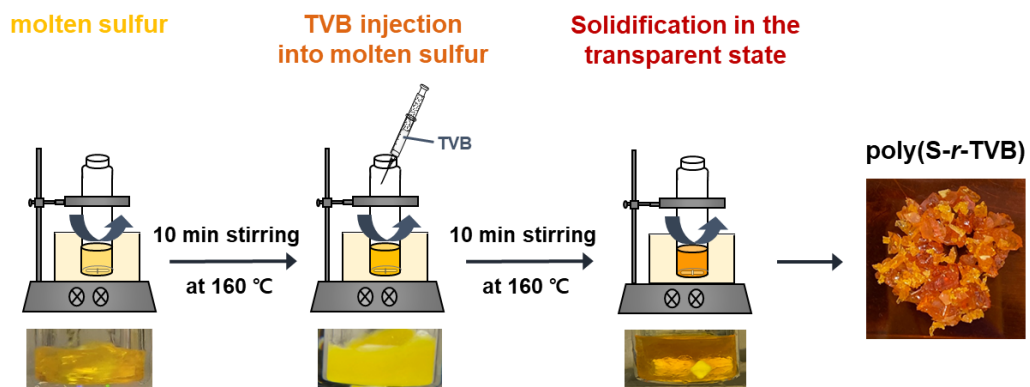
Figure 4.2. Schematic illustration for the synthesis procedure of poly(S-*r*-TVB)s.
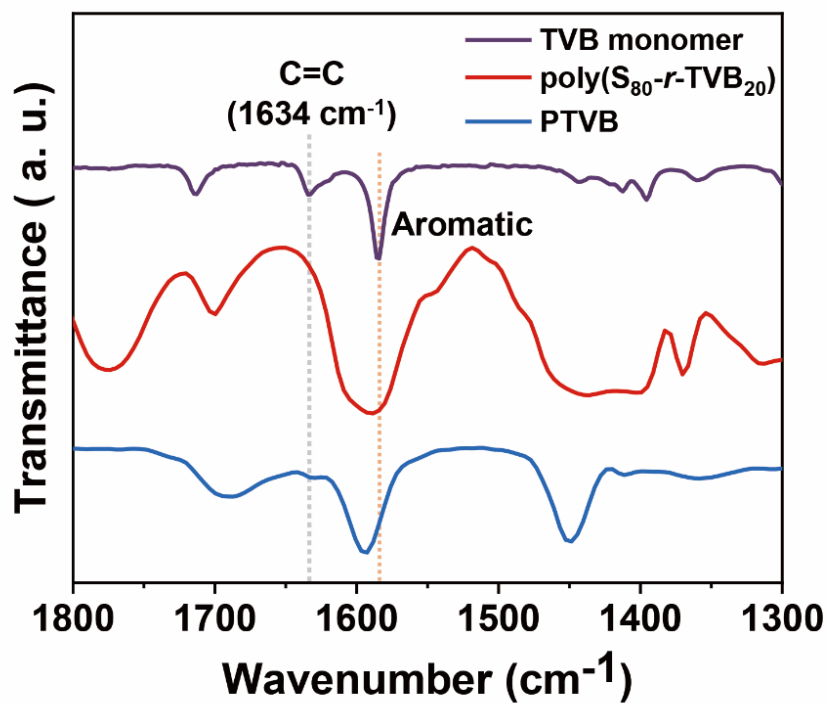
Figure 4.3. FT-IR (ATR mode) spectra of TVB monomer, poly(S_{80}-r-TVB$_{20}$), and PTVB.
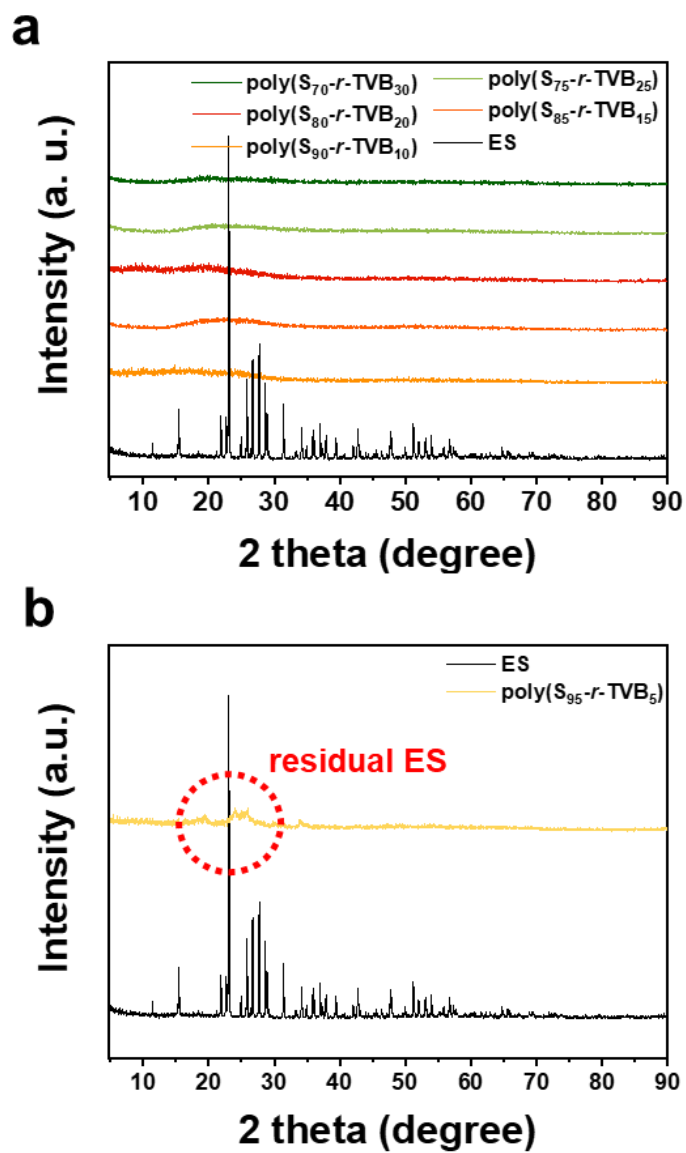
Figure 4.4. XRD profiles of ES and poly(S-*r*-TVB)s with (a) 10–30 wt % and (b) 5 wt % TVB contents.

a poly(S₇₀-*r*-TVB₃₀)

b poly(S₆₀-*r*-TVB₄₀)

Acceleration of the reaction (poly(S₆₀-*r*-TVB₄₀))
→ heterogeneous and incomplete product
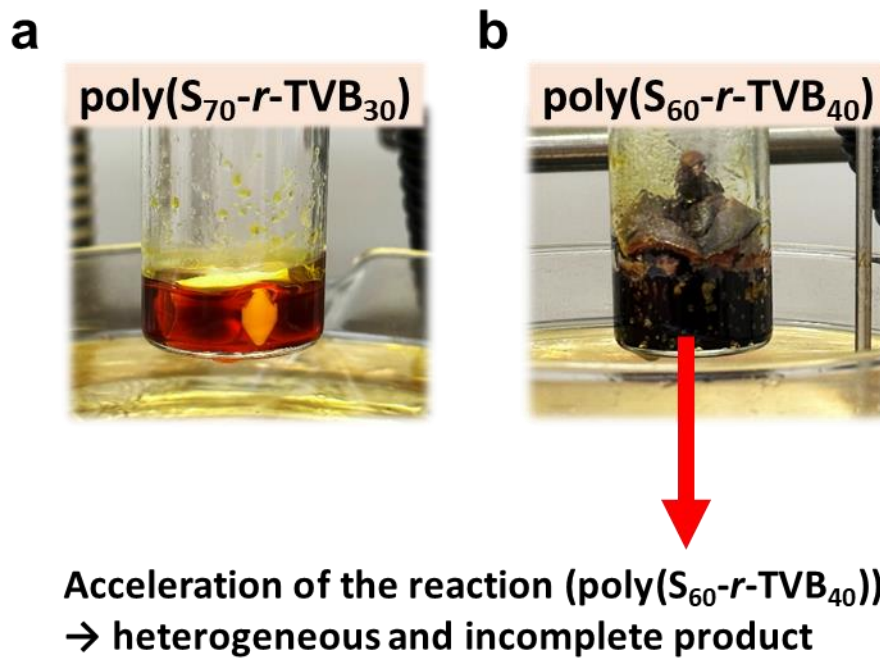
Figure 4.5. (a) Homogeneous and complete product of poly(S_{70}-*r*-TVB$_{30}$) and (b) heterogeneous and incomplete product of poly(S_{60}-*r*-TVB$_{40}$).
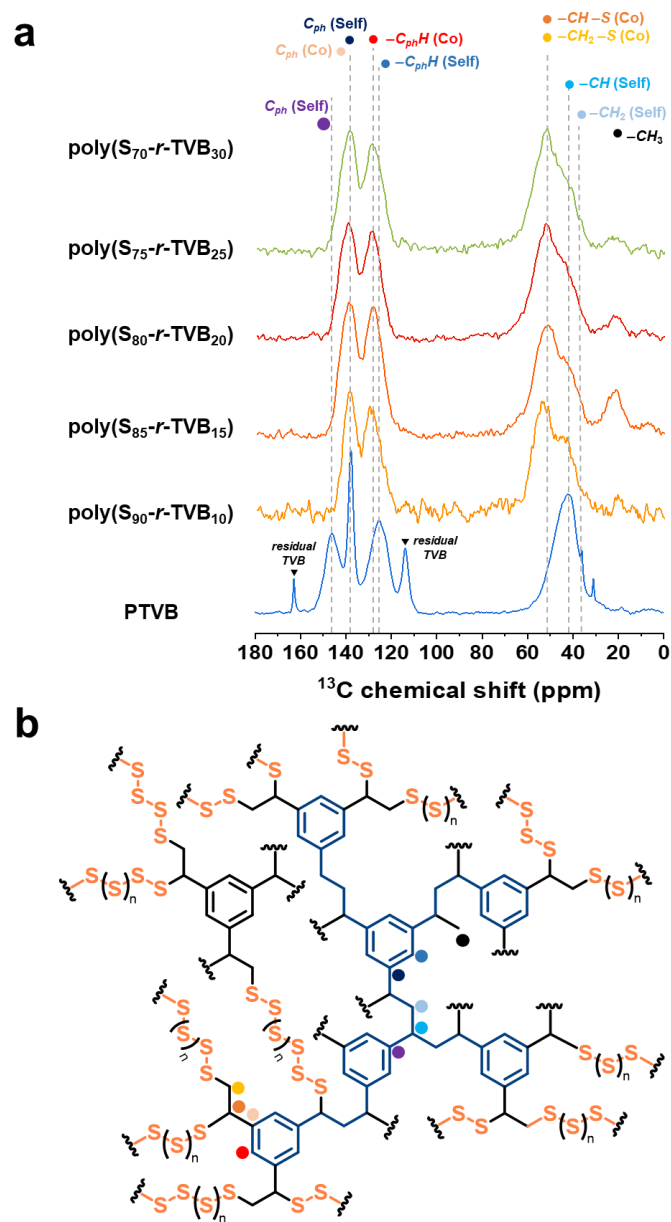
Figure 4.6. (a) ^{13}C CP-MAS NMR spectra of PTVB and poly(S-*r*-TVB)s. (b) Expected chemical structure of poly(S-*r*-TVB)s with ^{13}C NMR peak assignments.
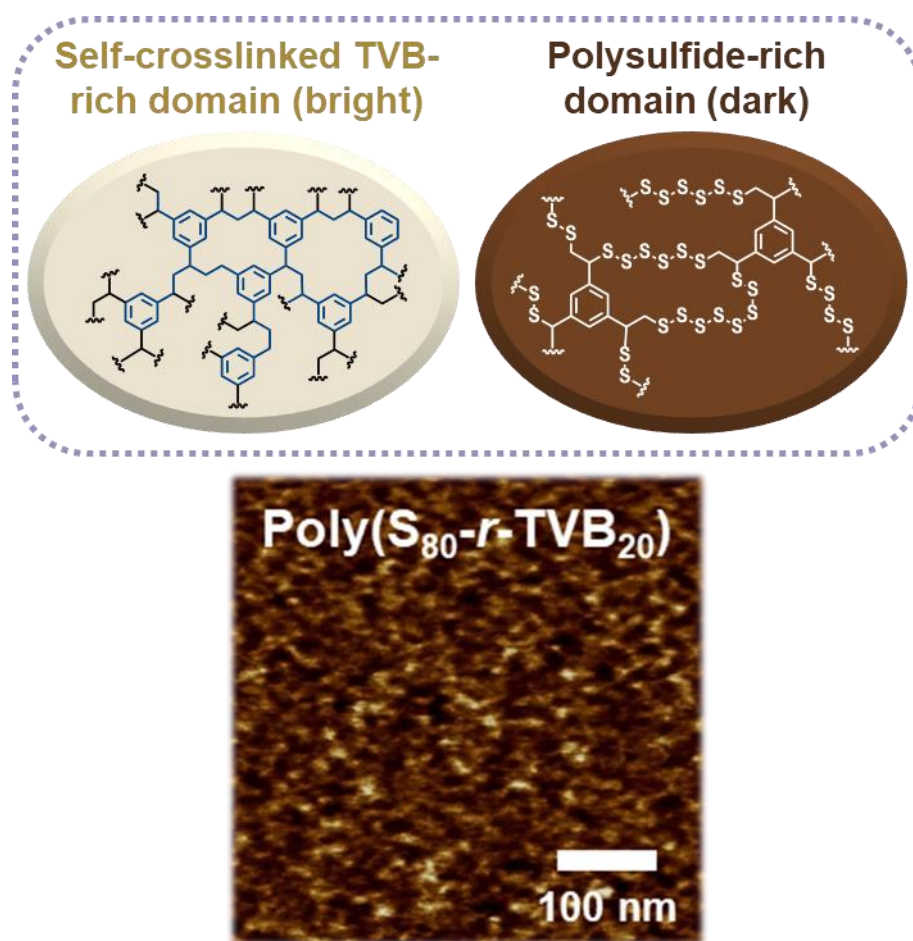
Figure 4.7. Tapping mode AFM phase image of poly(S_{80}-*r*-TVB$_{20}$) and corresponding schematic illustration of microphase-separated domains (scale bars: 100 nm).

poly(S$_{70}$-r-TVB$_{30}$)

poly(S$_{75}$-r-TVB$_{25}$)

poly(S$_{80}$-r-TVB$_{20}$)

poly(S$_{85}$-r-TVB$_{15}$)

poly(S$_{90}$-r-TVB$_{10}$)
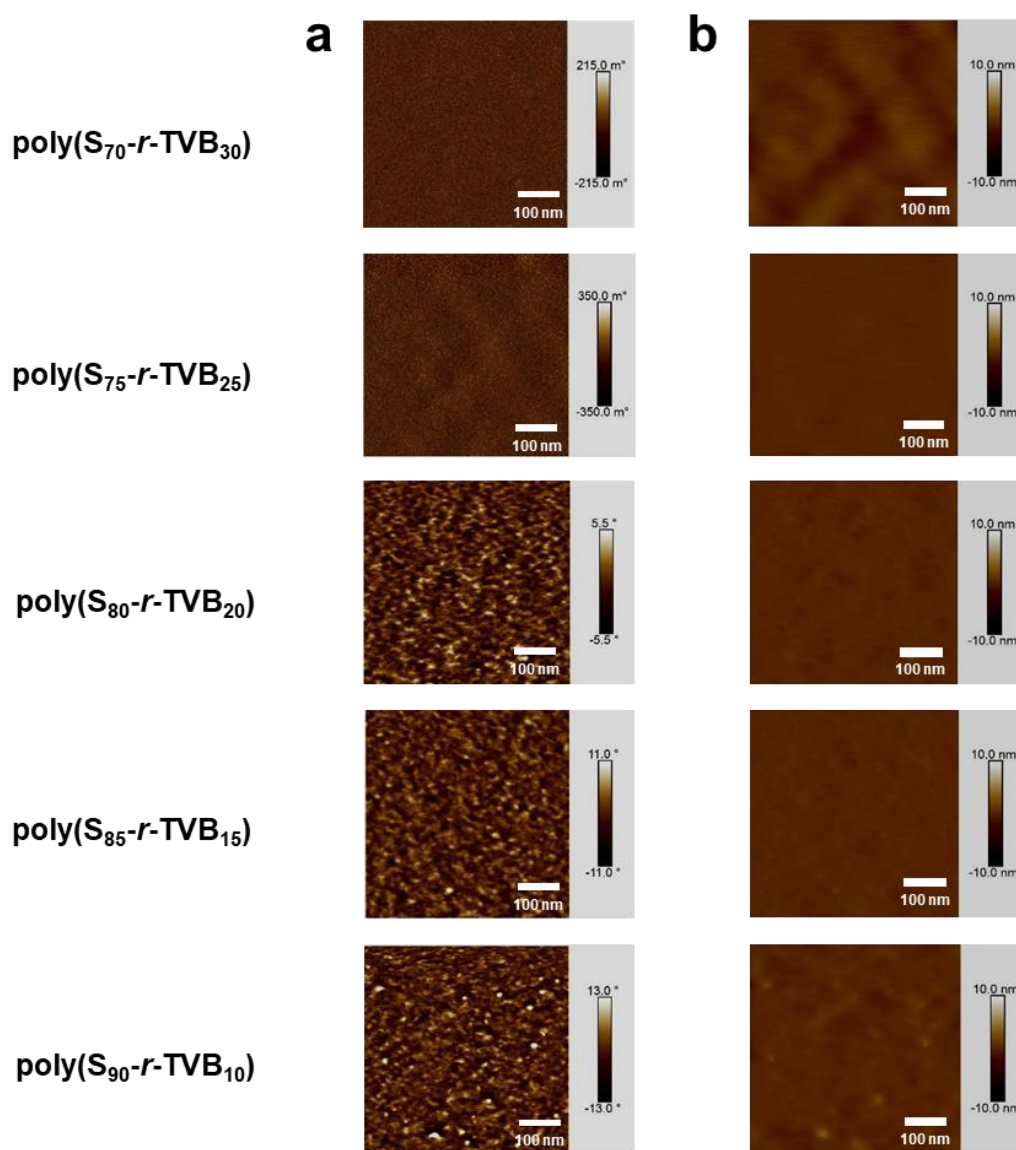
Figure 4.8. Tapping mode AFM images of poly(S-r-TVB)s. (a) Phase-contrast images and (b) Z-height contrast images. All the scale bars are 100 nm.
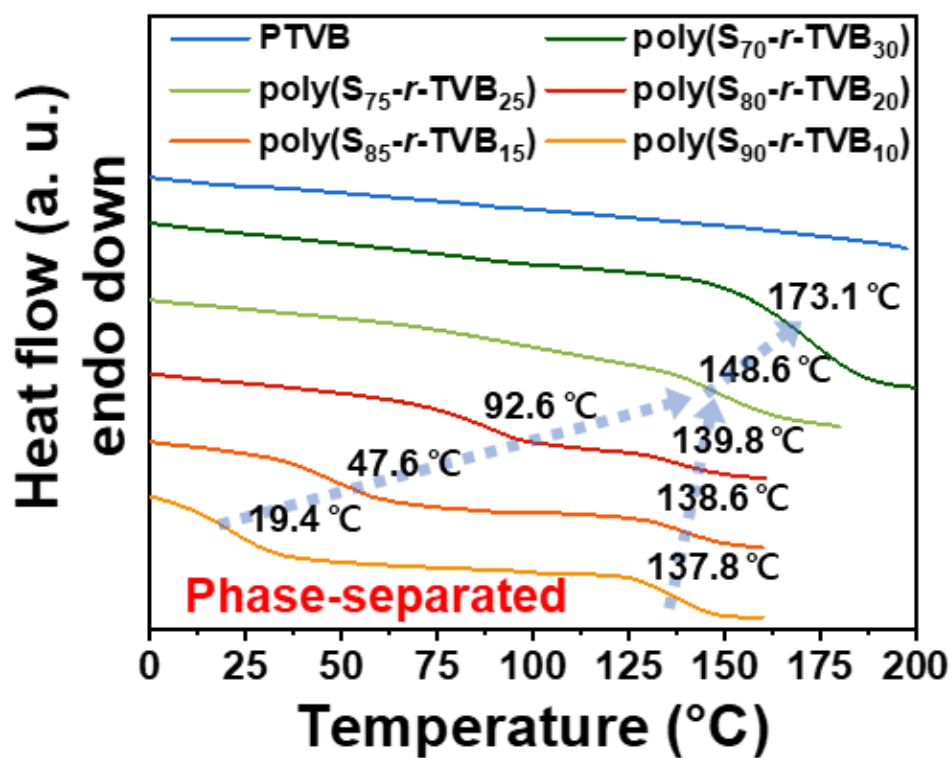
Figure 4.9. DSC thermograms of poly(S-*r*-TVB)s.
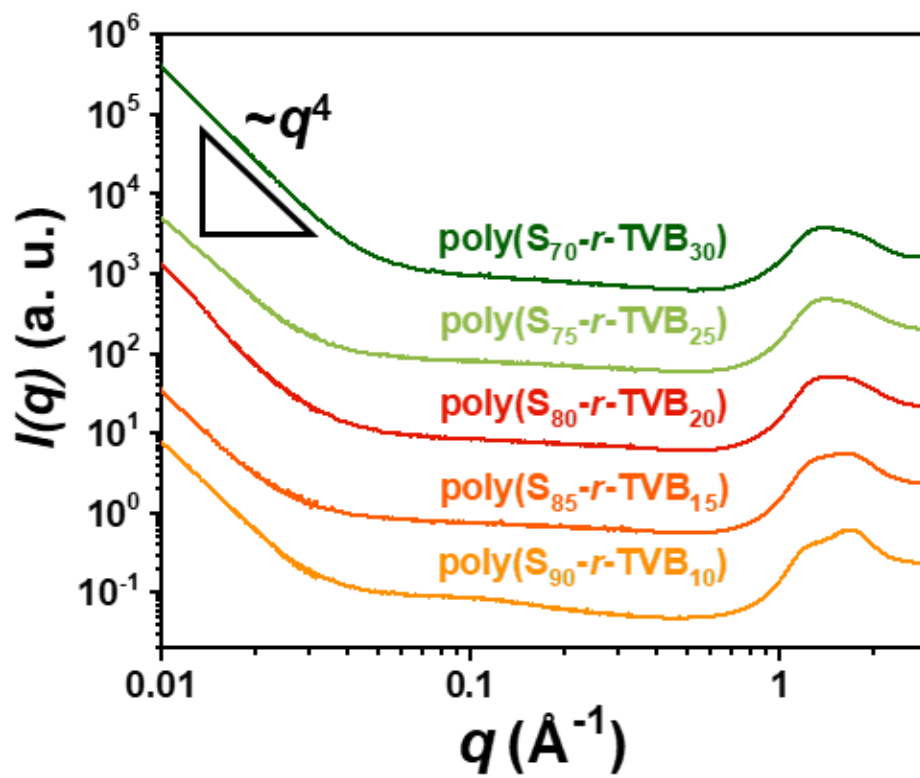
Figure 4.10. 1D X-ray scattering profiles for poly(S-*r*-TVB)s
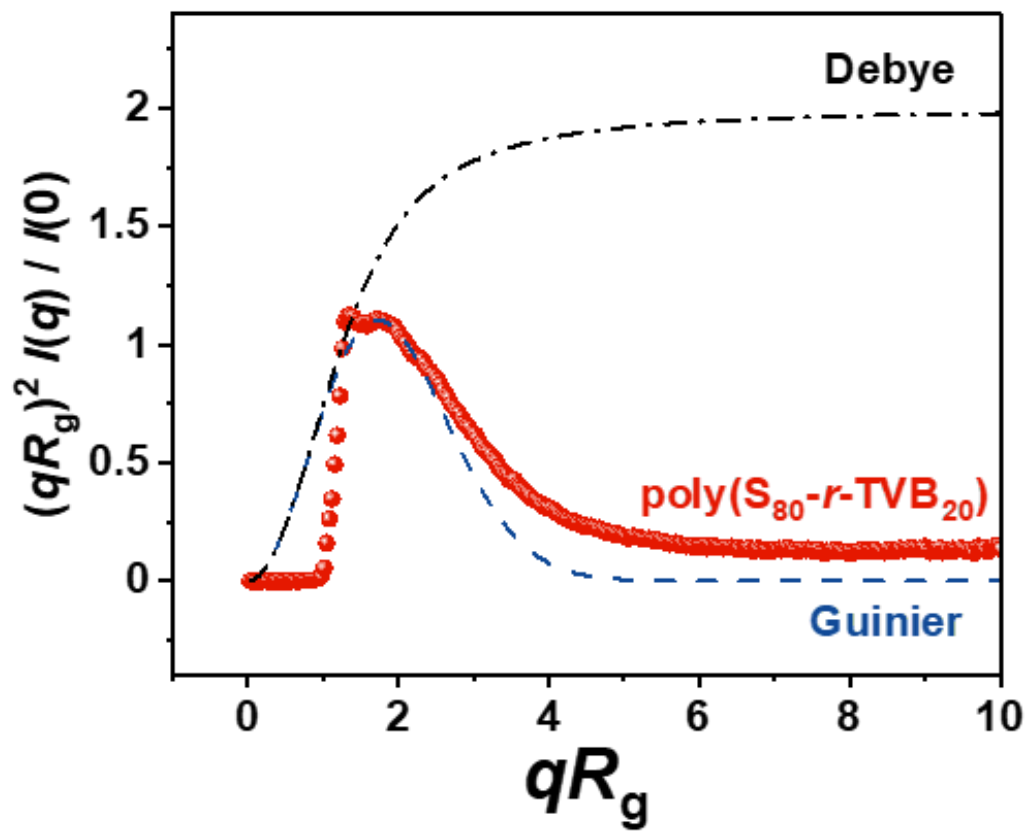
Figure 4.11. Kratky plot of poly(S_{80}-*r*-TVB$_{20}$).
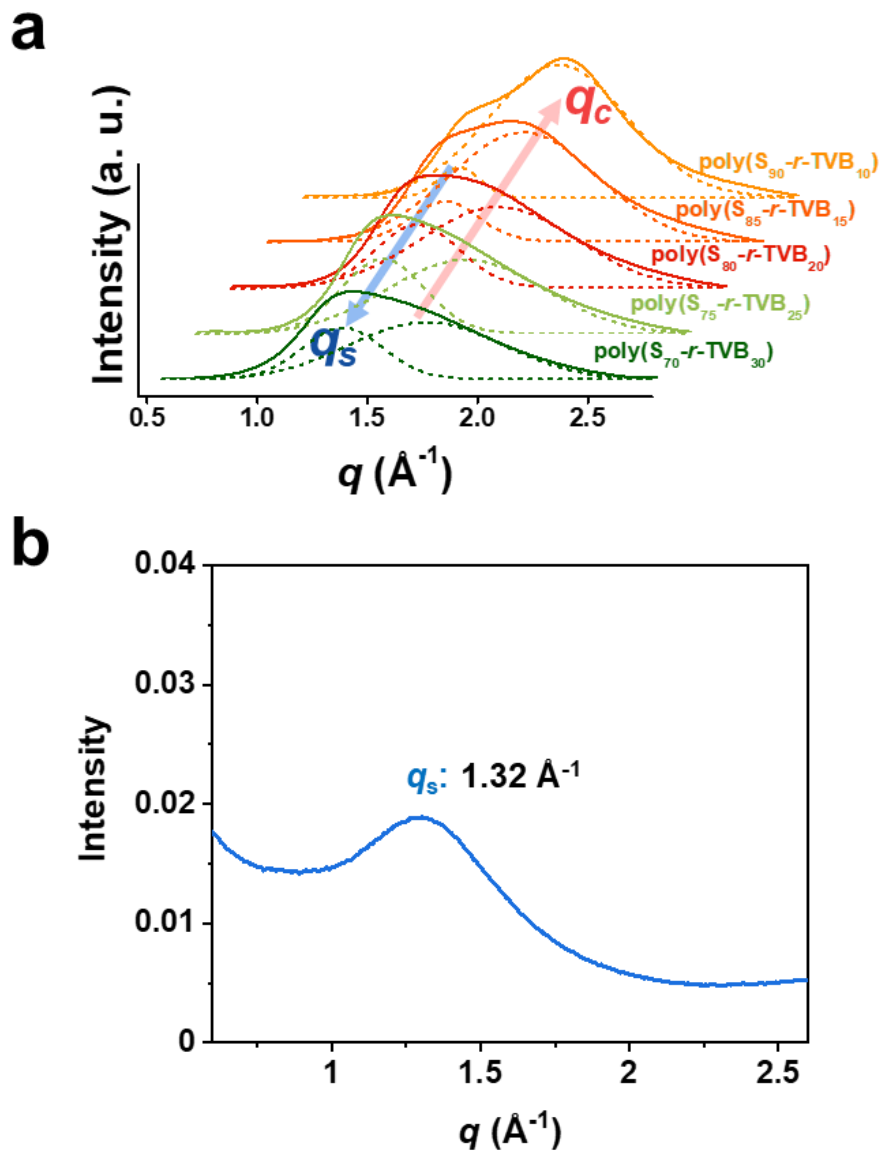
Figure 4.12. (a) Baseline-subtracted 1D WAXS profiles of poly(S-*r*-TVB)s. The solid lines represent measured data, and the dashed lines represent deconvoluted peaks using Gaussian functions and (b) proton mobility 1D WAXS profile of PTVB.
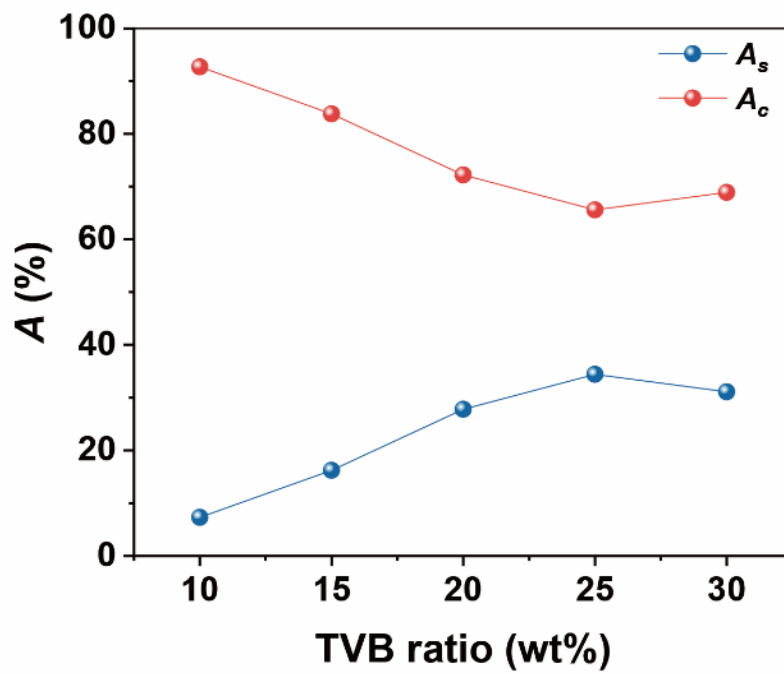
Figure 4.13. A plot of the peak area vs. TVB ratio of poly(S-*r*-TVB)s.
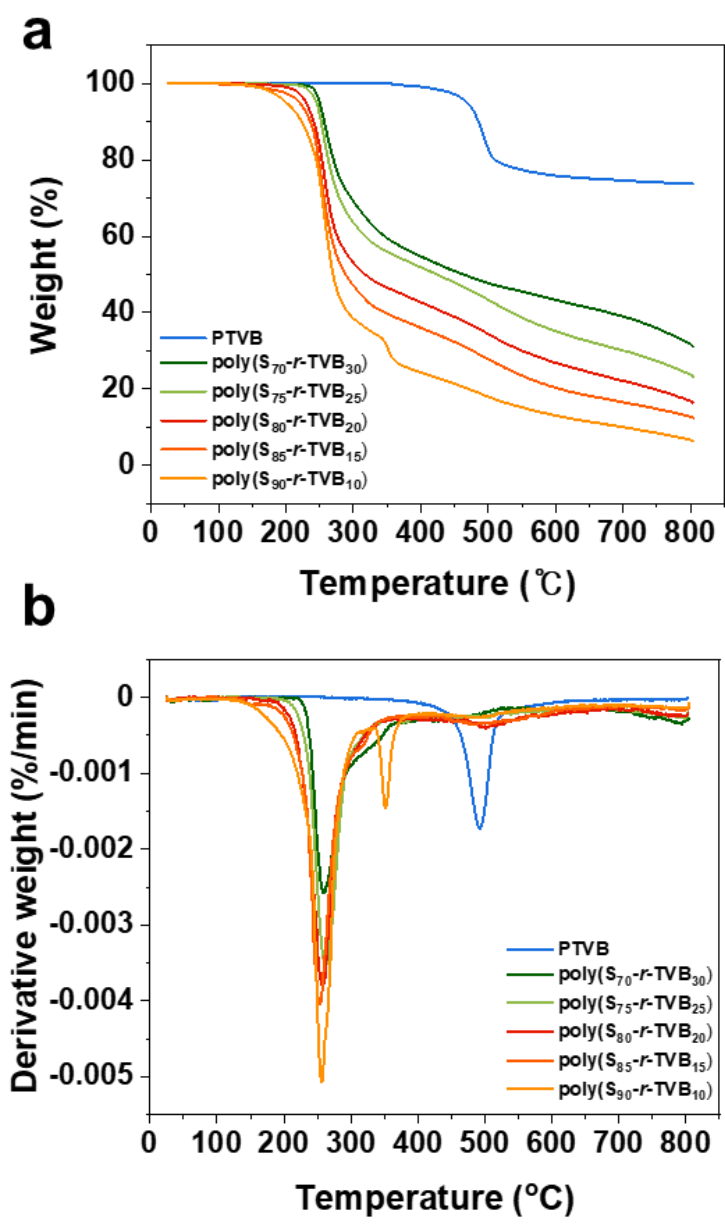
Figure 4.14. (a) TGA thermograms and (b) derivative TGA profiles of PTVB and poly(S-*r*-TVB)s.
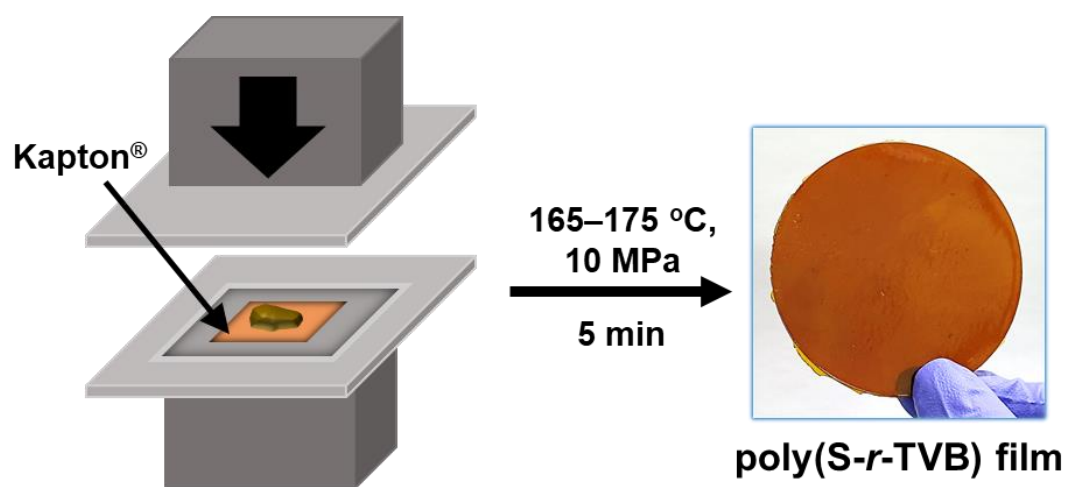
Figure 4.15. Schematic illustration for the preparation of poly(S-*r*-TVB) films *via* hot pressing.
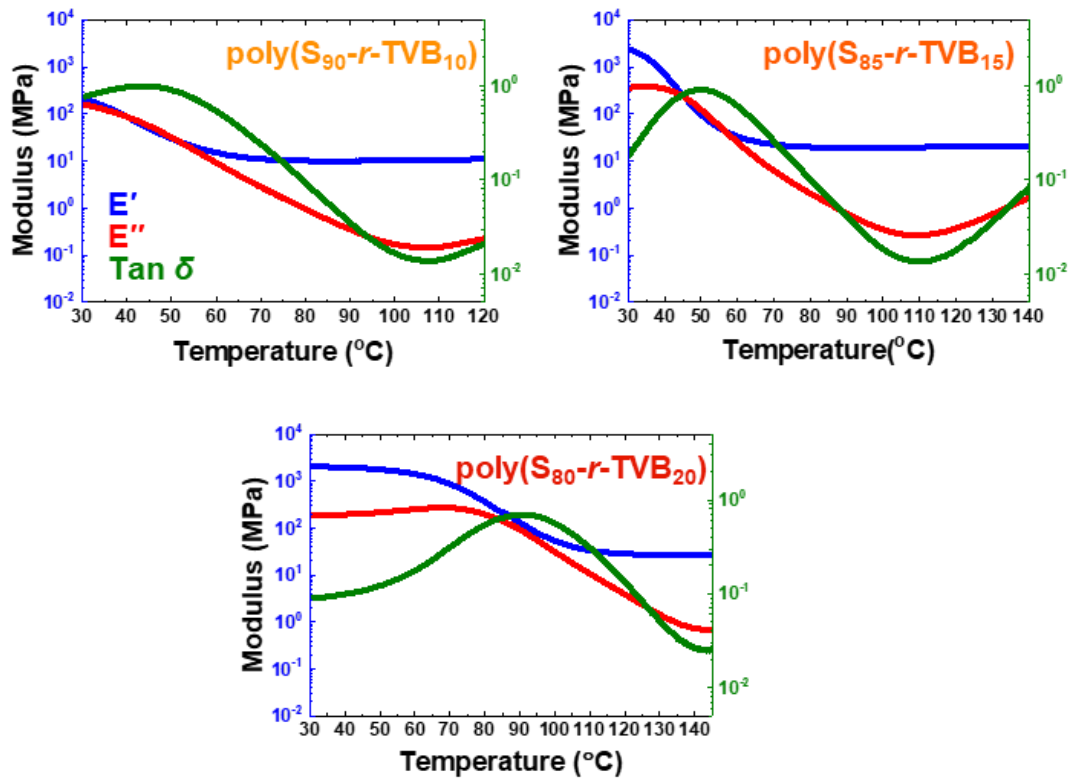
Figure 4.16. DMA temperature sweep tests of poly(S-*r*-TVB)s.
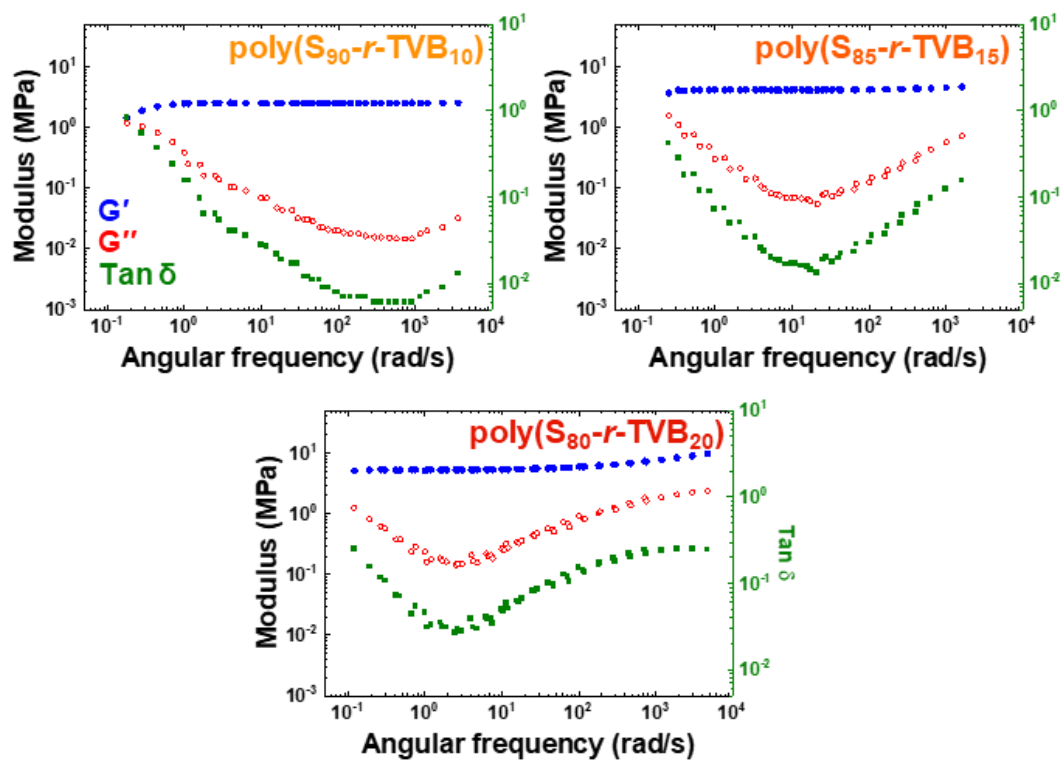
Figure 4.17. Master curves of poly(S-*r*-TVB) films at 130 ℃ of reference temperature.
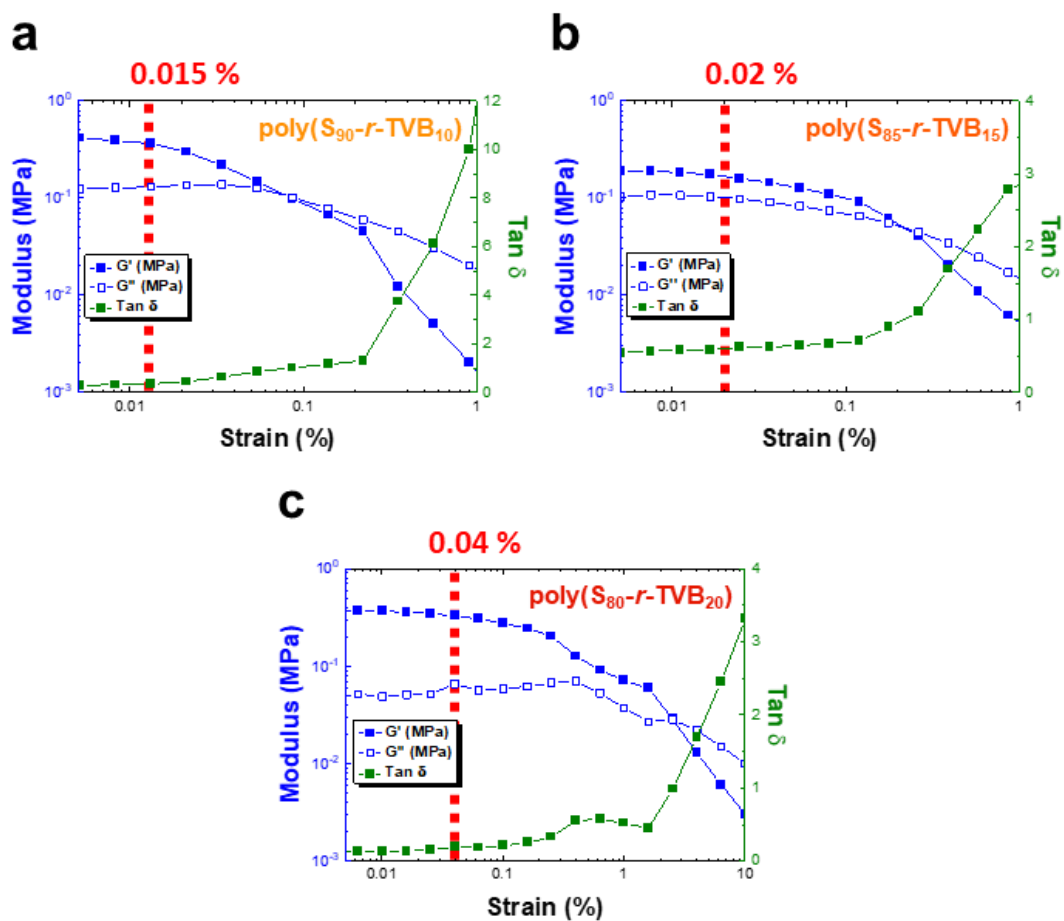
Figure 4.18. The result of strain sweep tests of the (a) poly(S$_{90}$-*r*-TVB$_{10}$), (b) poly(S$_{85}$-*r*-TVB$_{15}$), and (c) poly(S$_{80}$-*r*-TVB$_{20}$). The red dashed lines indicate maximum strain in the linear viscoelastic (LVE) region.
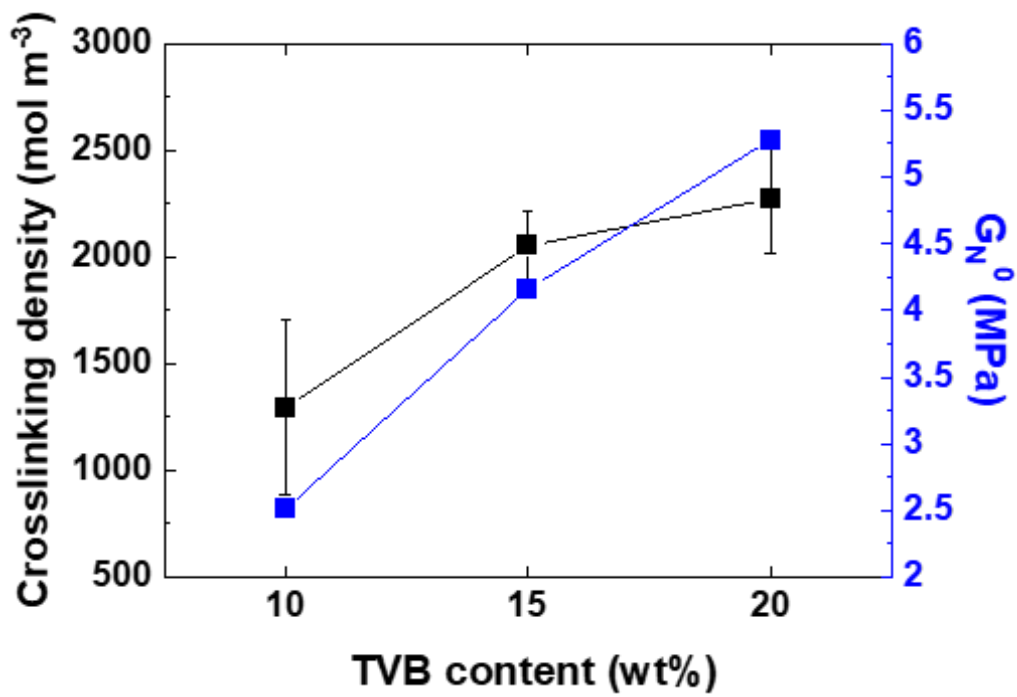
Figure 4.19. Plots of crosslinking density and plateau modulus (G_N^0) as a function of TVB contents in poly(S-*r*-TVB)s.
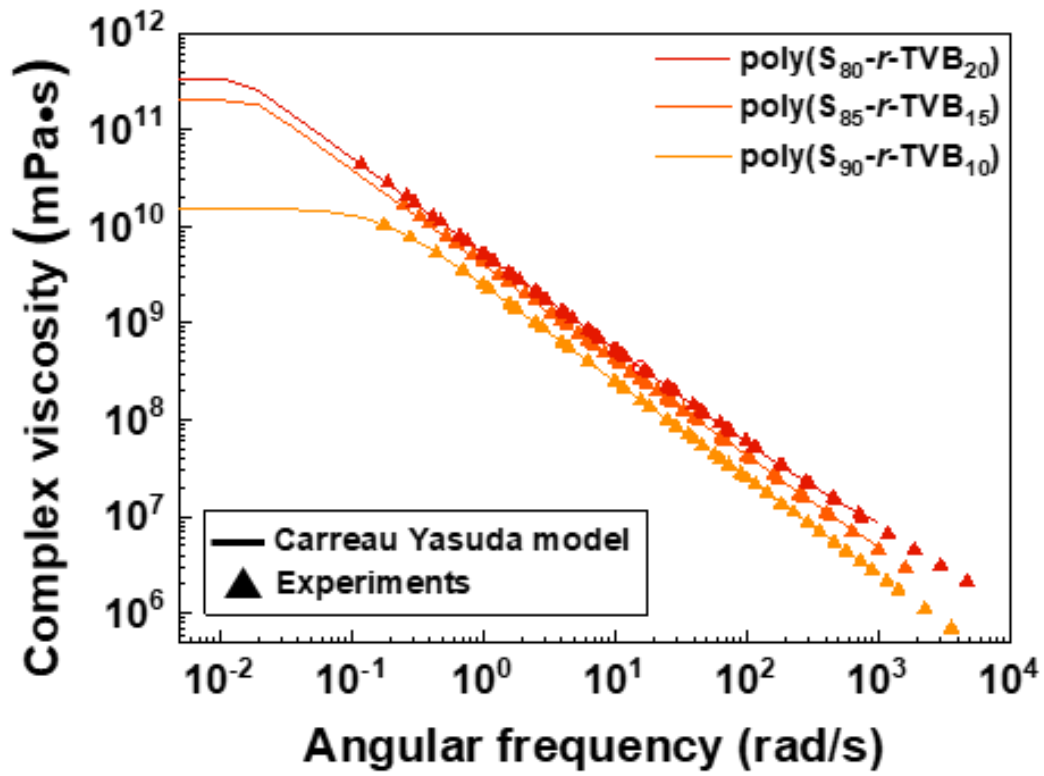
Figure 4.20. Plots of complex viscosity versus angular frequency for poly(S-*r*-TVB)s. The solid lines denote estimated fitting via the Carreau–Yasuda model.
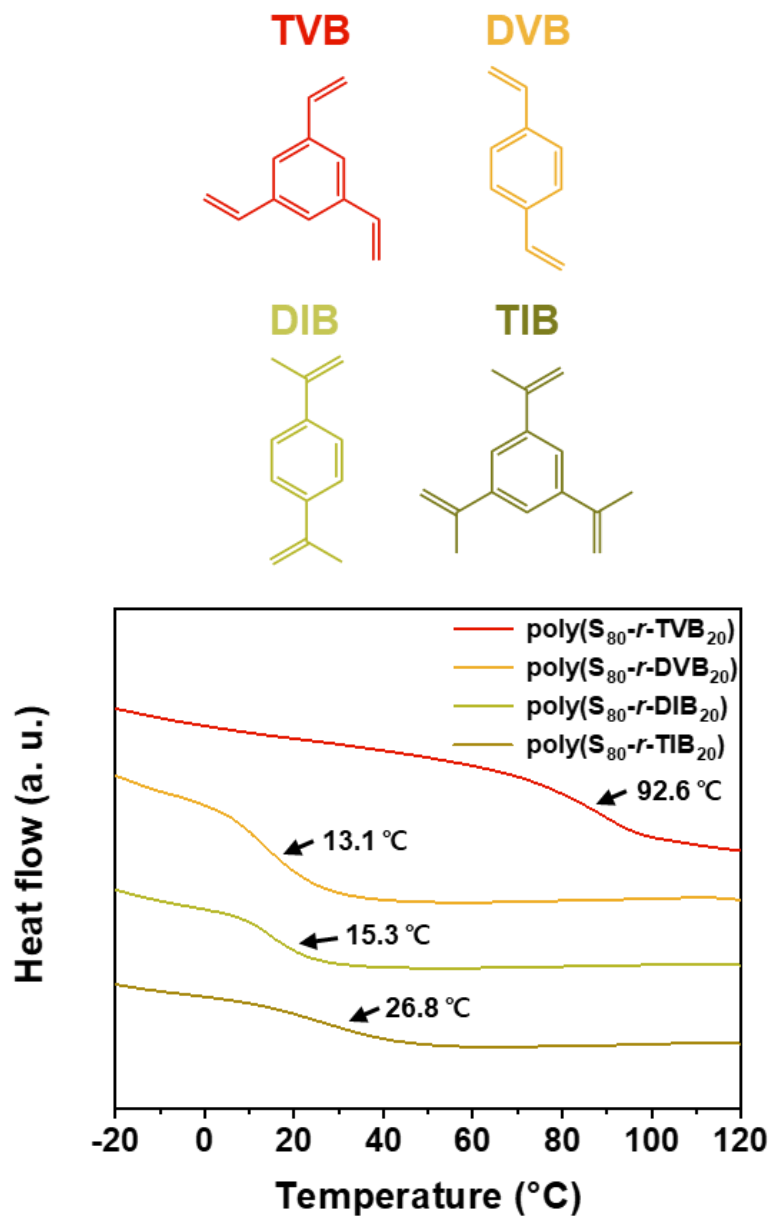
Figure 4.21. DSC curves of poly(S$_{80}$-*r*-TVB$_{20}$), poly(S$_{80}$-*r*-DVB$_{20}$), poly(S$_{80}$-*r*-DIB$_{20}$), and poly(S$_{80}$-*r*-TIB$_{20}$).
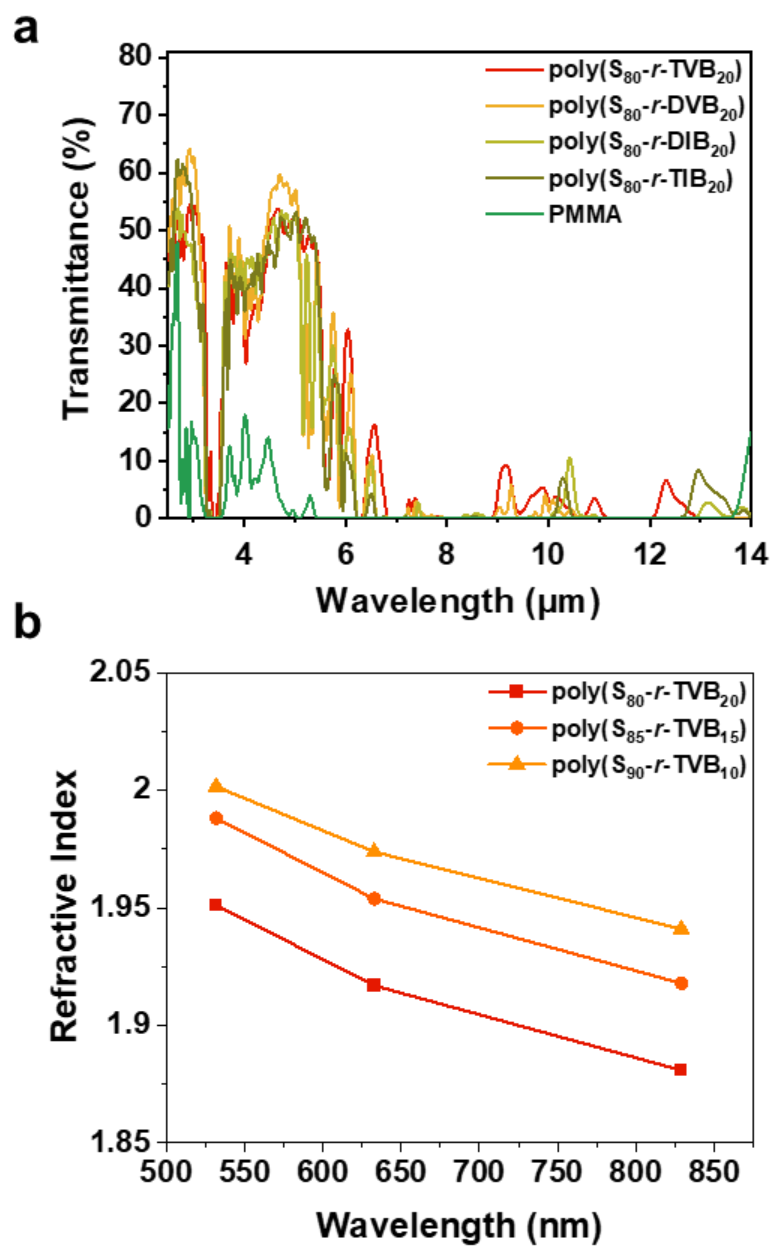
Figure 4.22. (a) IR transmission spectra for poly(S_{80}-r-TVB$_{20}$) and other sulfur-rich copolymers in the literature. (b) refractive indices of poly(S-r-TVB)s.
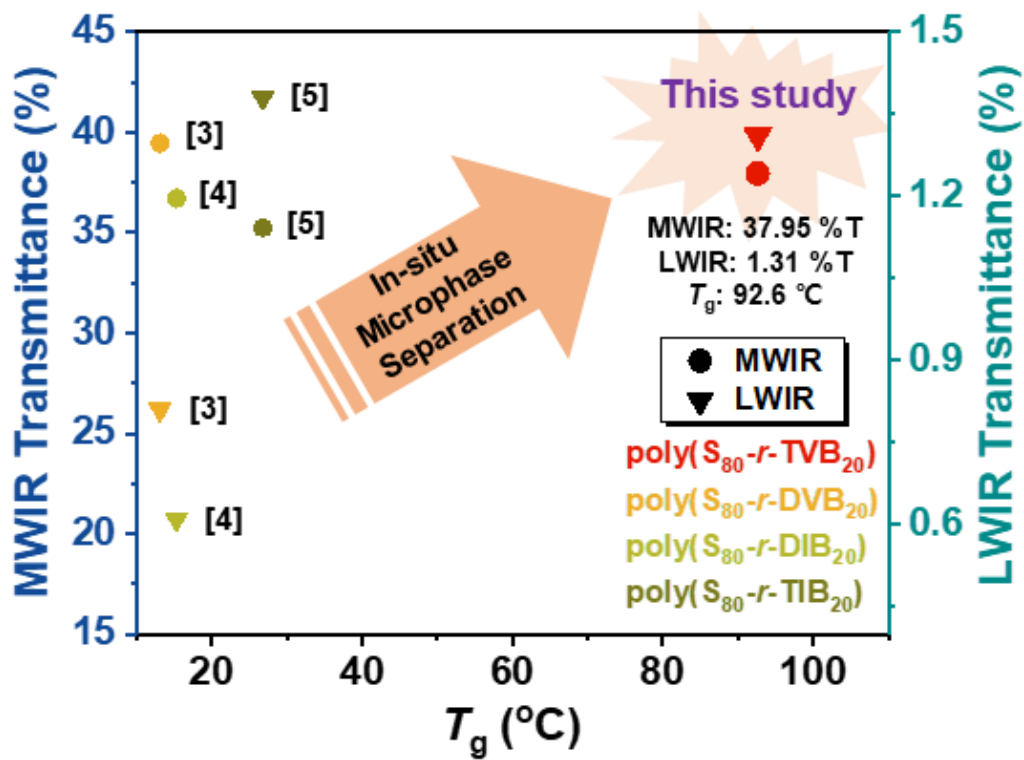
Figure 4.23. Plots of MWIR/LWIR transmittance vs. T_g for poly(S_{80}-r-TVB$_{20}$) and other sulfur-rich copolymers in the literature.
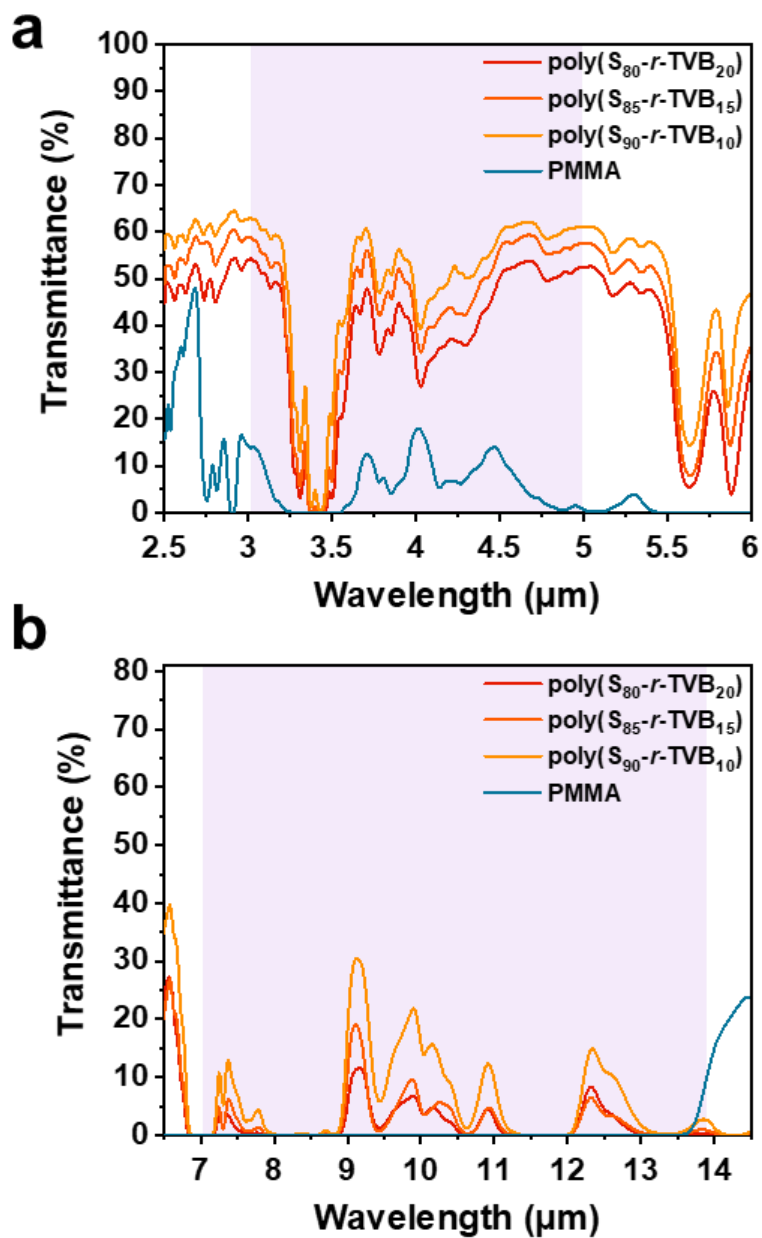
Figure 4.24. IR transmittance of PMMA and poly(S-*r*-TVB) films in the range of (a) MWIR (3–5 µm) and (b) LWIR (7–14 µm). The thickness of all films is 1.1 mm.
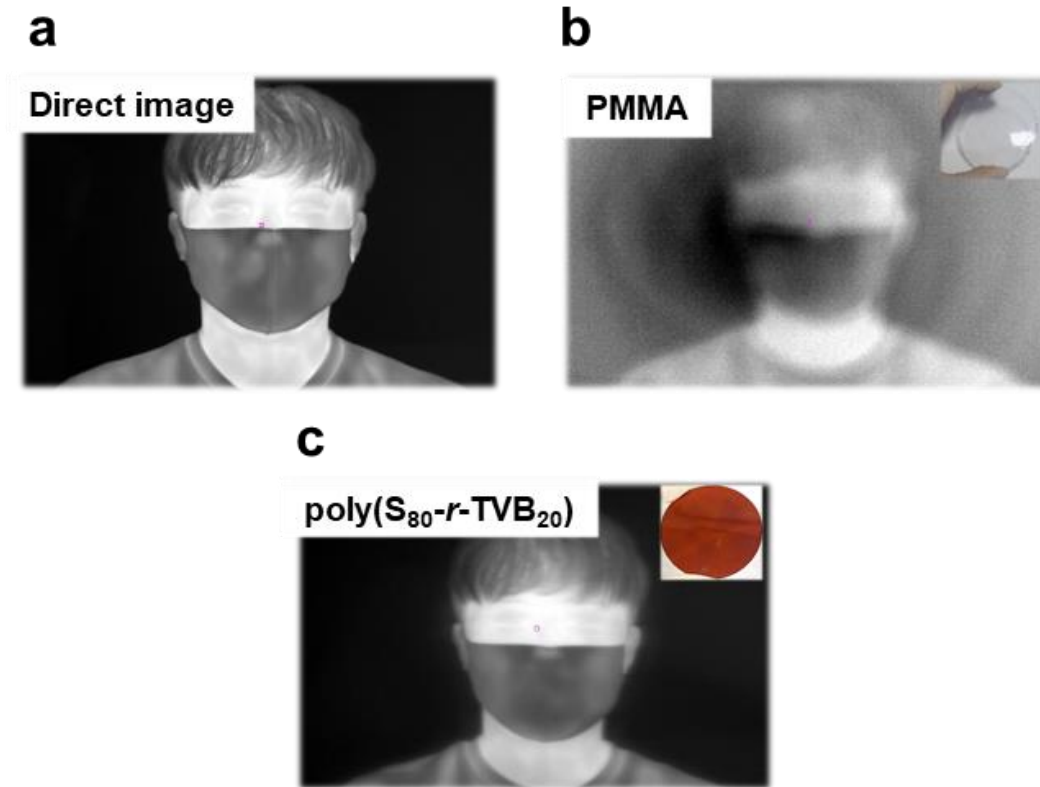
Figure 4.25. MWIR thermal images of a male subject were captured (c) without a window sample, through (d) PMMA, and (e) poly(S_{80}-*r*-TVB$_{20}$) windows. The thickness of all windows is 1.1 mm.
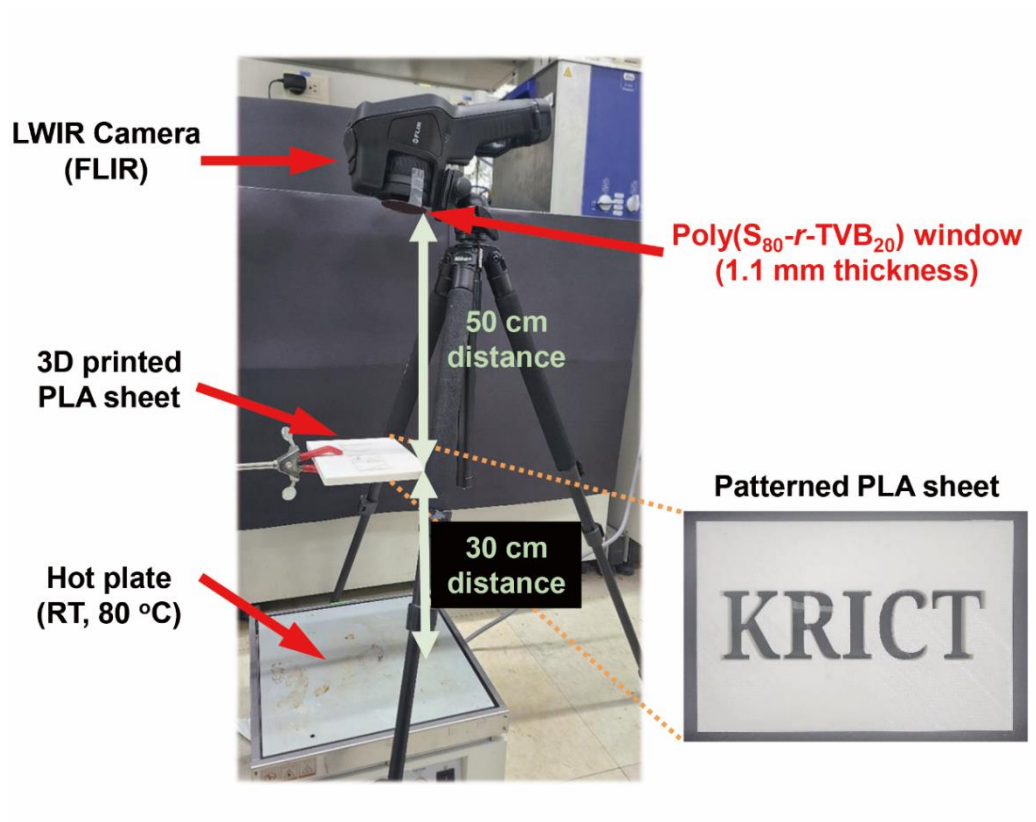
Figure 4.26. A photograph of the LWIR thermal imaging setup.
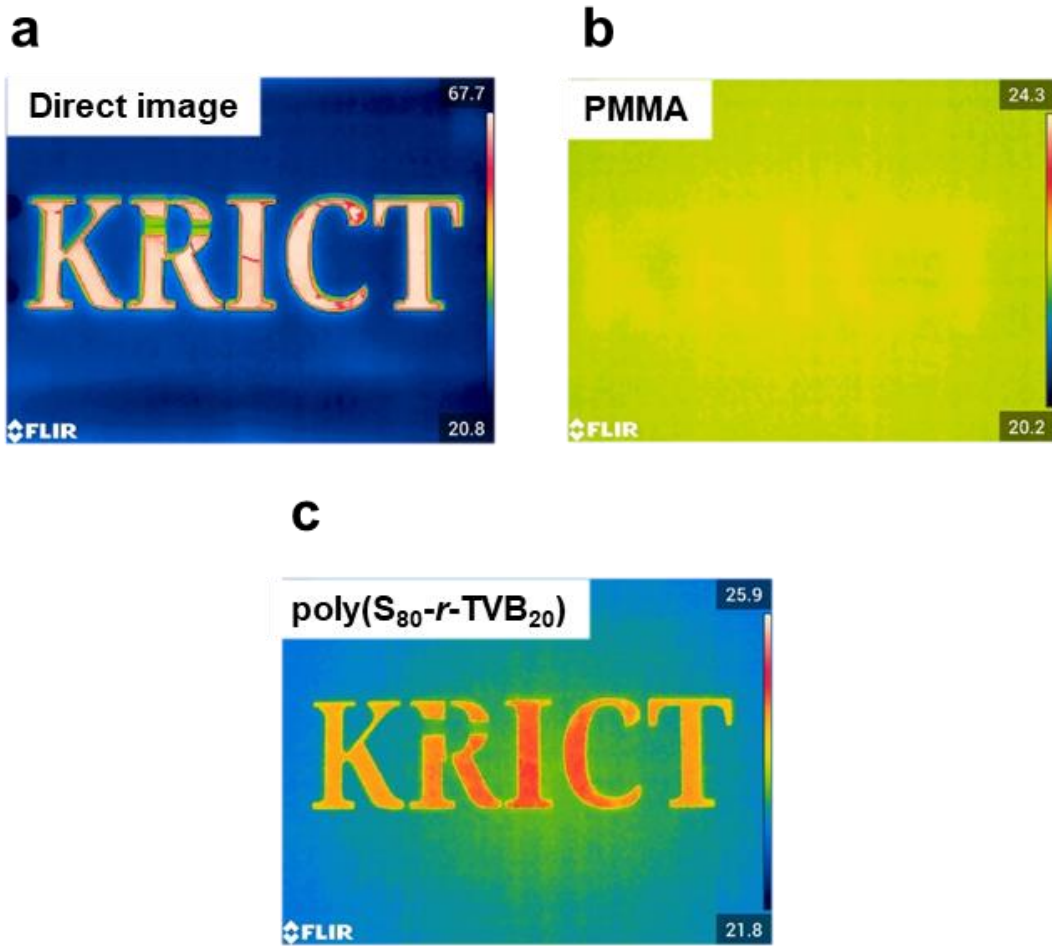
Figure 4.27. LWIR thermal images of 80 ℃ hot plate through the 'KRICT'-patterned sheet captured (f) thermal image w/o window sample, with (g) PMMA, and (h) poly(S_{80}-*r*-TVB$_{20}$) windows. The thickness of all windows is 1.1 mm.
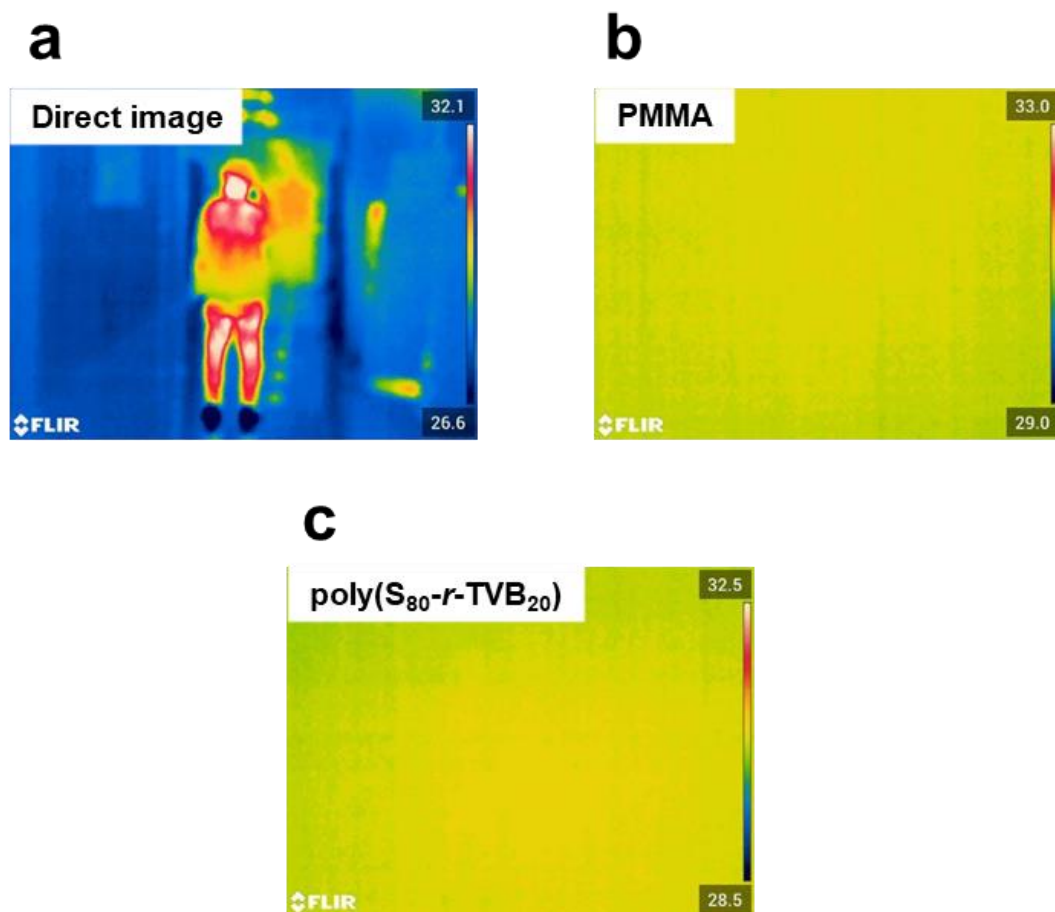
Figure 4.28. LWIR thermal images of human captured at 28 °C through (a) without window sample, (b) PMMA window, and (c) poly(S_{80}-*r*-TVB$_{20}$) window. The thickness of PMMA and poly(S_{80}-*r*-TVB$_{20}$) windows is 1.1 mm.
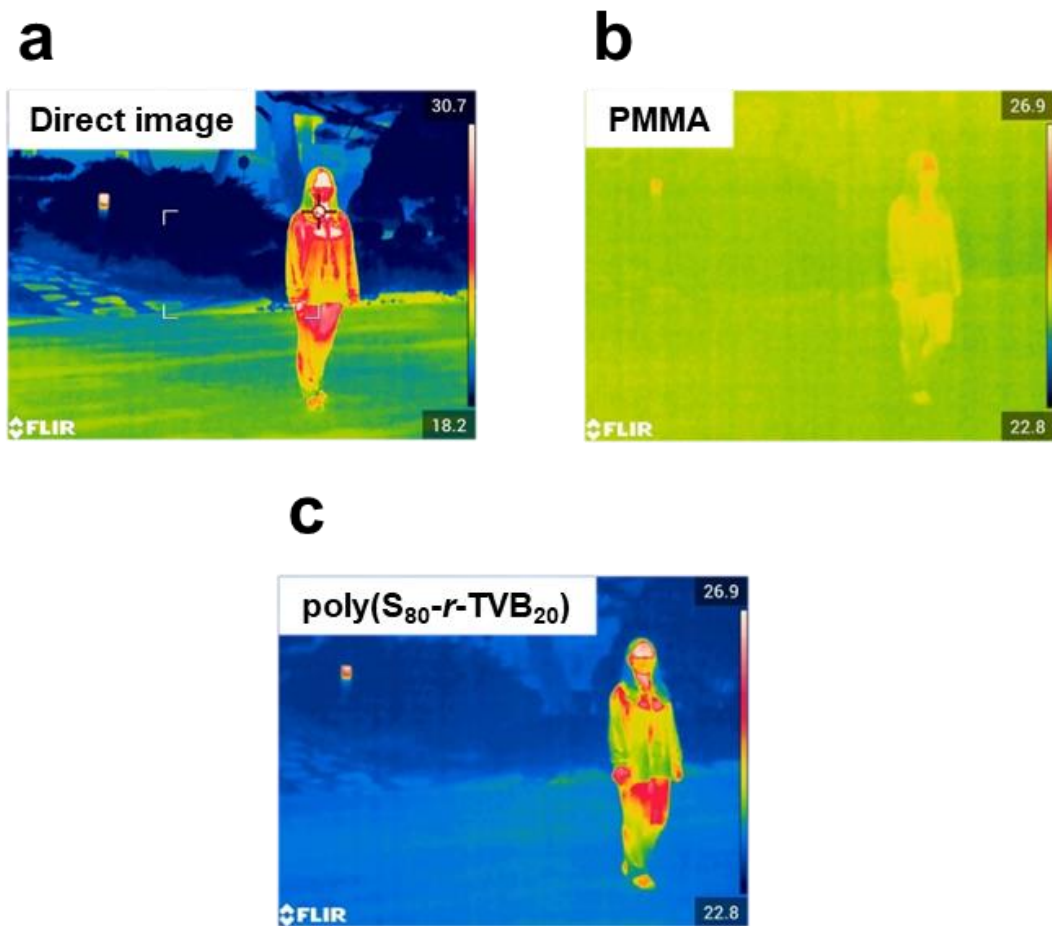
Figure 4.29. LWIR images captured (a) without a window and through (b) PMMA and (c) poly(S_{80}-r-TVB$_{20}$) windows. Each window was placed in front of the FLIR/LWIR camera. The thickness of all films is 300 µm.
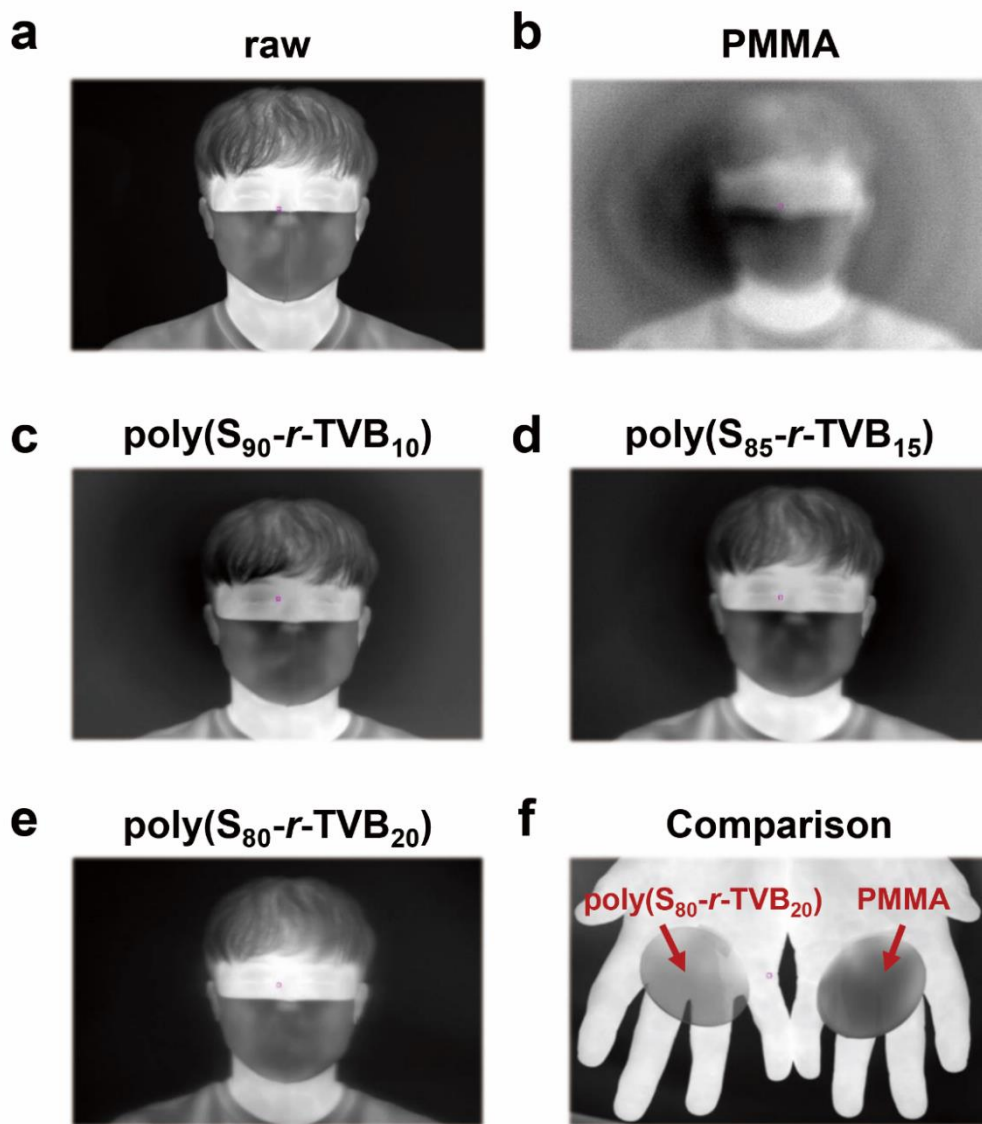
Figure 4.30. MWIR thermal images captured (a) without window and through (b) PMMA and (c-e) poly(S-*r*-TVB) windows. Each window was placed in front of the MWIR camera. (f) Comparison of the MWIR thermal images of poly(S_{80}-*r*-TVB_{20}) and PMMA windows. The thickness of all films is 1.1 mm.

초 록

본 연구에서는 소프트 로봇 및 적외선 애플리케이션을 위한 동적 공유 폴리머 네트워크의 합성 및 특성화를 제시하였다. 첫째, 동적 알릴 설파이드 교환이 가능한 MBTA 가교제와 정적 가교가 가능한 RM257 가교제를 포함하는 광제어 액정 네트워크(pc-LCN)를 합성하였다. 정적 및 동적 공유 이중 가교 pc-LCN 은 MBTA 로 인해 필름의 인터페이스 간에 레고와 같은 가역 조립을 가능하게 했으며 가교 구조는 RM257 로 인해 변경되지 않았다. 네트워크에서 정적 및 동적 공유 결합을 조정함으로써 pc-LCN 필름은 자외선 조사 하에서 복잡한 3D 구조로 쉽게 재구성되고 조립될 수 있었다. 이러한 모놀리스는 또한 구성 빌딩 블록 필름으로 분해되고 동일한 UV 자극 하에서 다른 아키텍처로 재조립될 수 있었다. 또한 선택적 가시광 반응 도펀트 염료가 pc-LCN 빌딩 블록을 작동시키기 위해 채택되었다. 가시광선 내에서 다른 파장을 흡수하는 염료를 포함하는 pc-LCN 이 선택적으로 작동되었다. 각 염료가 포함된 pc-LCN 필름 빌딩 블록은 레고와 같은 3D 소프트 변형 로봇으로 모놀리식으로 조립되었다. 여러 방향으로 구르기, 잡기, 화물 운송 등 다양한 동작 기능을 갖춘 3D 소프트 변형 로봇이 시연되었다.

둘째, 티올 비율이 10 mol % 과량으로 함유 되어있는 폴리(티오우레탄) MFTU 비트리머가 합성되었다. 과량의 티올을 함유한 MFTU 는 기존의 DBTDL 촉매와 비교하여 $Zn(DTC)_2$ 촉매 기반의 빠른 동적 티오우레탄

결합 교환을 가능하게 했다. MFTU 의 강성 변조는 네트워크 내에서 반결정 구조의 용융 전이에 의해 가능해졌다. MFTU 의 영률은 유연한 상태에 비해 강성 상태에서 70.5 배 증가했다. 또한, 수소 결합과 Zn 배위 결합의 형성은 MFTU 필름 사이의 가역 조립/분해를 실현했다. MFTU 네트워크에서는 티올 리간드 교환이 60 도 이상에서 일어나 수소결합이 분리되었다. 이때 MFTU 박막의 계면 사이에 새로운 수소결합과 Zn 배위결합이 형성되어 조립된다. 조립된 MFTU 필름에 다시 부드러운 응력으로 열처리를 가하면 티올 리간드 교환이 일어나는 동안 수소결합이 분리되어 MFTU 필름이 서로 분해된다. 이러한 다기능 특성을 통해 MFTU 빌딩 블록은 소프트 핸드 로봇으로 제작되었으며 단단한 또는 유연 상태에 따라 자기 작동을 수행했다. 소프트 핸드 로봇은 다시 소프트 리시버로 변신해 유연한 상태의 물체를 안전하게 받았다. 단단한 프로그래밍을 통해 소프트 리시버는 화물 고정 및 배송을 수행했다.

마지막으로, 현장 미세상 분리 황이 풍부한 공중합체는 TVB 를 활용한 원소 황의 역가황을 통해 합성되었다. TVB 가교제는 천정 온도가 400 °C 로 매우 높기 때문에 자가가교가 가능하기 때문에 역가황 시 자가가교된 TVB 가 풍부한 도메인이 형성된다. 원소 황이 TVB 와 반응하여 폴리설파이드가 풍부한 도메인을 형성하기 때문에, 폴리(황-랜덤-TVB) 는 미세상 분리 구조를 보였다. 80 wt %의 황 함량에서도 미세상 분리된 TVB 가 풍부한 도메인은 약 2.0 GPa 의 주목할만한 모듈러스와 92.6 °C 의

높은 유리 전이 온도로 공중합체를 자체 강화하면서 여전히 뛰어난 IR 광학 특성을 나타내었다. 적외선 이미징을 통해 폴리(황-랜덤-TVB)는 불투명한 참조 샘플에 비해 고해상도 이미지를 보여주었다. 따라서 자가가교형 TVB 가교제를 통해 황 공중합체의 적외선 투과율(황 함량)과 열적 특성 간의 트레이드오프 관계를 해소하였다.

주요어: 소프트 로봇, 액정 네트워크, 동적 공유 결합 교환, 가역 조립, 비트리머, 다양한 강성, 역가황 고분자, 미세상 분리, 열역학적 특성, 적외선 이미징

학 번 : 2017-27775